CHEMISTRY AND STRUCTURE OF COALS: EVALUATION OF ORGANIC STRUCTURE BY COMPUTER AIDED DIFFUSE REFLECTANCE INFRARED SPECTROSCOPY.{*}

E. L. Fuller, Jr., N. R. Smyrl, R. L. Howell, and C. S. Daw{**}

Plant Laboratory, Y-12 Plant, Box Y, Oak Ridge, TN 37830{***}

INTRODUCTION

Diffuse reflectance infrared Fourier transform (DRIFT) spectroscopy has become a very informative method of evaluating the chemistry and structure of coals, chars, and related materials {1,2,3}. Infrared spectroscopy has long been recognized as an informative means of studying the chemistry and physics of coals {4,5}. Recent advances in instrumentation, computer assistance, and techniques have appreciably enhanced the amount and caliber of the spectra and the scientific importance of the conclusions{6,7}. The enhanced sensitivity of these new instruments has permitted renewed interest in nondestructive spectroscopic studies by diffuse reflectance infrared spectroscopy{8,9}.

EXPERIMENTAL

The spectrometer, cell, and techniques for measuring the diffuse reflectance spectra of solid samples over a wide range of temperatures and pressures have been described previously {1,2,10,11}. A portion of this study is devoted to extending our capabilities to be able to study unperturbed solid surfaces of rather large pieces of coal and to directly monitor changes wrought in simulated chemical and physical processing. Grinding of coals is known to alter the chemical and physical structure of coals and although DRIFT studies require much less stringent treatment{9} there is most assuredly some modification due to the energy dissipation accompanying percussive grinding{12}. The coal sample for this study was a "run of the mine" aliquot taken from the -3/+4 mesh seive fraction, sealed in a glass bottle and stored for approximately two months, free from thermal effects (drying) and extensive oxidation (weathering) which are known to markedly alter the morpholgy and chemistry of both the organic and the inorganic (mineral) constituents in coals{13}. This sample was provided by the Tennessee Valley Authority from the Paradise (Kentucky) Mine and is generally ranked as High Volatile C-Bituminous as representative of the feed stock for the fluidized bed combustion facility.

RESULTS AND DISSCUSION

Typically the cleaved surfaces (parallel to the bedding plane) vary in appearance due to the heterogeneous distribution of the macerals in the structure. The variation in reflection of visible light allowed us to focus on glossy or dull areas of the surface of the piece of coal and to note the variation in DRIFT response over distances greater than our beam size (ca. 2mm with our 6X condensing optics). Figure 1 shows the variation in DRIFT signal. Spectrum A was taken with the incident beam flooding a visibly homogenous region of high reflectivity and we note that there is appreciable specular reflection in the infrared with little or no spectral features indicative of diffuse reflection. The negative features (500 and 1100 cm-1) are undoubtedly

due to anomolous despersion or reststrahlen effects{14,15} which are regarded as detrimental to DRIFT analyses and allow us to deduce some information concerning the physical state (consolidation) of the coal structure in this region. In marked contrast we note appreciable difference when sampling and dull area of the same piece of coal. The DRIFT spectrum, spectrum B, is still of very poor quality due to the consolidated nature of the substrate. Very good DRIFT spectra can be obtained after gentle abrasion of the surface with fine grit "Emory Paper" and removal of the dislodged material as shown in Spectrum C of Figure 1. This mild abrasion forms a surface which is rough enough to reflect and absorb electromagnetic radiation much as a fine powder. This spectral response is virtually identical to that of powders of similar rank, given that the quantitative nature varies due to chemistry and structure of individual aliquots. These spectra in turn correlate quite well with their counterparts obtained in the transmission mode after encapsulsation in KBr or some other support medium.

Figure 2 serves to show that one can use the DRIFT technique to monitor chemical and physical changes of a given sample of coal very well. Spectrum D shows the DRIFT response of the same area of the same sample in vacuum at 400 C after exposure to oxygen gas at 400 C long enough to attain the steady state conditions deduced by sensing no further change in spectral features (intensities, band shapes and intensties) with time. Visual observation allows one to semiquantitatively deduce some of the relevant steps associated with oxidation. Within the depth of DRIFT response the aromatic (e) and aliphatic (f,g,h) hydrogen content is essentially depleted and there is a marked increase in carbonyl content ranging from aldehydes/ketones (k) to the more oxygen rich acid anhydrides (i,j). These oxygen insertion precursors to gaseous carbon dioxide give rise to spectral intensities which actually exceed that of the omnipresent polynuclear aromatic (l) and methylene/ether (m,n,o) crosslinks. All of this is noted to have little effect on the oxy-hydrogen phenolic, alcoholic and acid entities that are present in various states of hydrogen bonding and gives rise to the broad absorption feature (3600 to 2000 cm-1). A very rich and enticing potpourri of potentially valuable information to say the least.
One can note the limited penetration involved in DRIFT studies and also note that the oxygen attack involves a layer of material near the surface. Reabrasion of the same area of the same sample gives rise to DRIFT spectrum E of Figure 2 where we note the reversion to the spectral state so classically characteristic of the original coal. The hydrocarbon bands (e,f,g,h) are again prominent and the carbonyl bands (i,j,k) are greatly diminished indicating that there probably existed a gradient of oxygen density which "tailed" beyond the approximately 50 micrometers removed in the second abrasion. All of the spectral features of E are somewhat enhanced with respect to C due to an increase in DRIFT efficiency brought about by a more enhanced roughness and/or a modified refractive index due to loss of infrared inactive graphitic carbon during the combustion phase of this study. Future studies with thinner sectioning will allow us to obtain further details from a detailed and quantititive analysis of the chemical and stuctural profile of the steady state oxygen insertion/diffusion process.

To this end we have instigated a program to quantitatively analyze our DRIFT spectra. The problem is complex since virtually every band overlaps one or more adjacent bands. There is currently a strong international move to quantitatively analyze infrared spectra in general {16.17,18,19} and coal spectra in particular{6,7} using sophisticated and readily available computers{20}. Figure 3 is our analysis of the data of DRIFT spectrum E, using the second derivative to rather accurately assess the frequencies of the individual contributing absorption bands in terms of the resultant inflection points in the summation composite. The results compare favorably with those of Painter et. al.{7}. There has been a renewed interest in "resolution enhancement" of spectra by deconvolution{21} techniques now that fast Fourier transforms are available and the required algorithms have been developed. Griffiths et.al.{9} have been able to accurately position coal structure bands with Fourier self deconvolution of their spectra. Our results are give in Figure 4 for the hydrocarbon region of DRIFT spectrum E shown with the Fourier self-deconvolution. Comparison of Figures 3 and 4 merely point out the close relationship between deconvolution and derivatization in terms of the multiplicative operation that corresponds to each in the time domain{22,23}. Both operations are mathematically classed as filter functions (albeit negative or "unsmoothing" filters in this instance){24}. The prime utility of both techniques is to accurately measure characteristic band frequencies without the human error associated with locating inflection points and "shoulders" reliably and reproducibly. That goal is achieved admirably in both cases. It is now such a simple task that we can turn it over to the simple "mind" of the computer where the maxima in both curves are evaluated without human intervention or bias. Table 1 tabulates the band position for our analyses compared to the results of others{25,26}. These carbon-hydrogen stretching frequencies are ideally suited to test our program since they are relatively immune to substituent and environmental effects{25}.

Quantitative analyses requires accurate evaluation of the intensity (height), integrated area and/or band width of the bands associated with the vibration of each entity. This can be done most reliably by iterative minimum least squares{16,17} or some related technique in which the summation of the composite peaks most closely matches the experimental spectrum. The band positions from the second derivative and/or Fourier self-deconvolution are used as first approximations and intensities are estimated ratiometrically (utilizing the area conservation inherent in deconvolution). Initial band widths are taken to be the optimum value (average) used in the Fourier self-deconvolution. Generally the iterations converge in 6 to 10 steps without divergence, which can occur if initial estimates are grossly disparate from the optimum value. Our results are given in Figure 5 where we note that the deviation (upper line) is at or near the signal/noise ratio of the experimental spectrum. When this case prevails (standard deviation approximately equals the signal/noise ratio) for the converged interations there is no justification of further deconvolution and/or incorporation of additional bands in the envelope. Conversely, more stringent deconvolution is not warranted if the standard deviation is not appreciably diminished toward the signal/noise ratio. These

techniques are readily implemented with the aid of today's computers and we must be cautious that we do not abuse them by taking them beyond their limits.

The broad band due to the oxygen-hydrogen stretching vibrations is seen to be composed of 5 bands whose intensities and widths are given in Figure 6. The positions and widths of these bands closely match those of Solomon et. al.{6}. Our spectrum is taken in vacuum (.00002 torr) and is a true vacuum spectrum as compared to the purge state that is approached when alkali halide pellets are allowed to equilibrate. It is readily noted that the five frequencies are associated with successively stronger hydrogen bonding {27,28,29}. The relative strengths are due to higher degrees of coordination between that of a linear bond to that of the 5 fold interaction of cubic close packing of the acceptor ligands oriented somewhat symmetrically around the donor hydrogen of the covalent phenol, alcohol, or acidic entities. Intermediate states correspond to lesser interactions with hydrogen. Each band corresponds to increased O-H length, decreased O-H...O separation, increased bandwidth, and enhanced extinction coefficient in accordance with known behavior of similar hydrogen bonding{27-29}. The importance in a good understanding of these hydrogen bonds is essential to understanding the structure and chemistry and structure of coals and related materials. More detail will be given in the oral presentation.

The utility of this computer aided analysis is quite evident when applied to the lower frequency range (Figure 8) where classical methods based on visual observation and operator judgement are far from quantitative. For example, the carbonyl bands at 1843, 1760 and 1720 cm-1 are readily resolved even in the presence of the very large aromatic peak at 1608 cm-1{9}. More details will be given in the oral presentation to note the quantitative aspects of analyzing successive spectra to elucidate the mechanism of oxidation of coals and chars.

CONCLUSIONS

Modern spectrometers with computer aided data aquisition and processing are very well suited to obtain diffuse reflectance infrared spectra of coals with a minimum time and effort for sample preparation. The spectra are of high caliber and are very comparable to the best transmission spectra. Quantitative data is obtained for the region penetrated by the incident beam. Depth profiling is possible utilizing this surface sensitivity of the DRIFT technique. Lateral scanning is also possible to allow one to evaluate the heterogeneity and specie distribution in the plane of the surface. The utility of DRIFT techniques, so well recognized for powdered coals, can be used on consolidated coals and thus measure and map chemistry and structure of of the original coalified matrix. These studies are easily effected under controlled environments to maintain coal bed conditions (high relative humidity), generate inert atmospheres (nitrogen or argon gas), induce and montior reactions (hydration/dehydration, oxidation, hydrogenation, carbonation ,etc.), or virtually any combination over a wide range of temperatures (77 K to 800 K) and pressures (.00002 torr to 2000 torr) with our present cell. All of the studies are easily made free of matrix and supports normally used for IR studies of

solids. The high quality of the spectra are well suited to quantitative analyses using modern computer aided deconvolution and related composite band evaluation techniques. We now can start to evaluate the complex chemistry and structure of coals and related materials and to follow the fate of each and every specie as we obtain spectra under realistic conditions of coalification and subsequent combustion or processing for fuels and feedstocks.

REFERENCES

1. N. R. Smyrl and E. L. Fuller, Jr., "Chemistry and Structure of Coals: Diffuse Reflectance Infrared Transform (DRIFT) Spectroscopy of Air Oxidation." in "Coal and Coal Products: Analytical Characterization Techniques" edited by E. L. Fuller, Jr., American Chemical Society, 1982.
2. E. L. Fuller, Jr., N. R. Smyrl, R. W. Smithwick, and C. S. Daw, "Chemistry and Structure of Coals: Air Oxidation Related to Fluidized Bed Combustion", Preprints, Div. Fuel Chem. A.C.S., 28, 44(1983).
3. M. P. Fuller and P. R. Griffiths, Anal. Chem. 50,1906 (1978).
4. D. W. van Krevelen, "Coal", Elsevier Publ., 1961.
5. Robert S. McDonald "Review: Infrared Spectrometry", Anal. Chem. 54, 1250, (1982).
6. P. R. Solomon, D. G. Hamblen and R. M. Carangelo, "Applications of Fourier Transform Spectroscopy Infrared Spectroscopy in Fuel Science", in "Coal and Coal Products: Analytical Characterization Techniques", edited by E. L. Fuller, Jr., American Chemical Society, 1982.
7. Paul C. Painter, Randy M. Snyder, Michael Starsinic, Michael Coleman, Deborah W. Kuehn, and Alan Davis, "Fourier Transform Infrared Spectroscopy: Application to the Quantitative Determination of Functional Groups in Coal", ibid., 1982.
8. Peter R. Griffiths and Michael P. Fuller, "Mid-infrared Spectrometry of Powdered Samples" in "Advances in Infrared and Raman Spectroscopy" Vol. 9, p. 63, edited by R. J. H. Clark and R. E. Hester, Heyden and Sons, 1982.
9. Peter R. Griffiths, Shih-Hsien Wang, Issam M. Hamadeh, Paul W. Yang and David E. Henry, "Direct Investigation of Reacting Coals by Diffuse Reflectance Infrared Spectroscopy", Preprints, Division of Fuel Chemistry, A.C.S. 28, 27 (1983).
10. N. R. Smyrl, E. L. Fuller, Jr., and G. L. Powell, Applied Spectroscopy 37, 38 (1983).
11. E. L. Fuller, Jr., N. R. Smyrl, J. B. Condon and M. Eager, J. Nuclear Materials, IN PRESS(1983).
12. E. L. Fuller, Jr., J. Colloid and Interface Science 75, 577 (1980)
13. E. L. Fuller, Jr., J. Colloid and Interface Science 89, 309 (1982)
14. W. W. Wendtlandt and H. G. Hecht, "Reflectance Spectroscopy", Interscience Publ., 1966
15. F. A. Jenkens and H. E. White, "Fundamentals of Optics", McGraw-Hill, 1957.
16. R. D. B. Fraser and E. Suzuki, Anal. Chem.,38,1770 (1966)
17. R. D. B. Fraser and E. Suzuki, Anal. Chem.,39,37 (1969)
18. R. N. Jones and K. Shimokoshi, Applied Spectroscopy, 37, 59 (1983)
19. P. H. Von Cittert, Z. Phys., 69, 298 (1931).
20. R. Peter Young, "Computer Systems", in "Infrared and Raman Spectroscopy" edited by E. G. Brame, Jr., and J. G. Grasselli, Marcel Dekker, 1977.

21. W. E. Blass and G. W. Halsey, "Deconvolution of Absorption Spectra", Academic Press, 1981.
22. J. K. Kaupinen, D. J. Moffat, H. H. Mantsch and D. G. Cameron, Anal. Chem. 53, 1454 (1981)
23. R. E. Ziemer and W. H. Tranter, "Principles of Communications", Houghton Mifflin, 1976.
24. J. K. Kaupinen, D. J. Moffat, D/ G/ Cameron and H. H. Mantsch, Applied Optics 20, 1866 (1981).
25. Norman B. Colthup, Lawrence H. Daly, and Stephen E. Wiberley, "Introduction to Infrared and Raman Spectroscopy", Academic Press,1964
26. Herman A. Szymanski, "IR: Theory and Practice of Infrared Spectroscopy", Plenum Press, 1964.
27. George C. McClellen and A. McClellan, "The Hydrogen Bond", W. H. Freeman, 1960.
28. Serge N. Vinogradov and Robert H. Linnell, "Hydrogen Bonding", Vand Nostrand Reinhold, 1971.
29. Walter C. Hamilton and James A. Ibers, "Hydrogen Bonding in Solids", W. A. Benjamin, 1968.

{*} This study was funded by the Tennessee Valley Authority through The Engineering Technology Division of The Oak Ridge National Laboratory.
{**} C. S. Daw is a member of The Engineering Technology Division, Oak Ridge National Laboratory, Oak Ridge, TN 37830
{***} Operated for The United States Department of Energy by Union Carbide Nuclear Division under U. S. Government Contract Number W-7405-eng-36.

TABLE 1. VIBRATIONAL FREQUENCIES EVALUATED FOR KENTUCKY #9(58) COAL
(freqencies tabulated as wavenumbers, cm-1)

This work	Ref. 7	Ref 25	Assignment
3051	-----	3050+/-50	Ar-H
3017	-----	3025+/-25	R2C=CHR & RCH=CHR
2958	2956	2962+/-10	RCH3
2925	2923	2925+/- 5	ArCH3 & R2CH2
2894	2891	2900+/- ?	R3CH
2870	2864	2872+/-10	RCH3 & ArCH3
2854	2849	2855+/-10	R2CH2
2752	-----	2732+/-12	RCHO

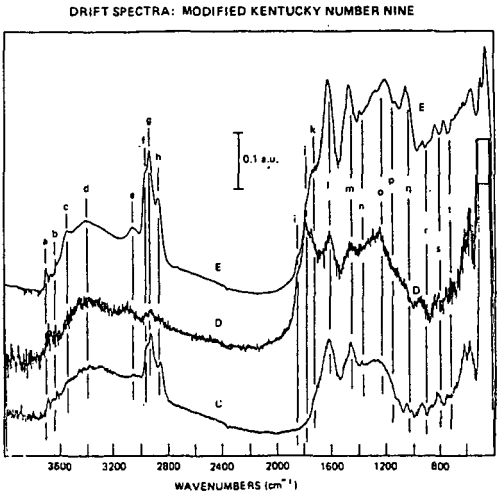

Figure 2. Effects of Chemical and Physical Treatment of Kentucky #9

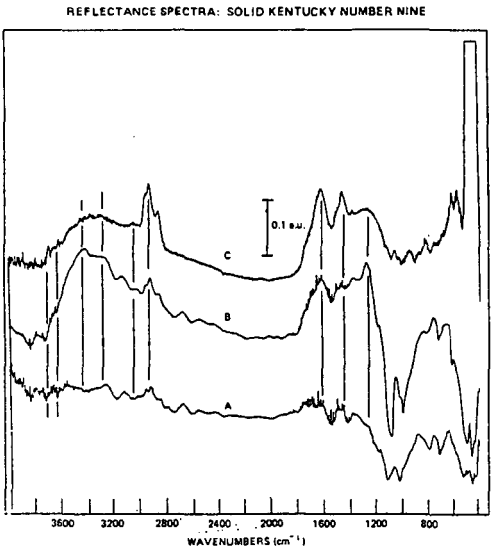

Figure 1. DRIFT Spectral Variation for Kentucky #9

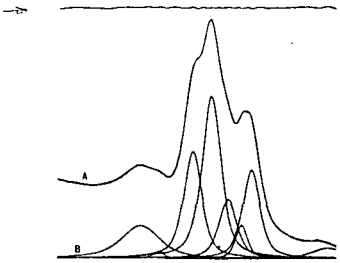

Figure 5. Least Squares Composite Sum for Hydrocarbon (K958)

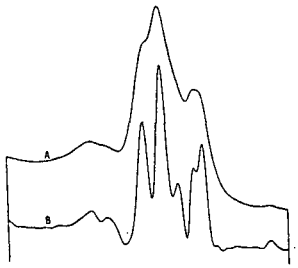

Figure 4. Fourier Self-deconvolution of Hydrocarbon Spectrum (K958)

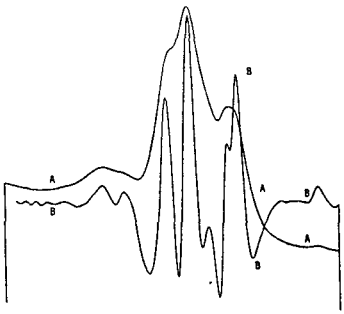

Figure 3. Second Derivative Analysis of Hydrocarbon Spectra (K958)

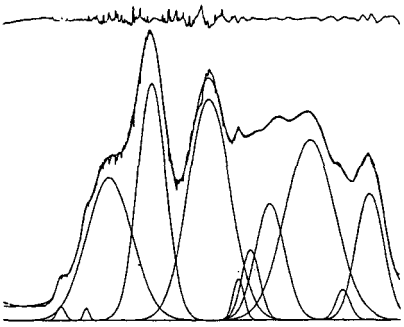

Figure 8. Least Squares Composite Sum for Low Frequency Bands (K958)

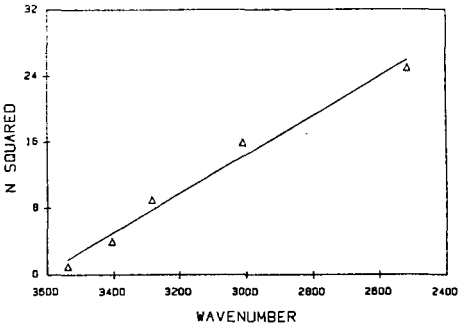

Figure 7. Hydrogen Bonded Hydroxyl Sequence Variation (K958)

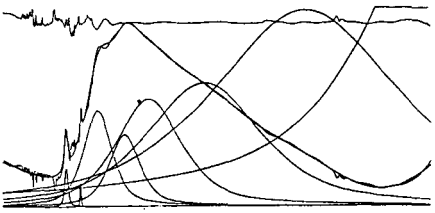

Figure 6. Least Squares Composite Sum for Hydroxyl Bands (K958)

RELATION BETWEEN HYDROCARBON STRUCTURE AND FRAGMENTS PRODUCED IN PYROLYSIS

Peter R. Solomon, Kevin R. Squire and Robert M. Carangelo

Advanced Fuel Research, Inc., 87 Church Street, East Hartford, CT 06108

Analysis of the heavy molecules which form tar in hydrocarbon pyrolysis can provide clues to the mechanisms of their release and to the structure of the parent molecule. This paper considers the relationship between the original hydrocarbon structure and the product tar. Pyrolysis experiments have been performed in a heated grid apparatus on several coals and lignins and on a polymer specifically synthesized to model features of natural hydrocarbons. Tars were collected and analyzed by Fourier Transfrom Infrared (FT-IR) Spectroscopy. The functional group composition of tars for a bituminous coal, a lignin and a polymer are all remarkably similar to the functional group composition of the parent material. It is believed that for these samples, the tar consists of minimally disturbed fragments of the original organic matrix. Molecular weights of tars were determined by Field Ionization Mass Spectrometry (FIMS) for tars collected from the heated grid apparatus and for samples pyrolyzed directly in the FIMS apparatus. The mass spectra all exhibit features reflecting structural aspects of the parent molecule and for the softening bituminous coals, the lignin and the polymer, the upper limit of molecular weight appears limited by vaporization. The process appears to be controlled by the combined effects of pyrolysis and vaporization, where bond breaking is required to produce fragments which are small enough to volatilize. The fragments are, therefore, similar in composition to the parent solid but lower in molecular weight.

A computer model for the coupled pyrolysis and vaporization of macromolecules has been used to interpret the results. The theory combines random cleavage of weak bonds in the polymer (to produce "metaplast") with transport of depolymerization fragments by vaporization and diffusion. The theory predicts product yields and molecular weight distributions in agreement with the observed results. An attempt has also been made to fit the regular structure in the FIMS spectra with an assumed distribution of likely homologous series. Although the assignments are highly speculative, it is possible to obtain a reasonable facimile of the FIMS spectra with chemically reasonable choices.

EXPERIMENTAL

The pyrolysis experiments were performed in an apparatus which employs an electrically heated grid within an infrared cell to provide on-line, in-situ analysis of evolved products by Fourier Transform Infrared (FT-IR) Spectrometry. In the flash pyrolysis experiments, the cell was closed and the grid was heated to a final temperature at between 600 and 2000°C/sec. Char yield was obtained gravimetrically from the residue in the grid. Tar samples were obtained from the cold glass wall of the cell or from in-line filters and yields were obtained gravimetrically. Details of the experiment have been described previously (1,2).

The field ionization mass spectrometry (FIMS) experiments were performed at SRI International. The FIMS technique ionizes molecules with minimal fragmentation and so gives a direct molecular weight distribution (3).

The preparation of the polymer, poly(1,4-dimethylenenaphthalene), napthalene rings linked by ethylene bridges, is described elsewhere (4).

RESULTS

In relating pyrolysis products to the parent hydrocarbon, one of the most striking observations is the similarity often seen for the functional group composition of the two materials. Figure 1 shows FT-IR spectra for the tars, parent hydrocarbons and their differences for the model polymer, a lignin, a lignite, and a bituminous coal. Except for the lignite, the pairs of spectra are quite similar.

An important difference in the bituminous coal spectrum is a higher methyl group concentration in the tar which appears to result from rupture of C(aliphatic)-C(aliphatic) bonds followed by radical stabilization. Similarly the loss of C(aliphatic)-O bonds in lignin tar is probably due to rupture of ether bonds and evolution of water.

Molecuar weight distributions for the heavy products obtained for these 4 samples plus two additional coals are presented in Figs. 2 and 3. All samples except for the lignin (which was pyrolyzed in the heated grid apparatus) were directly pyrolyzed in the FIMS apparatus. These samples were heated at approximately 2-3°C/min to temperatures up to 460°C. The molecular weight distribution is for the sum of products obtained during pyrolysis. The darker spectra in Figs. 2b and 3 are the odd numbered masses for molecules which include nitrogens or C^{13}. The simplest spectrum is that of the polymer. It consists of oligomers from monomers to heptamers. All the oligomers are released over a narrow temperature range between 400° and 425°C. This contrasts with the results obtained when the polymer tar is used as the sample in the FIMS. In this case, the sample distills with monomers and dimers coming off below 150°C, trimers and tetramers below 275°C and pentamers and hexamers near 400°C (4). This contrast suggests that the distribution of oligomers in Fig. 2a does not result from evaporation alone, but must be controlled by pyrolysis. The next simplest spectrum is that for lignin which appears to result from monomers, dimers and trimers. The large contribution of dimers in this spectrum is thought to be due to dilignols linked by thermally stable bonds.

The mass spectra of the coal pyrolysis products (Fig. 3) are the most difficult to interpret. The spectra consist of regularly spaced clusters of peaks on top of a smooth background. The height and width of the background increases with rank. Extensive studies of coal pyrolysis products have been performed by Meuzelaar and co-workers (5-7). Their results are obtained for electron impact ionization which produces fragmentation, while the FIMS spectra presented here have negligible fragmentation. Meuzelaar's results can, however, be used to guide our assignment of many of the FIMS peaks. For example, the following homologous series have been identified in Py-MS spectra: m/z- 110, 124, 138 (dihydroxy-benzenes); m/z-94, 108, 122, 136, 150 (phenols); m/z-142, 156, 170, 184 (napthalenes); and m/z-92, 106, 120 (benzenes).

A number of observations can be made about the spectra: 1) The peaks are organized into peak clusters which have a long range periodicity of 12 1/2 mass units. For subbituminous and higher rank coals, the peaks clusters appear to be arranged in groups of 4 with the peak clusters at 160, 210, 260, 310, etc. being larger than the previous peak cluster. The interpretation is that each set of 4 peaks is a similar series differing by an additional fused aromatic ring. After the addition of a new ring, the next peak cluster is larger by 14, representing the addition of saturated carbons, but the spacing is gradually reduced as the number of extra carbons grow, reaching 12 1/2 mass units per cluster with the addition of the next ring. The change in spacing is thought to result from increasing unsaturations as the side chains grow and form rings. 2) There are relatively low intensities at mass numbers for unsubstituted aromatics such as napthalene and anthracene; methyl or hydroxyl substituted aromatics have higher values but bi-substituted compounds appear to achieve a maximum. The interpretation is that fragments require the breaking of at least one and, more likely, two bonds, and therfore, are left with one or more substitutions. 3) There are a number of homologous series which are separated by saturated carbons. The relationship of these peaks can be seen by plotting their intensity as a function of the time (or temperature) at which they were evolved. Fig. 4 shows a series of peaks for a Pittsburgh Seam bituminous coal at 108, 122, and 136 compared to a series at 110, 124 and 138. The latter series evolves at a shorter time (lower temperature) than the former. The interpretation is that the 110 series is dihydroxy-benzene, while the former is a methyl hydroxy-benzene. The latter will likely require the breaking of C(aliphatic)-C(aliphatic) bonds which requires more energy and have higher temperatures than the breaking of C(aliphatic) bonds. 4) The relationship between the compound class and the temperature of evolution is further examined in Fig. 4b

which presents the time-dependent intensities of 5 masses associated with one cluster for a lignite. As can be seen, the temperature of evolution goes down with increasing molecular weight. The lignite peaks are more widely separated than for the bituminous coal. As can be seen, the highest molecular weight corresponds to oxygen substituted species, while the lowest corresponds to methyl. This reduction in pyrolysis temperature of oxygenated species is consistent with the rank dependence in pyrolysis products discussed in (8) presented at this symposium. The highest and broadest profile corresponds to a molecular weight having the widest variety of contributing compounds.

DISCUSSION OF TAR FORMATION IN COAL AND OTHER HYDROCARBONS

The mechanisms of tar evolution have been considered by a number of investigations (9-16). It is generally agreed that the process includes the following steps: 1) Formation of tar molecules, 2) transport and evaporation, and 3) possible repolymerization to form coke or char. The questions are: what is the source for tar, how are tar molecules formed, what are the transport bottlenecks and what is the relationship between the formation, transport and repolymerization of tar molecules? The following conclusions were reached in a recent review (17).

1. For bituminous coals, lignins, and some polymers, tar molecules appear to be minimally disturbed fragments of the coal's organic structure. The evidence for this is the striking similarity between the tar and parent material which has been observed in elemental composition, IR spectra (see Fig. 1) and NMR spectra.

2. The production of tar molecules involves bond breaking. The possibility that tar molecules exist in the parent material and are released through evaporation without any bond breaking can be ruled out on the basis of two observations. The first is that extractable molecules generally have a higher average molecular weight than tar molecules (18-20). The second observation is that the evaporation of previously formed tar has a much different temperature dependence than evolution of tar from coal, as discussed above.

3. The variation of yield and molecular weight distribution of tar with pressure suggest that the transport is controlled by gas phase diffusion. An example of the influence of pressure on the molecular weight distribution is illustrated in Fig. 5 which presents FIMS data for a Pittsburgh Seam coal tar produced at 4 atm., and a polymer tar produced at 5 atm. The reduction of the average molecular weight with increasing pressure is striking (see Figs. 2a and 7c). Unger and Suuberg have presented similar data (11-13) and have argued (14) that for softening coals this effect and the variation of yield with pressure can be explained by assuming that the limitation is the diffusion away from the liquid surface during the evaporation process. High pressures hinder the evolution of heavier molecules leading to cracking or repolymerization.

Considering the available evidence, tar formation in softening hydrocarbons may be viewed as a combined depolymerization and evaporation process in which the pyrolytic depolymerization continually reduces the weight of the molecular fragments through bond breaking and free radical stabilization until the fragments are small enough to be evaporated.

For non-softening coals, vaporization at the ambient pressure of the experiment does not appear to be the transport bottleneck. In Figs. 2 and 3, the very low molecular weight of the tars from non-softening lignite and subbituminous coal compared to that from the softening polymer, lignin and bituminous coal, suggests that some other mechanism for limiting the evolution of high molecular weight components must exist, possibly activated diffusion in the solid as suggested by Gavalas et al (15).

MODELING

A theory for the combined effects of bond breaking and vaporization has been developed. The theory combines random cleavage of weak bonds (similar to the concept used by Gavalas et al (15)) with transport of depolymerization fragments by vaporization and diffusion (like Unger and Suuberg (14)) to predict product yield

and composition. The assumptions in this theory include: (1) the bonds between the monomer units in the polymer molecules are the only weak bonds and are equally likely to be cleaved; and (2) repolymerization to form a different chemical structure is not included.

For any oligomer (i) with molecular weight M_i the theory computes the rate of loss due to bond breaking to form smaller oligomers, the rate of increase due to formation of new oligomers from the breaking of higher molecular weight oligomers and the rate of loss due to evaporization. The process continues as long as hydrogen is available to stabilize the free radicals. Integrating the rate equations over time yields the amount and molecular weight distribution of the vaporized products which constitutes the tar. The computations for the polymer (which has only one monomer) are the numbers in parenthesis on Figs. 2 and 5. The predictions compare favorably with the second set of numbers which are the observed integrated intensities. The theory applied to lignin assuming 7 monomers was described in a recent publication (21). The theory gives reasonable results.

Coal is more difficult to model because of the variety of monomer types and bond energies. We have attempted to get a monomer distribution by fitting the clusters of peaks which show up consistently in the FIMS spectra. The scheme is outlined in Fig. 6. Starting with three basic single ring compounds with the probability for occurrence listed in column A, side chains (or 5 membered rings) are added with the probabilities in column B. Additional fused aromatic rings are added with the probabilities in column C and additional hydrogens to saturate the rings are added in column D. The probabilities shown are for the Pittsburgh Seam coal FIMS in Fig. 7c. The distribution of all possible combinations (the monomer distribution) is illustrated in Fig. 7a which compares reasonably well with the peak clusters in Fig. 7c. The dimer distribution is obtained by adding this distribution (minus 2 to account for the loss of hydrogen in the dimer bridge) to a second monomer distribution which includes molecular weights below 100 (introduced artificially by taking off one fused ring). The dimers were added to the monomers in a ratio of 3.1. This is a departure from the above theory which predicts that initially all oligomers are equally likely, but this compensates for the lack of trimers and tetramers. The resulting distribution is then convoluted with a vaporization probability to produce Fig. 7b which now has the peak clusters as well as the smooth background. The exercise shows that the assumed simple distribution is a possible choice. Other possibilities may also fit, but the choice must have sufficient regularities to produce the observed FIMS peaks.

The lignite molecular weight distribution is clearly controlled by processes other than vaporization as indicated by the lack of appreciable molecules above 200. Lignite is a non-softening solid. The rigid cross-linked nature of the molecular structure provides several possible explanations: (1) the cross-link density is so high and the available hydrogen for stabilization so low that there are very few dimers and trimers which can be released; (2) the rigid structure sterically hinders the escape of large molecules; (3) the rigid structure creates high pressures in the pores which hinders the escape of large molecules. These possibilities are currently under investigation.

CONCLUSIONS

1. Pyrolysis tars for a number of different hydrocarbons including softening coal, lignin and model polymers appear to be minimally disturbed fragments from the parent hydrocarbons. 2. FIMS spectra are useful in providing unfragmentated molecular weight distributions for tar. The spectra for coals are remarkably regular. All spectra have the same series of peak clusters. Rank variations show up as variations in the intensity of the peak clusters and in the amount and width of a smooth background. 3. The spectra of the simplest compounds (lignin and a model polymer) can be modeled by a theory which combines random cleavage of weak bonds to form oligomers which are small enough to vaporize. The theory predicts the correct trends for softening coals but not for lignite and low rank coals. 4. A speculative scheme for matching FIMS spectra of coals with an assumed monomer distribution appears to give reasonable results.

ACKNOWLEDGEMENT

The authors wish to acknowledge the support of this program by the Gas Research Institute under contract #5083-260-0582 and the Morgantown Energy Technology Center of DOE under contract #DE-AC21-81FE01522. The authors are grateful to Sydney Buttrill of Stanford Research Institute for his efforts in providing the FIMS spectra and to Dr. Buttrill and Professor Henk Meuzelaar of the University of Utah for helping interpret the mass spectra.

REFERENCES

1. Solomon, P. R., Hamblen, D. G. and Carangelo, R. M., ACS Symposium Series, 205, Coal and Coal Products: Analytical Characterization Techniques, American Chem. Soc., Washington, DC, (1982) pg. 77.
2. Solomon, P.R., Hamblen, D.G. and Carangelo, R.M., Analytical Pyrolysis of Coal Using FT-IR, 5th International Symposium, on Analytical Pyrolysis, Colorado, (1982).
3. St. John, G.A., Buttrill, S.E., Jr. and Anbar, M., "Field Ionization and Field Desorption Mass Spectroscopy Applied to Coal Reserach", in Organic Chemistry of Coal, (Ed. J. Larsen), ACS Symposium Series, 71, 1978 p. 223.
4. Solomon, P.R., The Synthesis and Study of Polymer Models Representative of Coal Structure, Final Report for GRI, Contract #5081-260-0582, Phase I, (April, 1983).
5. Meuzelaar, H.L.C. and Harper, A.M., and Given, P.H., Utah Geological and Mineral Survey, Bulletin 118, 192, (1982).
6. Meuzelaar, H.L.C., Harper, A.M., Hill, G.R., and Given, P.H., Characterization and Classification of Rocky Mountain Coals by Curie-Point Pyrolysis Mass Spectrometry, Fuel, (in press), (1984).
7. Harper, A.M. and Meuzelaar, H.L.C., and Given, P.H., Correlations Between Mass Spectra of Rocky Mountain Coals and Coventional Coal Parameters, Fuel, (in press), (1984).
8. Solomon, P.R., Hamblen, D.G., Carangelo, R.M., Markham, J.R. and DiTaranto, M.B., The Variation of Coal Pyrolysis Behavior with Rank, ACS Division of Fuel Chemistry Preprints, 29 (1984).
9. Anthony, D.B., Howard, J.B., Hottel, H.C., and Meissner, H.P., "Fifteenth Symposium (International) on Combustion", The Combustion Institute, Pittsburgh, PA, 1974, 1303.
10. Suuberg, E.M., Peters, W.A. and Howard, J.B., "Seventeenth Symposium (Int.) on Combustion", The Combustion Institute, Leeds, England, 1978, 117.
11. Unger, P.E. and Suuberg, E.M., "International Conference on Coal Science", Pittsburgh, PA, 1983, 475.
12. Unger, P.E. and Suuberg, E.M., "Molecular Weight Distributions of Tars Produced by Flash Pyrolysis of Coals", Submitted to Fuel (Jan. 1983).
13. Unger, P.E. and Suuberg, E.M., ACS Division of Fuel Chemistry Preprints, 28, #4, 278, (1983).
14. Unger, P. E. and Suuberg, E. M. "Eighteenth Symposium (International) on Combustion", The Combustion Institute, Pittsburgh, PA, 1981, 1203.
15. Gavalas, G. R.,Cheong, P. H. and Jain, R. Ind. Eng. Chem. Fundam., 1981, 20, 113 and 122.
16. Gavalas, G. R., and Wilks, K.A., AIChE Journal, 26, 201, (1980).
17. Solomon, P.R. and King, H.H. Tar Evolution from Coal and Model Polymers: Theory and Experiments, submitted to Fuel (1983).
18. Gavalas, G.B., and Oka, M., Fuel, 57, 285, (1978).
19. Lowry, H.H., "Chemistry of Coal Utilization", John Wiley & Sons, Pub., 1963.
20. Suuberg, E.M., (Private Communication).
21. King, H.H., Solomon, P.R., Avni, E. and Coughlin, R., ACS Division of Fuel Chemistry Preprints, 28, #5, 319 (1983).

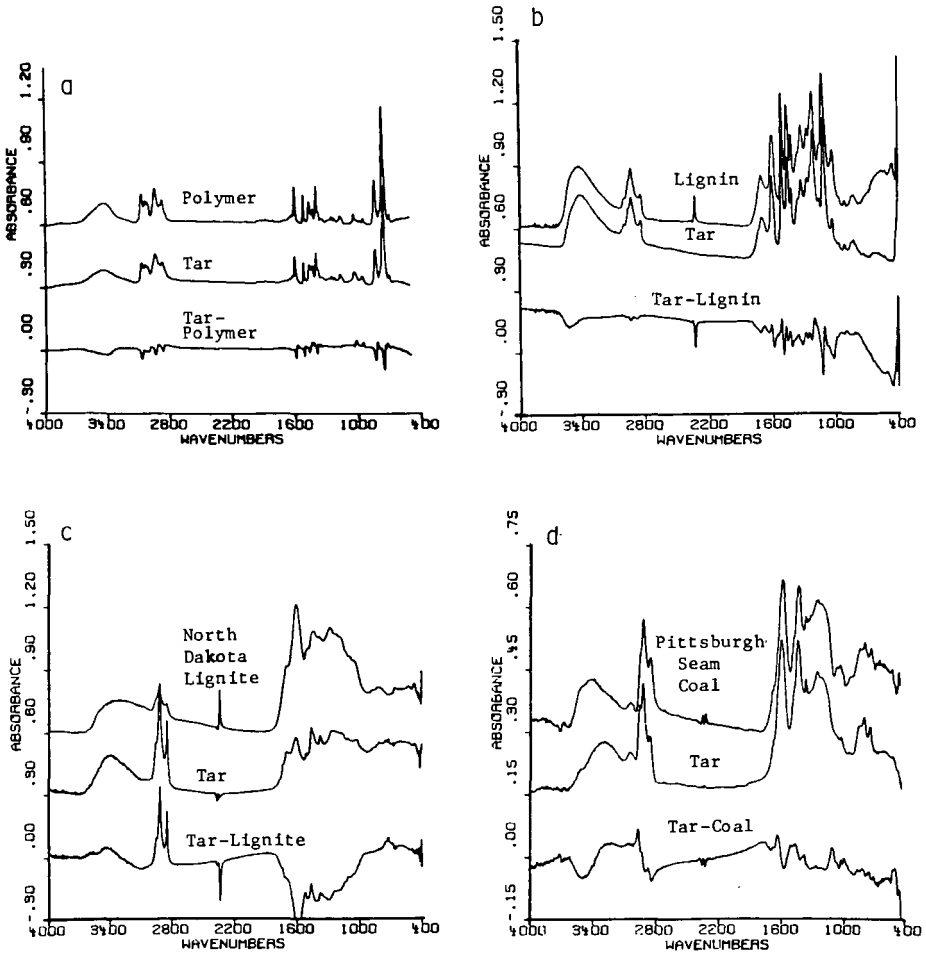

Figure 1. Comparison of FT-IR Spectra of Hydrocarbons and their Pyrolysis Tars.

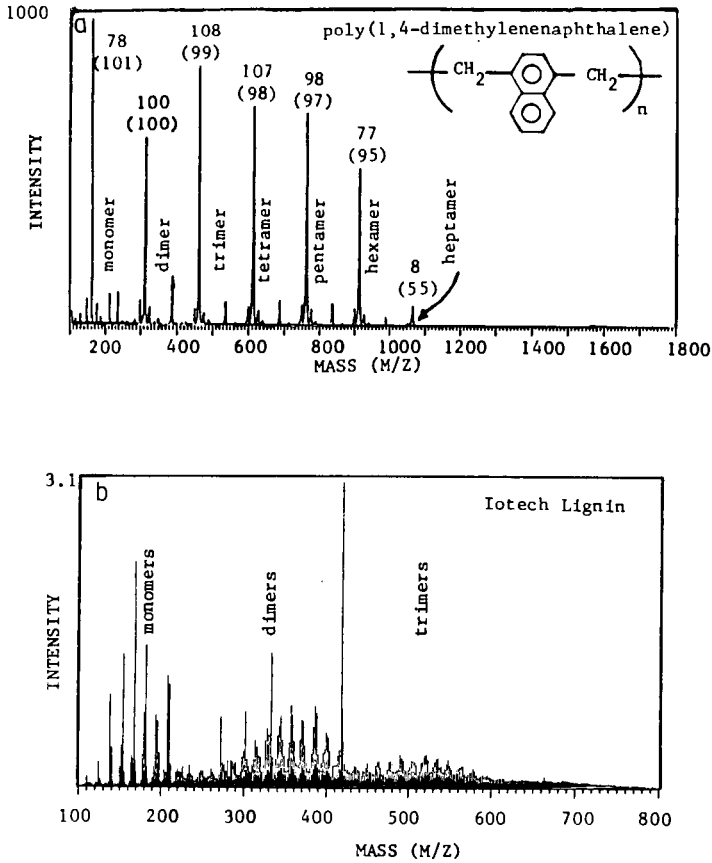

Figure 2. FIMS Spectra of two Hydrocarbons.

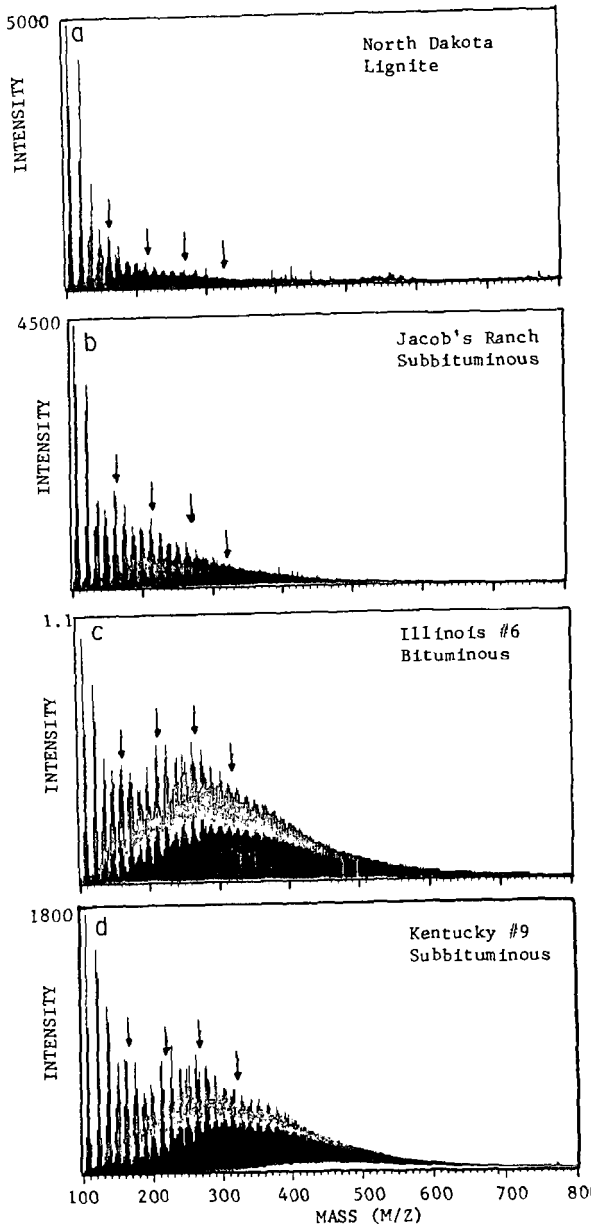

Fiugre 3. FIMS Spectra of a Lignite and 3 Coals. Arrows designate larger Peaks which begin Series of 4 Peak Clusters.

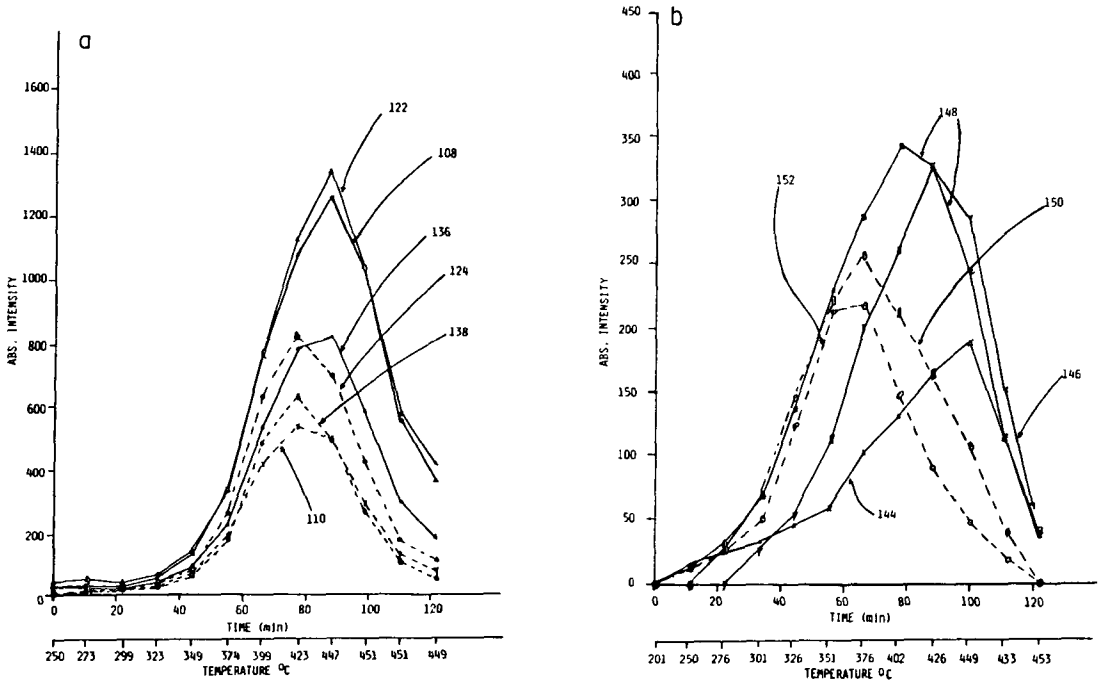

Figure 4. Intensity of Individual Mass Peaks as a Function of Pyrolysis Temperature.

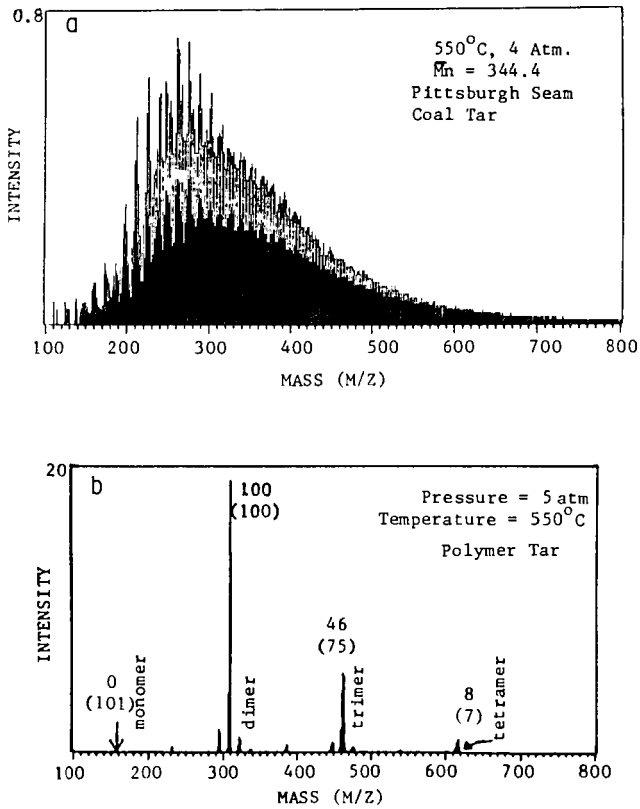

Figure 5. FIMS Spectra of two Hydrocarbon Tars Produced at Elevated Pressure. Spectra for Tars from the same Hydrocarbon produced in Vacuum are presented in Figs. 2a and 7c.

a BASIC COMPOUND			b SIDE GROUPS			c ADDITIONAL FUSED RINGS			d RING SATURATION		
MW	Compound	Probability	MW	Group	Probability	MW	Number of Rings	Probability	MW	Number of Hydrogens	Probability
106		0.2	0	-	1.0	0	-	1.0	0	0	.25
			12	C	0.1	50	1	.6	2	2	.25
			14	CH_2	1.0	100	2	.6	4	4	.5
108		1.0	24	C_2	0.1	150	3	.6	6	6	.25
			26	C_2H_2	0.2	200	4	.3	10	10	.25
			28	C_2H_4	0.5	250	5	.2			
110		0.3	36-42	$C-C_2H_6$	0.25	300	6	.1			
			48-56	$C_4-C_4H_8$	0.15						
			60-70	$C_5-C_5H_{10}$	0.07						

Figure 6. Compounds and Probabilities for Monomer Distribution in a Pittsburgh Seam Coal.

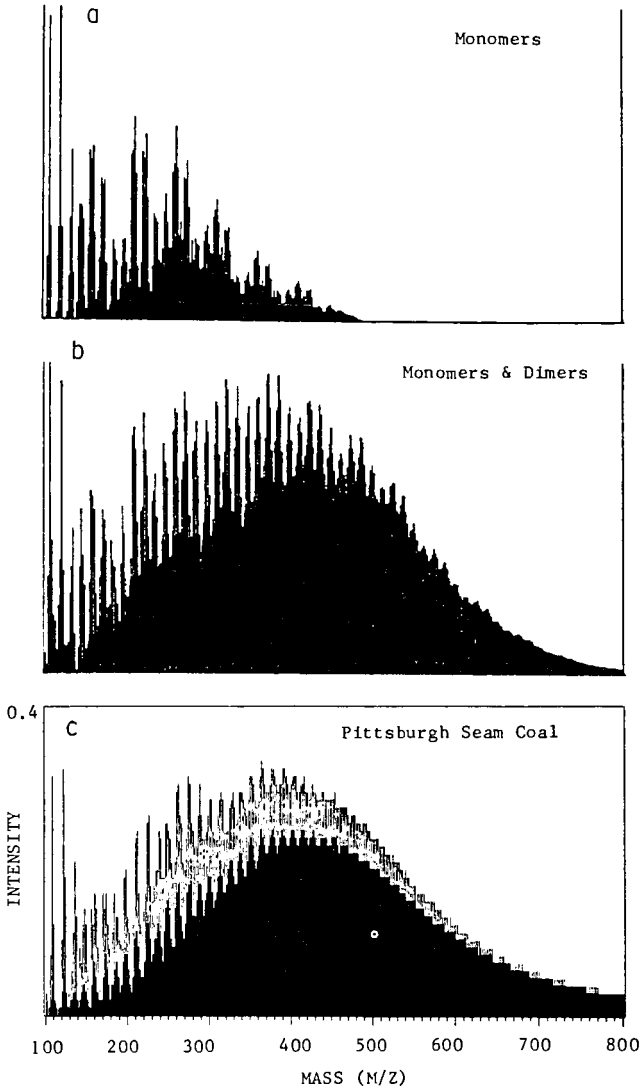

Figure 7. FIMS Spectra for a Pittsburgh Seam Coal (c) and Synthesized Spectra for Monomers and Monomers Plus Dimers.

INVESTIGATION OF ORGANIC STRUCTURAL CHARACTERISTICS OF LOW-RANK COAL LITHOTYPES

S.A. Benson, K.S. Groon, G.G. Montgomery, and H.H. Schobert

University of North Dakota
Energy Research Center
Box 8213, University Station
Grand Forks, North Dakota 58202

Introduction

The structural characteristics of low-rank coals and separated lithotypes were examined by several techniques. The bulk of the work was accomplished with pressure differential scanning calorimetry (PDSC). Supplemental information regarding functional groups was generated by electron spectroscopy for chemical analysis (ESCA) and infrared spectroscopy (IR). Aromaticities were calculated from the PDSC thermogram by a peak height ratio method which has been used in the past on whole coals, organic compounds, and polymers (1, 2). Aromaticities were determined for whole coals and separated lithotypes (fusain, durain, and vitrain). The fusain is the most aromatic of the lithotypes, with aromaticities ranging from 0.67 to 0.80. Calculations made using the proportions of each lithotype present in the coal determined a weighted aromaticity which corresponds very closely to aromaticity on the whole coal. ESCA was used to examine the carbon 1s peak for whole coal and lithotypes. Correlations were made between the relative abundances of C-C, C=O, and C-O bond types and coal lithotype. In nearly all cases, fusain had the largest ratio of C-C bonds. The spectral modes in the infrared which showed significant differences with lithotype include C=O and C-H stretching.

Methods and Procedures

Five low-rank coals and associated lithotypes listed in Table 1 were obtained from mines in the Fort Union and Powder River regions. The whole coals originated from channel samples representing one vertical section of the mine. Lithotypes were separated from samples taken near the location of the channel. The lithotypes were separated into three basic types based on megascopic differences. The vitrain is a very hard, vitreous lithotype. Durain has a dull, woody appearance and is soft compared to vitrain. The fusain is charcoal-like and very fragmental.

TABLE 1. COAL MINE LOCATION DESCRIPTION

Mine	Rank	County	State	Region	Seam
Beulah	Lignite	Mercer	North Dakota	Fort Union	Beulah-Zap
Indian Head	Lignite	Mercer	North Dakota	Fort Union	Beulah-Zap
Velva	Lignite	McHenry	North Dakota	Fort Union	Coteau
Glenharold	Lignite	Mercer	North Dakota	Fort Union	Scranton
Gascoyne	Lignite	Bowman	North Dakota	Fort Union	Harmon
Spring Creek	Subbituminous	Big Horn	Montana	Powder Creek	Dietz

A DuPont 1090 Thermal Analyzer system with a pressure DSC cell was used, to determine aromaticity. Details of this procedure have been published elsewhere (1, 2). Briefly, the procedure to determine the aromaticity involves hermetically sealing between 0.5 to 1.5 mg sample in an aluminum pan with a small hole punched in the

lid; the sample is then heated linearly from 150° to 600°C at 20°C/min under 500 psi oxygen to obtain the thermogram. The aromaticity is calculated from the thermogram as explained in the following section.

Samples were analyzed by transmission infrared spectrophotometry in an attempt to determine qualitative differences in functional groups among lithotypes. The dry coal spectra were obtained using KBr pellets. Appropriate amounts of coal and KBr were used to give a 0.4% or less coal to KBr mixture.

ESCA was used to determine the relative amounts of carbon as C-C, carbon bonded only to carbon or hydrogen; C-O, carbon in ether or phenol groups; and C=O, carbon in carboxyl or carbonyl groups. Samples used for ESCA analysis consisted both of ground samples and whole pieces of coal. The ground samples were pulverized to pass a 200 mesh sieve and pressed into 12.5 mm pellets using a standard laboratory press. The whole pieces of coal were attached to the sample holder with double stick tape and metal clips. Analysis was done using a Physical Electronics model 548 ESCA system. The sample bell jar was maintained at 10-100 nPa. Analysis time was approximately 30 minutes, using an analyzer pass energy of 25 eV. The x-ray beam was 5 mm in diameter to insure a large spectral area. The spectra were corrected for charging by assigning the hydrocarbon C-C peak to -284.6 eV. The spectra were resolved into components using a curve fitting routine employing a Gaussian-Lorentzian function to separate the carbon 1s peaks (3).

Results and Discussion

Aromaticities and temperatures of the peak maxima were determined for whole coals and lithotypes by the PDSC thermograms. The thermograms produced by the PDSC experiment of lithotypes from the Velva mine of North Dakota are shown in Figure 1. The apparent aromaticity, f_a', of these samples was found by dividing the height of the high-temperature peak of the thermogram by the sum of the heights of both peaks. The corrected aromaticity, f_a, was then calculated by the empirical equation $f_a = 0.263 + 0.868\ f_a'$ (1). (Preliminary work (1) suggests that different equations for calculating f_a from f_a' may be needed for different lithotypes; however, until further data is forthcoming, the equation given above will be used.) The results show that fusain is the most aromatic while durain and vitrain have lesser but similar aromaticities. The peak temperatures of the aromatic region of the PDSC thermogram were measured to determine the amount of ring condensation (1).

Five lignites and one subbituminous coal were examined by the PDSC method. The results indicate that the fusain was consistently the most aromatic of the lithotypes. The durain and vitrain of each coal were always lower, but similar to each other, in aromaticity. The peak temperatures and corrected aromaticities of all six coals and their lithotypes are summarized in Table 2.

The temperature of the aromatic peak (high-temperature peak) is important when determining the number or average number of aromatic clusters in coal. Figure 2 is a plot of the temperature of the aromatic peak versus the number of fused rings. This plot was prepared from thermograms of model compounds and polymers of known structure containing one to five fused rings. In general, most of the compounds lie within the band bounded by straight line rising at an angle of approximately 15 degrees. The temperature of the aromatic peak has been plotted for a series of run-of-the-mine coals as a function of rank, where P is peat, L is lignite, etc. Most of the coals fall within the band depicted by the dashed lines with a slow curve upward.

TABLE 2. PEAK TEMPERATURE AND AROMATICITIES OF COALS

Sample Description	Peak Temperatures, °C Low	High	Corrected Aromaticity, f_a
Beulah (whole)	275	375	0.66
B-12 Fusain	290	390	0.88
B-12 Durain	280	365	0.66
B-12 Vitrain	295	375	0.65
Indian Head (whole)	275	360	0.68
IH-1 Fusain	280	390	0.77
IH-4 Durain	275	360	0.71
IH-4 Vitrain	280	380	0.71
Velva (whole)	285	350	0.70
V-5 Fusain	300	375	0.86
V-5 Durain	280	355	0.65
V-5 Vitrain	280	360	0.66
Glenharold (whole)	280	350	0.63
GH Fusain	270	350	0.67
GH Durain	275	345	0.62
GH Vitrain	275	345	0.63
Gascoyne Blue (whole)	380	380	0.57
GB Fusain	290	395	0.78
GB Durain	290	390	0.71
GB Vitrain	285	390	0.54
Spring Creek			
SP Fusain	297	400	0.77
SP Durain	285	400	0.69
SP Vitrain	285	400	0.74

The amount of ring condensation observed by the position of the aromatic peak in the thermograms can be determined by comparison to Figure 2. The extent of ring condensation was determined for lithotypes. The results suggest that fusain ranges from 2½ to 3½ ring clusters, durain ranges from 1 to 3½ ring clusters, and vitrain ranges from 1 to 3½. The average ring condensation for the composite samples ranges from 1½ to 2½. If vitrain and durain are considered to be derived from plant materials with little chemical alteration relative to fusain, it is reasonable to expect low values of ring condensation. Lignin would have a ring condensation number of 1, since the lignin structure is based on phenylpropane moieties. The more extreme thermal conditions which may have led to the formation of fusain would result in a greater aromatization, cross-linking, and condensation of rings.

The approximate amounts of lithotypes in the coals studied averaged 5% fusain, 40% durain, and 45% vitrain. The experimental aromaticities of the composite coals agree with values calculated from weighed aromaticities as shown in Table 3.

An example of an ESCA spectrum, for the carbon 1s region, is shown in Figure 3. The spectrum is resolved into separate peaks assigned to the C-O, C=O, and C-C bond types. The peak assignments are based on analogy to model polymers, particularly polyethylene terephthalate (3). The C-C peak was corrected to -284.6 eV to account

TABLE 3. CALCULATED VERSUS EXPERIMENTAL AROMATICITIES

Coal	Corrected Aromaticity of Lithotype			Calculated Aromaticity For Whole Coal	Calculated Aromaticity For Whole Coal
	Fusain	Durain	Vitrain		
Beulah	0.80	0.66	0.65	0.66	0.66
Indian Head	0.77	0.71	0.71	0.71	0.68
Velva	0.86	0.65	0.66	0.66	0.70
Glenharold	0.67	0.62	0.63	0.63	0.63
Gascoyne Blue	0.78	0.71	0.54	0.64	0.57

for the effects of sample charging. The ratios of individual peak intensities to the total intensity in the carbon is region are summarized in Table 4 for Beulah and Gascoyne lignites and their lithotypes. (The ratios of peak intensities to total intensities are shown because, for a series of experiments, the total intensity will vary from sample to sample depending on such factors as duration of the experiment and whether the sample is a chip or powder.) The relatively high concentration of C-C bonds in fusain as determined by ESCA is in agreement with the relatively high aromaticities of this lithotype determined by PDSC. The high aromaticity, reduced levels of oxygen functional groups, and the high proportion of oxidized (ie, C=O) functional groups among those remaining in fusain are all consistent with the concept that fusain has been exposed to severe thermal conditions at some point in the coalification process. The ratios of bond types for the composite sample of Beulah lignite are 0.37 for C=O/C-O and 0.09 for C=O/C-C; these agree fairly well with previously published values of 0.44 and 0.12 from ESCA examination of a different sample of Beulah lignite (3). However, as we have discussed elsewhere (3) it is desirable to incorporate data from several techniques or instruments before attempting to draw structural inferences.

TABLE 4. C=O, C-O, and C-C RATIOS DETERMINED FOR ESCA CARBON 1s SPECTRUM

Coal	C=O	C-O	C-C
Gascoyne (whole)	0.03	0.19	0.78
Fusain	0.07	0.03	0.90
Durain	0.04	0.15	0.81
Vitrain	0.04	0.10	0.86
Beulah (whole)	0.07	0.19	0.74
Fusain	0.09	0.05	0.86
Durain	0.05	0.16	0.79
Vitrain	0.0	0.21	0.88

The infrared spectra for the Beulah coal and lithotypes are shown in part in Figure 4. The intensity of the aliphatic C-H stretches for durain is much greater than that of fusain and the whole coal. The peak at 1700 cm^{-1} is most pronounced in the fusain spectra and appears as shoulders in the others. This peak may be assigned to carbonyl (C=O) stretching. The ESCA data indicates a higher concentration of C=O for fusain, providing qualitative agreement between the ESCA and IR data.

Conclusions

PDSC analysis of lithotype samples has shown that fusain is invariably the most aromatic of the lithotypes of these low-rank coals. Durain and vitrain have usually shown aromaticities similar to each other and significantly lower than fusain. It has been shown that experimental values obtained for the lithotypes could be weighted according to the approximate percentage of each lithotype in the coal, and a value for the whole coal could be calculated which compared quite well with the actual, experimental value. This correlation was especially significant when aromaticity values were used.

The correlations noted between the PDSC, ESCA, and IR include aromaticities and functional group analysis. The aromaticities determined by PDSC are supported by the ESCA C-C ratio, where in most cases fusain is the most aromatic. The unique features of the PDSC thermograms for vitrain are supported by ESCA data. For example, the shoulder peak at 400°C is an indication of increased aromatization. The C-C ratio from the ESCA spectra of vitrain is nearly as high as that of fusain but in the Beulah the vitrain C-C ratio was greater. The aliphatic nature of durain is shown by the aliphatic C-H stretching in the infrared spectra being relatively greater than in the spectra of the other lithotypes. High amounts of carboxyl content (C=O), supported by both ESCA and IR evidence, was characteristic of fusain.

The structural relationships of low-rank coals and associated lithotypes determined by ESCA, PDSC, and IR provides a means of examining coal aromaticities and functional groups. The techniques are relatively fast and help provide insight into the molecular "structure" of low-rank coals.

Acknowledgment

The authors would like to thank David Kleesattel for separating the lithotypes. Ms. Groon was supported by an Associated Western Universities summer research participation grant.

References

1. Benson, S.A. and H.H. Schobert. Structural Characteristics and Relationships in Low-Rank Coals. In Technology and Use of Lignite. U.S. Department of Energy Report GFETC/IC-82/1, p. 442-70, 1982.

2. Benson, S.A., K.S. Groon, and H.H. Schobert. Pressure Differential Scanning Calorimetry of Coals, Organic Compounds, and Polymers. Proceedings, 12th North American Thermal Analysis Society Conference, Williamsburg, Virginia, p. 22-36, September 1983.

3. Schobert, H.H., G.G. Montgomery, M.J. Mitchell, and S.A. Benson. Characterization of the Organic Structure of U.S. Lignites by Electron Spectroscopy and Thermal Analysis. Proceedings, 9th International Conference on Coal Science, Pittsburgh, Pennsylvania, p. 350-353, August 1983.

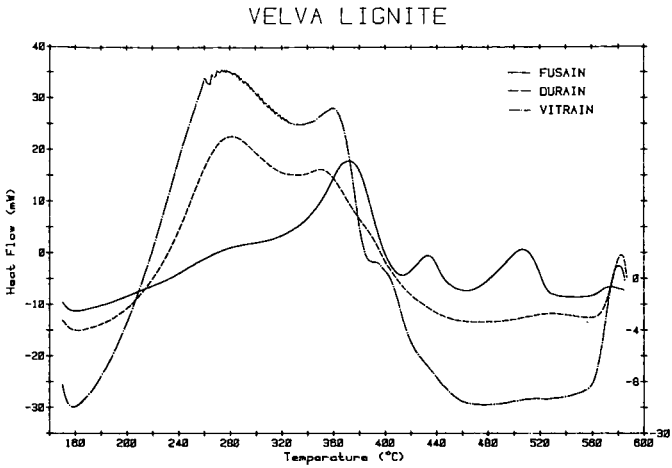

FIGURE 1. PDSC thermograms of lithotypes from the Velva, North Dakota mine.

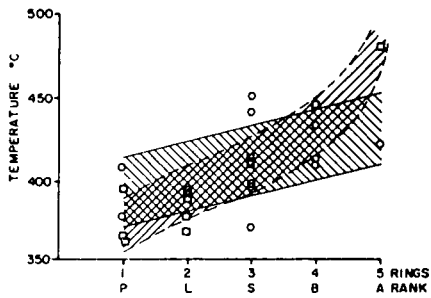

FIGURE 2. Temperature of aromatic peak as a function of number of fused rings for pure compounds (circular points; trend shown by band outlined with solid straight lines) or as a function of rank (square points; trend shown by band outlined with dashed curving lines) (1).

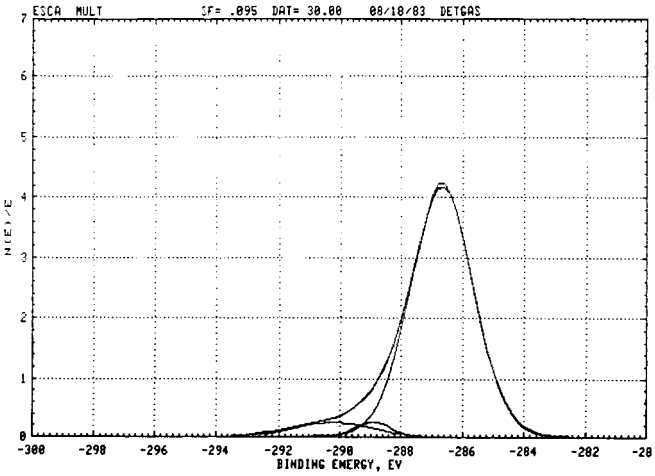

FIGURE 3. ESCA carbon 1s spectra of Gascoyne vitrain.

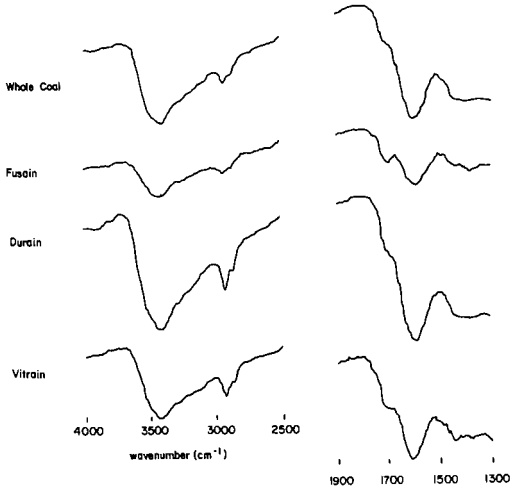

FIGURE 4. IR spectra of Beulah coal and lithotypes.

CONCERNING THE CALCULATION OF COAL STRUCTURAL PARAMETERS FROM SPECTROSCOPIC DATA

P. Painter, M. Starsinic, E. Riesser, C. Rhoads and B. Bartges

Materials Science and Engineering Department
Steidle Building
The Pennsylvania State University
University Park, PA 16802

Because of the heterogeneous, multicomponent nature of coal, much structural analysis work has been channelled towards the determination of parameters that can be used to describe "average" structures. In principle, FT-ir measurements can be used to quantitatively determine the aliphatic CH, aromatic CH and OH content of coal (1-5), while solid state ^{13}C nmr spectroscopy can be used to determine the relative proportions of aromatic to aliphatic carbon (6-9). There is much active research aimed at extending the scope of these techniques to allow the measurement of additional functionalities. Nevertheless, with these measurements alone a number of fundamental structural parameters (H_{ar}/C_{ar}, H_{al}/C_{al}, H_{ar}/H_{al} etc.) can be calculated. Furthermore, with the measurement of one additional parameter, the number of methyl groups (as measured by the fraction of aliphatic carbon or hydrogen involved in such groups), it should be possible to determine the distribution of aliphatic carbon (ie. the relative proportions of CH, CH_2 and CH_3 groups) and then describe a"mean structural unit" in terms of average aromatic ring size and the type and distribution of bridging units and substituents. This can be accomplished by using the equations originally described by van Krevelen and Schyuer (10) and utilized by Dryden (11,12) for statistical structural analysis. Similar equations were also derived by Brown and Ladner (13) in order to utilize the data that was then becoming available from proton n.m.r. measurements. However, there were a number of uncertainties in applying these equations. Dryden used data from elemental analysis together with estimates of aromaticity and other parameters (eg. alicyclic hydrogen) that were to some degree uncertain. An iterative procedure was used to solve the equations. The application of the Brown-Ladner equation required assumptions concerning the aliphatic hydrogen-to-carbon atomic ratio. Quantities such as this can now be determined directly from combined FT-ir/^{13}C nmr measurements. We therefore considered that it might be a relatively straightforward task to calculate mean structural units for the coal samples for which we have accumulated spectroscopic data (4,9). And it is. Unfortunately, a major problem arises once we consider whether or not the numbers so derived mean anything. We will show that for an individual coal they do not. The form of the equations are such that errors accumulate dramatically and our spectroscopic measurements are insufficiently precise to obtain anything but a broad description of trends as a function of rank. We will first consider the data obtained for a set of vitrinite concentrates and specifically the problems with the FT-ir data. We will then demonstrate how even small errors in this data dramatically affect the calculation of structural parameters.

The fraction aromaticity, f_a, can now be determined with what is considered to be reasonable precision by ^{13}C nmr using cross-polarization and magic angle spinning. It is probably more accurate to say that most fuel scientists are comfortable with the values of f_a so derived, because there are a number of sources

of possible error and these are not easily quantified. For the sake of the arguments we wish to make here we will assume (optimistically) that the values of f_a are good to $\pm$ 5%. Values of f_a for a set of vitrinites reported previously (9) are combined with more recent measurements of additional samples by Martzel and Koenig (14) and Pugmire and Grant (15) in figure 1. There is some scatter, but a reasonably narrow band of values is apparent.

Unlike nmr measurements, where the ratio of peak areas is equal to the ratio of aromatic to aliphatic carbon, bands in the infrared spectrum require calibration. They are related to the concentration of the appropriate functional group through an absorption coefficient which is different for each band. This has led to all sorts of trouble and a variety of values of aromatic to aliphatic hydrogen ratio's can be found scattered throughout the literature. We will not discuss the various methods that can (and have) been used to calibrate infrared bands, this ground is covered elsewhere (5). In terms of the points we wish to make here, the actual values of H_{al} and H_{ar} are to some degree irrelevant, as we will be more concerned with the effects of errors in these values on subsequent calculations of structural parameters. Nevertheless, it is important and illuminating to consider one factor that is probably central to many of the discrepancies found in the literature. If we take a bituminous coal of, say 82% carbon content, we typically determine an aliphatic hydrogen content close to 4% and an aromatic hydrogen content of about 1%. There are numerous errors that can affect these measurements, but these are not simply cumulative. For example, if errors in sample preparation, band areas etc. were of the order of $\pm$10%, we might be able to quote values of 4$\pm$0.4% and 1$\pm$0.1% for aliphatic and aromatic CH content, respectively. However, the absorption coefficients for aliphatic and aromatic CH bands are presently being determined by equating band areas to hydrogen content determined from elemental analysis (1,5). If a sample has negligible COOH content we can write

$$H = H_{OH} + H_{ar} + H_{al} \qquad (1)$$

where H is the hydrogen content determined by elemental analysis, and H_{OH}, H_{ar} and H_{al} is the hydrogen found as OH, aromatic CH and aliphatic CH, respectively. This can be rewritten as;

$$(H - H_{OH}) = I_{ar}\,\varepsilon_{ar} + I_{al}\,\varepsilon_{al} \qquad (2)$$

where I is the intensity of the appropriate infrared band and ε is a conversion factor (equivalent to the reciprocal of the absorption coefficient in appropriate units) relating band area to corresponding hydrogen content. Theoretically, data from a set of coals can be used and ε_{ar} and ε_{al} determined graphically (1) or by obtaining numerical solutions to the resulting simultaneous equations (3,5). We have recently shown, however, that these equations are clasically ill-conditioned (5). In other words, a range of solutions gives almost equally acceptable answers. We have spent a lot of time trying to pin down the "correct" answer, and the values we have recently come up with (5) are somewhat different to those originally reported (3). The key point here, however, is that the ill-conditioned nature of the equations means that the values of H_{ar} and H_{al} determined in this fashion are somewhat dependant. In other words, a 10% error in determining ε_{al} and hence H_{al} translates into a much larger error in H_{ar}. This is because the values of ε_{ar} obtained from solutions to equation 2 will be adjusted to account for as much of the hydrogen as possible. Accordingly, if H_{al} is calculated to be 4$\pm$0.4%, H_{ar} will be calculated to be 1$\pm$0.4%. A 10% error in ε_{al} (hence A_{al}) translates into a <u>40%</u> error in ε_{ar} (and H_{ar}). As a result, even

though the values of the absorption coefficients we have recently determined for the aliphatic CH stretching modes (5) are not far off the more recent values reported by Solomon (2), we still calculate vastly different values of H_{ar}/H_{al}.

Undaunted by these difficulties, we have reproduced our values of H_{ar}/H_{al} for a wide range of coals and vitrinite concentrates in figure 2. The knowledgeable reader will immediately recognize that for coals with a carbon content of 85% or higher these results are very similar to those reported by Brown (16) more than twenty five years ago. For lower rank coals Brown's results fall near the bottom of our band of values. The scatter in the data is not more than we would have intuitively estimated on the basis of coal heterogeneity. This is because these results are obtained by ratioing infrared bands and thus cancelling errors from a number of sources (eg. weighing, insufficient grinding, improper corrections for moisture and mineral contents of the coal). When we consider values of H_{al} and H_{ar} separately, however, these errors return with a bang, as can be seen in the plots shown in figure 3 for the vitrinite concentrates. This, unfortunately, has dire consequences for the calculation of structural parameters.

Before turning our attention to the calculation of these parameters, we will briefly mention measurements of methyl groups by FT-ir. The most easily recognized group frequencies for methyl groups are the stretching modes near 2960 and 2870 cm^{-1} and the symmetric bending mode near 1380 cm^{-1}. The overlap of these bands with other modes is severe and even sophisticated curve resolving procedures cannot entirely separate out the contributions of other functional groups. When methyl groups are attached to aromatic rings, however, a weak overtone band appears near 2730 cm^{-1} (17). This band is well separated from other modes and the precision of FT-ir measurements is such that its band area should be measurable with reasonable accuracy. The process is not entirely straightforward due to problems with establishing a baseline in this region of a typical coal spectrum (the position of the baseline can dramatically affect the measured area of an infrared band). This problem and its solution is discussed elsewhere (18). An absorption coefficient for this band was determined from model compounds. Unsurprisingly, this coefficient did not vary significantly amongst a variety of methyl substituted aromatic materials. This is because many of the methyl vibrational modes are not sensitive to the size and nature of the aromatic entity to which it is attached. We determined that for vitrinite concentrates obtained from bituminous coals the %C found as methyl groups attached to aromatic units varied between 3 and 5% (with one or two outside this range). These numbers agree very well with the total methyl content recently determined by ^{13}C nmr for some of the same vitrinites by Pugmire and Grant (15). Presumably, in vitrinites there are very few methyl groups present in ethyl, propyl or similar units. (This is not the case for exinites, which are much more aliphatic. We again determine that approximately 4%C is tied up in methyl groups attached to aromatic rings, but nmr analysis indicates a total methyl content of approximately 7%).

Given that we can determine reasonably accurate values for the relative proportions of aliphatic and aromatic carbon from ^{13}C nmr, aliphatic and aromatic hydrogen from FT-ir and methyl group concentration from either or both techniques, what can we calculate and to what extent does it mean anything? Space does not permit us to consider all the equations utilized by Dryden (11,12) and Brown and Ladner (13), but a relatively simple example indicates the problem. The following two equations can be used to describe the distribution of aliphatic groups;

$$H_{al} = H_{CH} + H_{CH2} + H_{CH3} \quad (3)$$

$$C_{al} = C_{CH} + C_{CH2} + C_{CH3} \quad (4)$$

The concentration of hydrogen and carbon present in aliphatic groups, H_{al} and C_{al}, can be determined from FT-ir and ^{13}C nmr, respectively. The % hydrogen and carbon present in methyl groups, H_{CH3} and C_{CH3}, can also be determined as discussed above. This leaves two equations in two unknowns. Consequently, we should be able to determine the distribution of aliphatic species in any particular coal. Consider, however, a typical example. A vitrinite concentrate (PSMC 71, 85.2%C) with f_a=0.73, H_{al}=3.5% and C_{CH3}=3.6%. Solving equations (3) and (4) gives values of C_{CH2} = 11.8% and C_{CH}=7.6%. Now consider the effects of relatively modest errors. For example, if we optimistically decide that f_a is equal to 0.73 $\pm$ 0.2 and H_{al} is equal to 3.5 $\pm$ 0.2%, we can determine a range of values of C_{CH2} and C_{CH} corresponding to the upper and lower limits of these values. The values of C_{CH2} now fall in the range 15.1% to 2.2% while C_{CH} falls in the range 4.5% to 16.2%! Clearly for any <u>single</u> sample even small errors multiply to such an extent that it is not possible to define structural parameters with any degree of precision or confidence.

This situation is not confined to the simple example given above. For example, we previously (9) used the Brown-Ladner equation (13) to calculate the aliphatic hydrogen to carbon atomic ratio, H_{al}/C_{al}:

$$f_a = [C/H - H^*_{al}/(H_{al}/C_{al})]/C/H \quad (5)$$

where H^*_{al} is the fraction of total hydrogen present as aliphatic groups. Assuming errors of approximately $\pm$5% in values of f_a it was found that proportionally much larger errors were calculated in H_{al}/C_{al}, these errors increasing proportionally with rank. This is because H_{al}/C_{al} actually varies with the reciprocal of (1-f_a), so that errors in f_a become increasingly significant. [For example, even <u>small</u> errors in f_a for a high rank coal, say 0.9 $\pm$0.02 or $\pm$2% results in much larger errors in (1-f_a); 0.1$\pm$0.02 or $\pm$20%!].

Clearly, the accurate calculation of structural parameters for any <u>specific</u> coal is almost pointless, given the precision of the data presently available. Nevertheless, broad averages and trends as a function of rank can be determined. If we take the plots of f_a, H_{al}, H_{ar} etc. reproduced in figures 1 thru 3, then we can draw lines through the data. At any particular value of %C we can then read off these plots values that represent an "average" parameter value for coals of that rank. These average values can then be used to calculate structural parameters. This procedure is limited and unsatisfactory, but given the major effects experimental errors have on the data, it is the best we can do at this time. If nothing else they show trends as a function of rank. As an example a plot of the distribution of aliphatic CH groups is shown in figure 4. It can be seen that the proportion of CH_2 to CH groups increases as a function of rank, while the experimentally determined %C as CH_3 groups remains approximately constant.

References

1. Solomon, P. R. ACS Division of Fuel Chemistry Preprints, 24 #3, 184 (1979).
2. Solomon, P. R. Hamblen, D. G. and Carangelo, R. M. in "Coal and coal products. Analytical Characterization Techniques" E. L. Fuller, Ed. ACS Symposium Series #205, 77 (1982).

3. Kuehn, D. W., Snyder, R. W., Davis, A. and Painter, P. C. Fuel, 61, 682 (1982).
4. Snyder, R. W., Painter, P. C., Havens, J. R. and Koenig, J. L. Applied Spectroscopy (In press).
5. Riesser, E., Starsinic, M., Squires, E., Davis, A. and Painter, P. C. Fuel (In press).
6. Miknis, E. P., Maciel, G. E. and Bartuska, V. J. Org. Geochem. 1, 169 (1979).
7. Miknis, E. P., Sullivan, M. and Maciel, G. E. Org. Geochem. 3, 19 (1981).
8. Ziln, K. W., Pugmire, R. J., Grant, D. M., Wood, R. E., Wiser, W. H. Fuel, 60, 717 (1981).
9. Painter, P. C., Kuehn, D. W., Starsinic, M., Davis, A., Havens, J. and Koenig, J. L. Fuel, 62, 103 (1983).
10. Van Krevelen, D. W. and Schuyer, J. "Coal Science" Elsevier (1957).
11. Dryden, I. G. C. Fuel, 37, 444 (1958).
12. Dryden, I. G. C. Fuel, 42, 55 (1962).
13. Brown, J. K. and Ladner, W. R. Fuel 39, 87 (1960).
14. Martzel. E. M. S. Thesis. Case Western Reserve University, Dept. of Macromolecular Science. (1983).
15. Pugmire, R. and Grant, D. Private communication, to be published.
16. Brown, J. K. J. Chem. Soc., 744 (1955).
17. Bellamy, L. J. The infrared spectra of complex molecules. Vol I, Third Edition Chapman and Hall, London (1975).
18. Starsinic, M. Ph.D. Thesis, The Pennsylvania State University (1984).

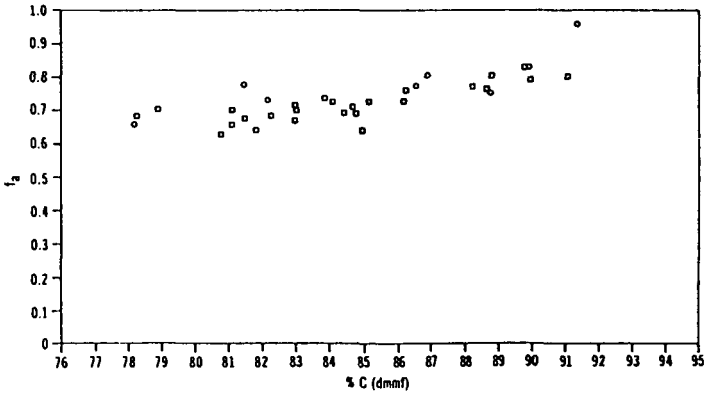

Figure 1. Plot of fraction aromaticity, f_a, vs %C dmmf for a set of vitrinite concentrates.

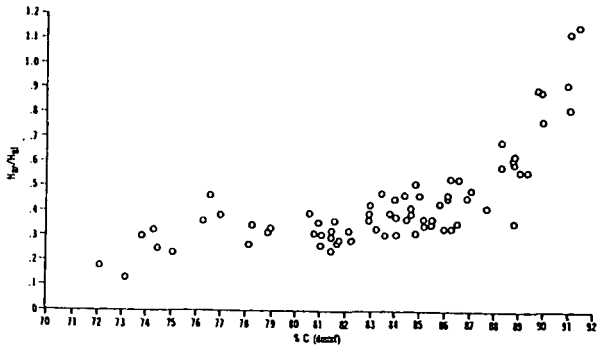

Figure 2. Plot of the ratio of aromatic to aliphatic hydrogen, H_{ar}/H_{al}, determined for a set of coals and vitrinite concentrates.

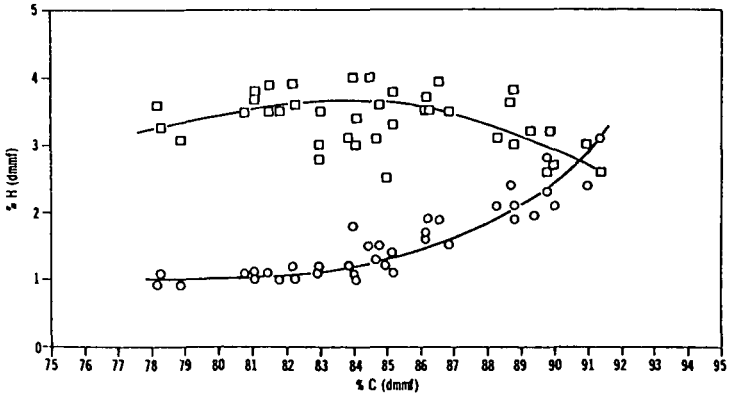

Figure 3. Plot of %H in aliphatic groups (top) and %H in aromatic groups (bottom) vs %C dmmf for a set of vitrinite concentrates.

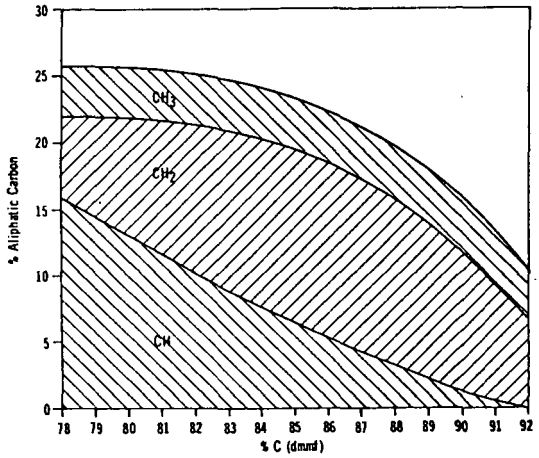

Figure 4. Plot of distribution of aliphatic groups as a function of rank of a set of vitrinite concentrates.

ASPHALTENE CHARACTERIZATION BY A NONSPECTROSCOPIC METHOD

Manuel A. Francisco
and
James G. Speight

Exxon Research and Engineering Co.
Clinton Township, Route 22 East
Annandale, New Jersey, U.S.A. 08801

INTRODUCTION

The emergence of the heavier crude oils as refinery feedstocks has become the accepted norm over the last decade (1). It is, however, a property of these feedstocks to be rich in asphaltenes (2,3,4) which are not very amenable to refinery processes and are usually responsible for coke lay-down and for catalyst deterioration (3,4).

The conventional definition of asphaltenes is based on the solution properties of petroleum residua in various solvents (5,6,7). This generalized concept has been extended to fractions derived from other carbonaceous sources, such as coal and oil shale. Thus, there are "petroleum asphaltenes", "coal liquid asphaltenes", "coal tar asphaltenes", "shale oil asphaltenes", "tar sand bitumen asphaltenes" and the like. With this extension, there has followed considerable scientific effort to further define asphaltenes in terms of molecular structures (9,10,11).

Nevertheless, it must always be recognized that asphaltenes (from whatever the source) are, in fact, a solubility class (Figure 1) and that the definition is, in fact, an operational one; that is, asphaltenes are soluble in benzene and insoluble in pentane. Usually, for virgin petroleum samples, the residuum is completely soluble in benzene. However, with heat-soaked samples or coal derived liquids, the benzene insolubles can be appreciable.

A more recent concept (14) extends the solubility classification of asphaltenes and involves, initially, a consideration of molecular weight vs. polarity for the molecular types found in petroleum residua and/or heavy oils (Figure 2). The polarity scale may be in definable arbitrary units, such as relative adsorptive strength on a solid, e.g. Attapulgus clay and/or silica gel (15), or by solubility in a variety of solvents of increasing polarity as practiced on separation of coal liquid fractions (13); this scale is thus a <u>molecular weight-independent</u> portion of the solubility parameter. For any particular

precipitating medium, say n-heptane, the precipitated asphaltenes will, therefore, consist of less polar materials of higher molecular weight and more polar materials of lower molecular weight; with n-pentane as the precipitating agent, both less polar and lower molecular weight materials are included in the precipitate and the total amount of precipitate increases (16,17). The concept also allows for a polarity range within the various asphaltenes where varying heteroatom (nitrogen, oxygen, and sulfur) contents of the petroleum asphaltenes or variations in the source (and method of preparation) that would be expected to influence polarity (18,19,20).

The present communication describes an extension to the concept of asphaltene polarity by the delineation of petroleum asphaltenes as a collage of functional types using ion-exchange chromatography.

EXPERIMENTAL

1. Feedstock

Arabian heavy crude oil vacuum (950°F+) residuum was used as the feedstock for all of these investigations.

2. Ion-exchange Fractionation

Separation of the feedstock by ion-exchange resins was carried out using a feedstock/solid ratio ~ 0.05* and the product fractions (Figure 3) were designated (a) bases; (b) acids; (c) neutral polars; and (d) neutral nonpolars.

3. Deasphalting

Separation into asphaltene and deasphalted oil fractions was achieved by mixing the fraction with n-heptane (1 gm. fraction:40 ml. n-heptane) at room temperature for 16 hr. with agitation. At the end of this time, the insoluble asphaltenes were separated by filtration and washed with fresh n-heptane (200 ml:1 gm. asphaltenes). The asphaltenes were "purified" from adsorbed material by dissolution in toluene (10 ml:1 gm. asphaltenes) and precipitated with n-heptane (80 ml:1 ml toluene); any soluble material was recovered and added to the deasphalted oil.

*The feedstock/resin ratio was computed on the basis of the number of active sites on the resin and is, therefore, subject to change and depends upon the nature of the resin.

4. General Techniques

Solvents were removed from the products by means of a Rotovap (60°C/40 mm Hg.) and final vestiges were removed by "drying" the products in vacuo (100°C/20 mm Hg).

RESULTS AND DISCUSSION

The application of chromatographic adsorption techniques to investigate functional and/or structural types in asphaltenes is not new (21,22) but problems of precise identification may be limited by the incomplete recovery of the asphaltene from the adsorbent, particularly when the functionalized ion-exchange adsorbents are employed. However, ion-exchange fractionation of whole feedstocks has been cited to result in an overall more complete recovery of the asphaltenes (23).

In the present work, it has been found preferable to fractionate the whole residuum by ion-exchange chromatography not only to build up a picture of the asphaltenes in terms of functional types but also to note the overall distribution of functional types in the whole feedstock as well as the nuances of the deasphalting technique.

Thus, fractionation of Arabian heavy crude oil vacuum residuum by ion-exchange chromatography produced a series of fractions (Table 1) of varying functionality which could also be differentiated by infrared spectroscopy (Figure 4).

Subsequent heptane-deasphalting of these fractions not only allows cross-referencing of the two techniques but also allows the deasphalted oil and the asphaltenes to be represented on the basis of the different functionalities (Figures 5 and 6).

Obviously, the chemistry and structural features of petroleum asphaltenes will be dictated by the distribution of functional/structural types separated as an artifact of the deasphalting technique. This makes the representation of the structure/functionality of these carbonaceous constituents of petroleum by "average" structures very difficult to conceive (11,18).

Such carbonaceous materials are, therefore, best represented by a series of structural and/or functional types that are best fitted to describe their chemistry/reactivity.

LITERATURE CITED

1. "The Future of Heavy Crude Oil and Tar Sands", R. F. Meyer and C. T. Steele (editors), McGraw-Hill, New York, 1981.

2. J. G. Speight, "Asphaltenes as an Organic Natural Product and their Influence on Crude Oil Properties", presented at the Div. of Geochemistry, Am. Chem. Soc., New York, August 23-28, 1981.

3. J. G. Speight, "Th Desulfurization of Heavy Oils and Residua", Marcel Dekker Inc., New York, 1981.

4. M. L. Gorbaty and J. G. Speight, "The Characterization of Heavy Oils and Residua", paper presented at the 28th IUPAC Conference, Vancouver, B.C., Canada, August 16-21, 1981.

5. "Annual Book of ASTM Standards; American Society for Testing and Materials, Philadelphia, Part 24, Standard No. D-2006", 1975, withdrawn 1976.

6. "Annual Book of ASTM Standards; American Society for Testing and Materials, Part 15, Proposed Standard for Asphalt Composition".

7. "Standards for Petroleum and Its Products, Standard No. 1P 143/57", Institute of Petroleum, London.

8. J. G. Speight, R. B. Long and T. D. Trowbridge, Preprints, Am. Chem. Soc. Div. Fuel Chem., 1982, 27, (3/4), 268.

9. J. G. Speight, Applied Spectroscopy Reviews, 1972, 5, 211, and references cited therein.

10. T. F. Yen, PREPRINTS, American Chemical Society, Division of Petroleum Chemistry, 1972, 17(4), F102, and references cited therein.

11. J. G. Speight, Preprints, Am. Chem. Soc., Div. Petrol. Chem., 1979, 24(4), 910.

12. J. D. Brooks and G. H. Taylor, Chem. & Phys. of Carbon, Vol. 4, 243 (1968) Marcel Dekker, New York.

13. M. Farcasiu, T. O. Mitchell, D. D. Whitehurst, A.C.S. Div. Fuel Chemistry Preprints, Vol. 21, No. 7, 11, (1976).

14. R. B. Long, Preprints, Am. Chem. Soc., Div. Petrol. Chem., 1979, 24(4), 891.

15. L. W. Corbett, Anal. Chem. 41, 576 (1969).

16. D. L. Mitchell, J. G. Speight, Fuel, 1973, 52, 149.

17. L. W. Corbett, and U. Petrossi, Ind. Eng. Chem. Prod. Res. Dev. 17, 342 (1978).

18. J. G. Speight and R. B. Long in "Atomic and Nuclear Methods in Fossil Energy Research", R. H. Filby (editor), Plenum Press, New York, 1982, 295.

19. J. G. Speight and S. E. Moschopedis in "The Chemistry of Asphaltenes", J. W. Bunger and N. C. Li (editors), Am. Chem. Soc., Adv. in Chem. Series No. 195, Washington, DC, 1981, 1.

20. J. G. Speight, "The Structure of Petroleum Asphaltenes", Information Series No. 81, Alberta Research Council, 1978; and J. G. Speight, "Geochemical Influences on Petroleum Constitution and Asphaltene Structure" presented at the Div. of Geochem., American Chemical Society, Washington, DC, September, 1979.

21. M. L. Selucky, S. S. Kim, F. Skinner and O. P. Strausz in "The Chemistry of Asphaltenes", J. W. Bunger and N. C. Li (editors), Am. Chem. Soc., Adv. in Chem. Series No. 195, 1981, 83.

22. J. F. McKay, P. J. Amend, T. E. Cogswell, P. M. Harnsberg, R. B. Erickson and D. R. Latham in "Analytical Chemistry of Liquid Fuel Sources", Am. Chem. Soc., Adv. in Chem. Series No. 170, 1978, 128.

23. H. H. Oelert, Z. Anal. Chem., 1969, 244, 91.

Table 1: Fraction yields from the ion-exchange chromatography of Arabian heavy crude oil vacuum (950°F+) residuum

Fraction	Yield	Functionality type
Bases	29.6	Quinoline nitrogen
Acids	3.2	Carboxylic acids and phenols
Neutral polar	19.4	Carbazole nitrogen
Neutral nonpolar	46.5	Saturate and aromatic hydrocarbons

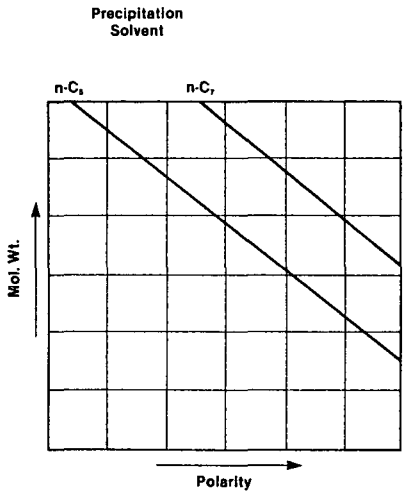

Figure 2: Schematic representation of asphaltene character

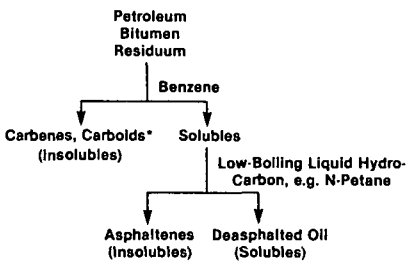

Figure 1: Schematic representation of asphaltene separation.

*In the case of coal liquids, these "insolubles" are often referred to as "preasphaltenes", "asphaltole", etc. based on solubility in solvents such as pyridine and/or quinoline (12,13).

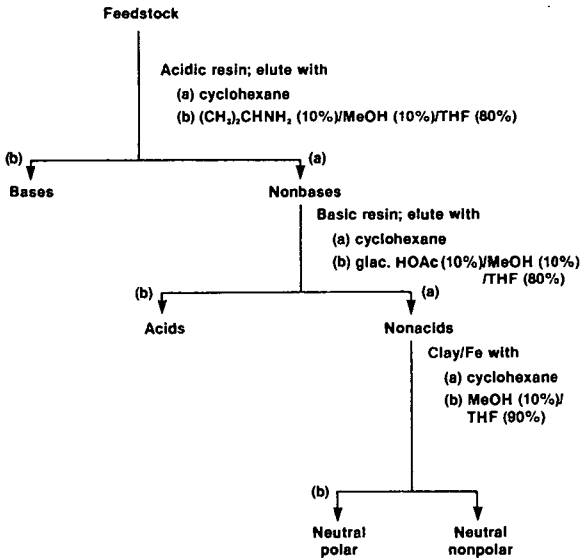

Figure 3: Schematic representation of the ion-exchange fractionation technique.

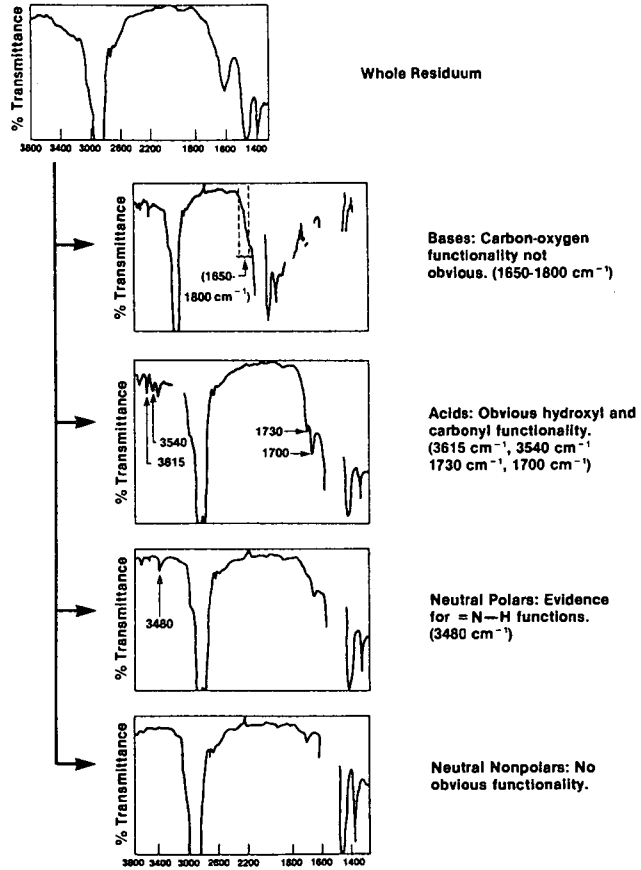

Figure 4: Infrared spectra of fractions separated by the ion-exchange technique

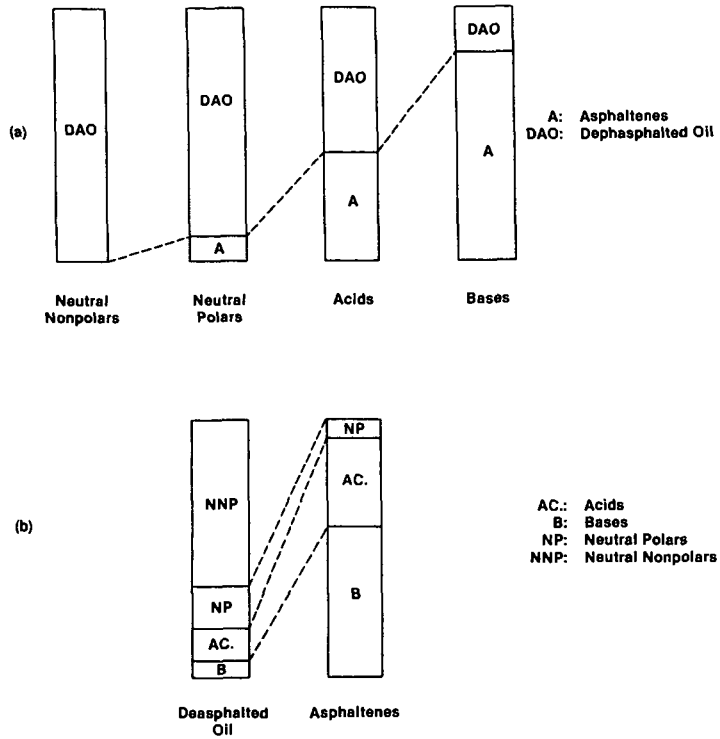

Figure 5: Schematic representation of (a) deasphalting the functionality fractions end (b) reconstruction of the deasphalted oil and asphaltenes on the bases of functional types.

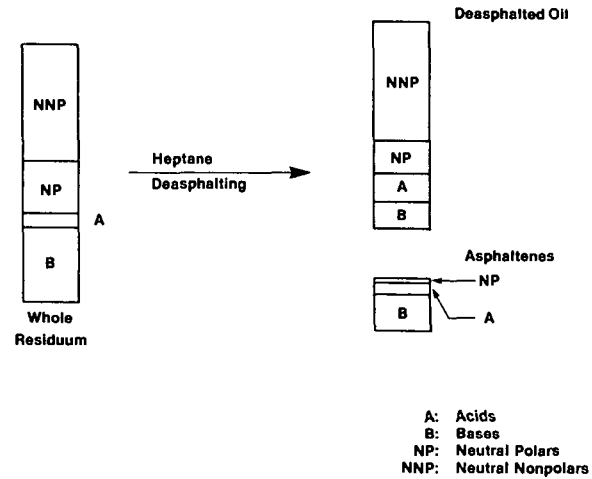

Figure 6: Schematic representation of the deasphalting technique in terms of functionality distribution/redistribution

APPLICATIONS OF X-RAY COMPUTED TOMOGRAPHY TO COAL STUDIES

D.H. Maylotte, P.G. Kosky, E.J. Lamby, C.L. Spiro

General Electric Corporate Research and Development
Schenectady, NY 12301

and

A. Davis, D.F. Bensley

Pennsylvania State University
University Park, PA 16802

X-ray computed tomography (CT) is a non-destructive, non-invasive technique which has been applied here to studies of the internal structures of coal and the penetration of tracer gas into those structures. The CT images are 2-D cross-sectional images of the coal rather than the shadowgraphs of traditional radiography. Compared to shadowgraphs, the CT images provide higher spatial and higher density resolution.

CT images are digital images of the effective x-ray attenuation coefficient for elementary volumes (voxels) within the sample. In these experiments a GE 8800 CT/T machine was used to take the image data, which were then reconstructed to product images with a voxel size of 0.3 mm x 0.3 mm x 1.5 mm. The CT number for each voxel is related to the experimental effective attenuation coefficient for that volume by the relationship:

$$\text{CT No.} = 1024 \times \left[1 + \frac{\mu\,(\text{material})_E - \mu\,(\text{water})_E}{\mu(\text{water})_{Eo}} \right]$$

where $\mu\,(\text{material})_E$ is the attenuation coefficient for the unknown material, $\mu\,(\text{water})_E$ is the attenuation coefficient of water taken under the same conditions, and $\mu(\text{water})_{Eo}$ is the attenuation coefficient of water taken under standard conditions. The CT images were displayed by assigning a grey scale to the CT numbers. The whiter the image the higher the CT number represented by it and the higher the electric density of the sectioned object. The data collection time for each image was nine seconds.

The x-ray tube for this work was operated at 120 Kev. The filtered emission is a continuum covering the range 20 Kev - 120 Kev, peaking at 35 Kev (Ref. 1). Over this energy range the three significant attenuation mechanisms are, (i) photoelectric absorption, (ii) Compton scattering, and (iii) coherent scattering. For carbonaceous materials the dominant mechanism in this energy range is Compton scattering; therefore, the CT images reflect the electron density distribution within the sample. For the low atomic number elements commonly found in coal the atomic weight is almost twice the atomic number (hydrogen contributes little to the total electron density) and therefore the images are approximately images of the mass density within the sample.

Figure 1 shows a CT image of a piece of Illinois #6 coal. The piece was cut from a larger block which, after mining, had been stored in a sealed vessel under deionized water. The dimensions of the piece were 2.5 cm x 2.5 cm x 10 cm long. The long axis was cut parallel to the bedding planes of the coal. This CT image was taken perpendicular to the

long axis of the coal piece. The coal was potted in a cylinder of epoxy which was then cut to expose the two smaller end faces of the coal and finally O-ring sealed in an acrylic plastic tube (5 cm I.D.).

A sample rectangle on the coal image has been displayed in Figure 1a, and a histogram of the CT values within that rectangle is shown in Figure 1b. Both the average and most probable CT number in the area was 1220. Subsequent to the CT experiments, this particular piece of coal has been sectioned along the plane whose structure was examined by the x-ray fan beam. A microlithotype examination of the exposed face showed that the predominant material in the region covered by the sample rectangle is vitrain. A number of bituminous coals have been examined by CT and, after sectioning, petrographically. CT numbers in the range 1210-1250 are the most commonly occurring numbers in these coals. This assignment of a CT number of circa 1210 to vitrain is also justified on theoretical grounds.

The CT number for a particular material can be calculated when the following system characteristics are known, (a) the emission spectra for the filtered source, (b) the elemental composition and number density of the material being examined, (c) the wavelength sensitivity and efficiency of the detection system. The results of such a calculation for a number of standard materials, minerals and for coal are given in Table 1.

Material	CT (Calc.)	CT (Obs.)
Coal ($C_{49}H_{43}O_7S_1N_1$)	1254	~ 1220
Kaolin ($Al_4Si_4O_{10}(OH)_8$)	3096	3078
Teflon C_2F_4	2106	2050
Calcite $CaCO_3$	4521	> 4096
Dolomite $CaMg(CO_3)_2$	3924	3900-4096
Water H_2O (standard)	1024	

TABLE 1: Calculated and Actual CT Numbers for Coal and Minerals

The calculation of the theoretical CT value for coal assumed the formula given in Table 1 and a density of 1.3 $g.cm^{-3}$. The calculated CT number is not significantly affected by the formula chosen to represent coal within the reasonable limits of the formulas for the three major maceral groups, i.e., vitrinite, exinite, and inertinite (2). However, the CT number is directly affected by the density chosen for the coal. This insensitivity of CT number to the formula of a hydrocarbonaceous material and its sensitivity to the density is demonstrated in Figure 2. In the density range around 1.3 g/cc the density sensitivity of the technique is 11 CT numbers for a 1% density change. For a uniform material the standard derivation of the CT numbers is $\pm$ 2. The different maceral groups in coal have different densities in the range 1.1 to 1.6 g/cm^3 (2), and the CT image has enough density resolution to distinguish between them. However, the normal size range of many individual coal macerals is below the spatial resolution of the CT equipment being used in this work. In the present experiments, a CT voxel represents a volumetric average of the densities of the macerals contained within it.

In the case of kaolin the CT number for the bulk sample reflects the porosity of the kaolin as well as the CT number attributable to the mineral itself. The kaolin sample was therefore potted in a low viscosity epoxy resin which penetrated the outer layers of the sample (Figure 3). The CT number for the kaolin mineral and the void fraction within the kaolin can then be calculated from the relationships:

$$CT_{total}(1) = \varepsilon \times CT_{epoxy} + (1-\varepsilon)\, CT_{kaolin} \qquad 1)$$

$$CT_{total}(2) = \varepsilon \times (CT \text{ \# of air} = 0) + (1-\varepsilon)\, CT_{kaolin} \qquad 2)$$

where ε is the void fraction in the mineral. The Equation 1) was evaluated for a region where epoxy had penetrated the kaolin and Equation 2) was evaluated for a region inside the kaolin where the epoxy has not penetrated and air fills the spaces between the kaolin grains. The CT number for the cured epoxy was taken from the region outside of the mineral. The CT number for kaolin as obtained in this calculation is given in Table 1 and the void fraction in the bulk mineral was found to be 38%.

The results of Table 1 show that if a region of coal has a CT number above 1300 but less than 3100 then it is contaminated with a varying proportion of mineral matter, and if the CT number is greater than 3100 then it is contaminated with high atomic number minerals (e.g., calcite or pyrite). If the CT number is between 1100 and 1400 then the area is essentially organic, while if it is below 1000 then the area contains an unusally large component of voids.

The CT number for a particular volume of the imaging space is affected by the amount and density of the coal present, the minerals present, and the void space in that volume. Because of the large CT numbers associated with the mineral matter (Table 2), the mineral content of the CT volume would be expected to have a large effect upon the CT image.

Figure 4 shows the same CT image as in Figure 1a, but this time a reference line has been drawn over the image and the CT numbers plotted along that line. The white area at the bottom left of the image corresponds to the peak in CT number on the left-hand side of the graph.

After the CT experiments had been completed, and the coal sectioned along the CT image plane, automated x-ray microprobe measurements were made along the same region as the line in the CT image. The area of the microprobe beam was 50 μm x 50 μm with an expected penetration of ca 1 μm. The elements scanned in the microprobe were Si, Al, S, Fe, Mg, Na, K, Ca. The observed weight percents for the elements were totalled and plotted against distance (Figure 5). The automated microprobe measurements are in a finer grid than the CT data. If converted to the same grid size as the CT, then peaks in the microprobe spectra would appear shorter and broader. There does appear to be a first order correlation between the mineral matter in the coal and the variation in density of the CT image. CT images of raw coal can be regarded therefore as maps of the mineral distribution within the coal. A further distinction into minerals of elements with high atomic number (e.g., pyrite) and minerals with only low atomic number minerals (e.g., illite) may also be possible using images taken with different x-ray energies.

The porosity within this particular coal sample was examined by following the penetration of xenon gas into the sample at room temperature (27°C). Xenon was chosen because of its relatively inert nature and becase it has a strong x-ray K-absorption edge at 35 Kev, i.e., at the peak of the spectrum from the x-ray tube. The presence of xenon should therefore be detectable against the coal background. The penetration of xenon gas

into the coal was carried out by exposing one end face of the coal parallelepiped to a pressure of xenon (1130 torr) and monitoring the gas exiting the opposite face by following the pressure rise in a closed system of known volume. The penetration of gas within the coal was monitored, (a) with the coal containing its equilibrium moisture, (b) after the coal had been dried at 80°C for two weeks. The bulk gas flow through the coal was much faster in case (b) than in (a). After about 3.5 hours the pressure on both sides of the coal had equalized in case (b). Images from the second series of experiments are more indicative of the porosity within the coal and three images from these experiments are shown in Figure 6. These images were obtained by subtracting the digital image of the evacuated coal from the digital images taken while the xenon was penetrating into the coal. The resulting difference image is a map of xenon penetration. The images clearly show the non-uniform nature of the penetration of the xenon into the coal. The lighter areas in the image are the areas into which the xenon has preferentially penetrated. The plane of the CT image was situated about 15 mm in the coal block from the high pressure end. The presence of xenon in this plane was detected in the first image taken of this plane after the xenon had been introduced into the high pressure chamber (time elapsed was eight minutes). The major features of the pattern were streaks of xenon parallel to the bedding planes of the coal. Over the duration of the experiment these features grew in intensity and broadened out. This behavior suggested that the xenon penetrated into this plane by a network of fine cracks. The cracks that are interconnected and give access to the xenon reservoir appear to be primarily oriented parallel to the bedding planes of this piece of coal and many are associated with the mineral-rich regions of the coal. In these cracks, the xenon pressure rapidly reached the reservoir pressure, but because the cracks are very fine on the scale of the CT resolution, the actual amount of xenon introduced into a voxel even when the crack had reached reservoir pressure was still quite small and so the CT signal in the difference image was small. As the xenon diffused into the coal away from the crack more xenon was introduced into the voxel containing the crack, and into neighboring voxels and consequently, the numbers on the difference image increas ed.

Figure 7 shows a composite plot of the CT numbers along the line drawn on the difference images of Figure 6. For the data along each line, the curve has been normalized to its maximum value. The plot illustrates the spreading of the xenon into the neighboring coal from a source apparently situated ca 2.5 mm from the arbitrary origin. It may be possible to analyze these curves in terms of a diffusion parameter which depends upon the CT number of the original coal.

A calibration graph of CT number against xenon pressure is given in Figure 8. This shows that if the xenon pressure at the high pressure inlet was 1130 torr, then the maximum observable CT number increase within an image of the coal should be 263, provided that all the xenon remained in the gas phase within the coal. In fact, CT numbers much greater than the gas phase maximum are observed within the CT difference image (Figure 6). This is probably caused by the xenon being present within the coal both as a gas phase species and as adsorbed species.

In the final image used in Figure 6, the maximum CT value along the line had risen to 2171, or over eight times the maximum possible from solely gas phase absorption. On the assumptions that the occupied surface area for a xenon atom is 22 $(Å)^2$ (3) and a coal material density of 1.3 g/cm^3, then the apparent surface area in a region with a xenon difference CT number of 2171 is 51 m^2/g. Using a BET apparatus, a room temperature xenon absorption measurement on a micronized sample of coal from the same batch gave a surface area of 44 m^2/g. The final image of xenon penetration into the coal could therefore be regarded as a surface area image for the coal. This information should be useful in future studies on the reactivity of coal.

The primary interest in the CT technique is in making use of its non-invasive nature for in situ studies of coal combustion and gasification. The preliminary studies discussed here will provide a basis for understanding the images obtained from more complex experiments.

ACKNOWLEDGMENTS

We would like to express our appreciation to the U.S. Department of Energy for support of this work (Contract No. DE-AC21-82MC19210).

REFERENCES

1. Maylotte, D.H., Lamby, E.J., Kosky, P.G., St. Peters, R.L., "Proceedings fo the International Conference on Coal Science", Dusseldorf, 1981.

2. Stach, E., Mackowsky, M.-th., Teichmuller, M., Teichmuller, R., Taylor, G.H., Chandra, D., (Eds.), Coal Petrology, Gerbruder Borntraeger, Berlin, 1975.

3. McClellan, A.L., Harnsberger, H.L., "Cross-Sectional Areas of Molecules Adsorbed in Solid Surfaces", Coll and Interface Sci., 23, 577 (1967).

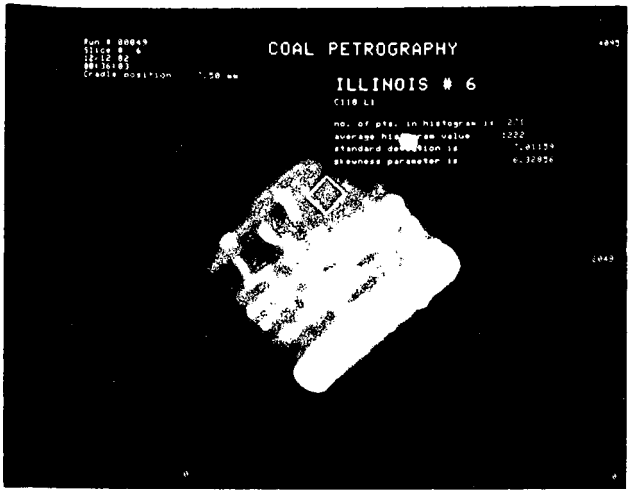

Figure 1a. CT Image of Encapsulated Illinois #6 Coal

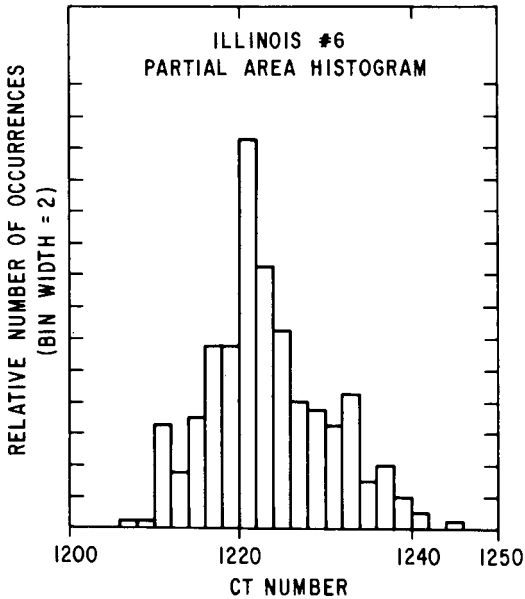

Figure 1b. Histogram of CT Values Within the Rectangular Outline of Figure 1a

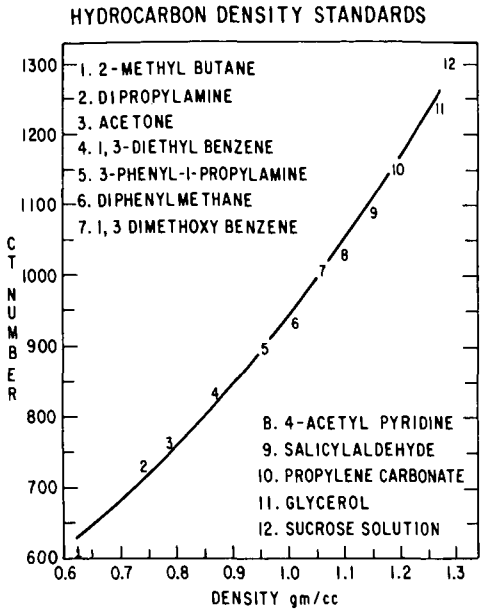

Figure 2. CT Number as a Function of Hydrocarbon Density

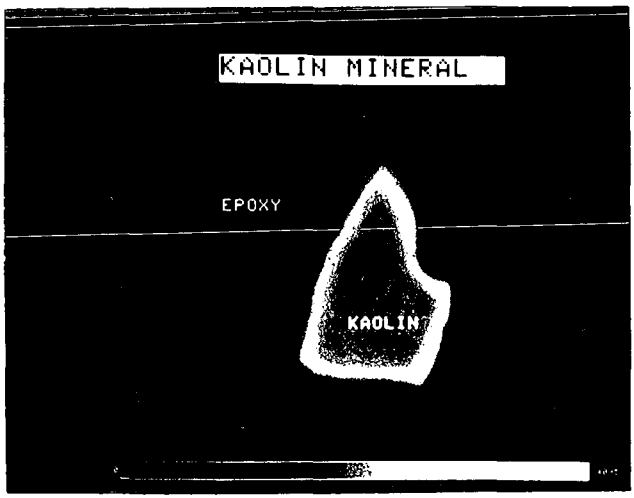

Figure 3. CT Image of Kaolin Sample Impregnated With Epoxy Around the Periphery

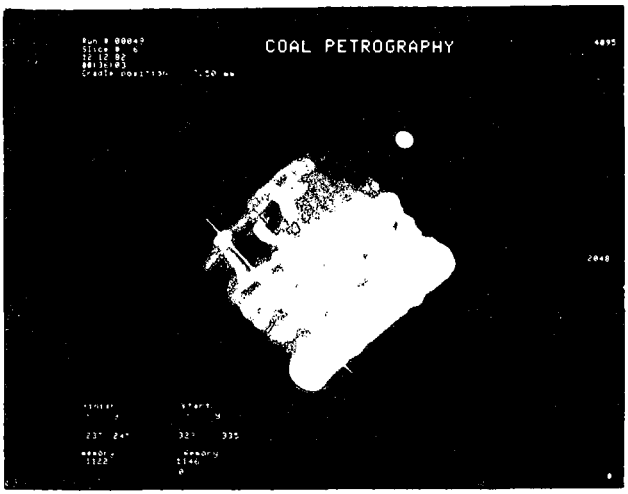

Figure 4a. CT Image of Illinois #6 Coal With a Line Drawn on the Image

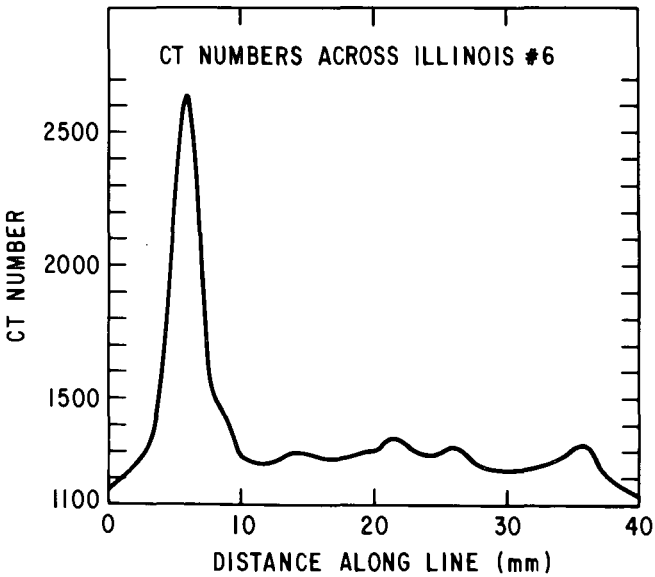

Figure 4b. CT Numbers Along the Line Drawn in Figure 4a

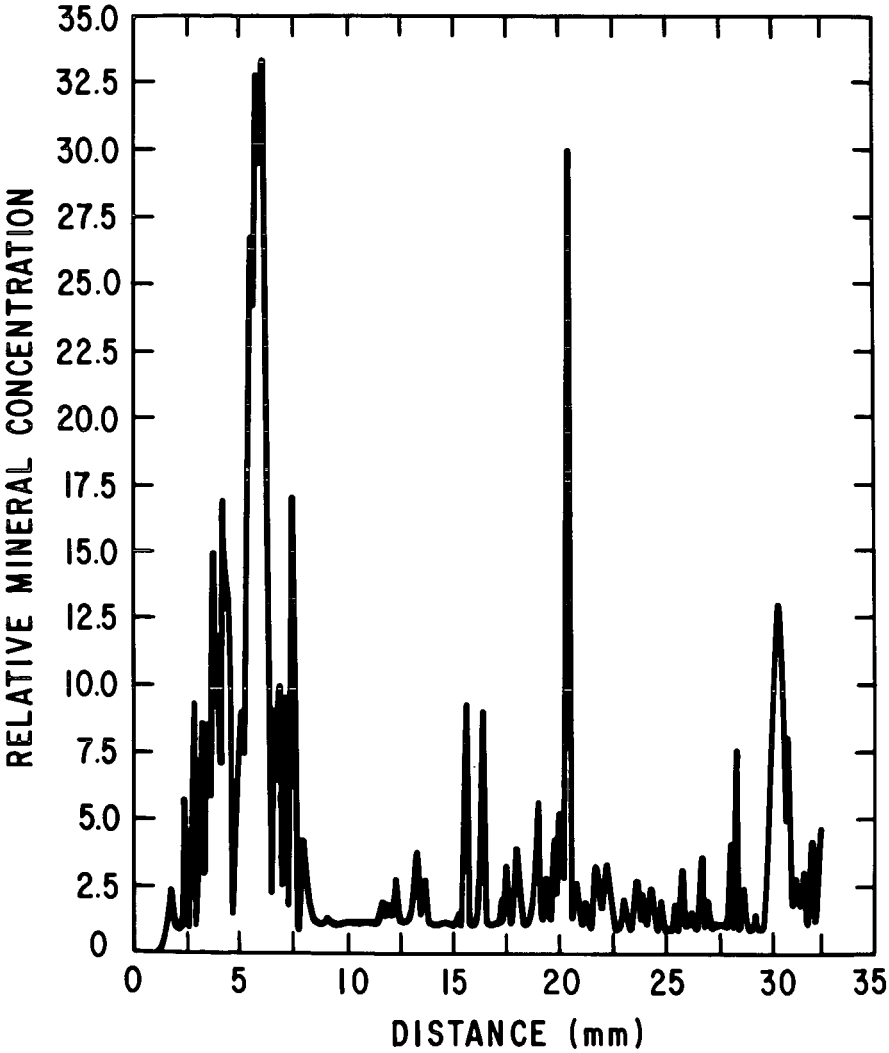

Figure 5. Relative Mineral Concentration Along the Line of Figure 4a.

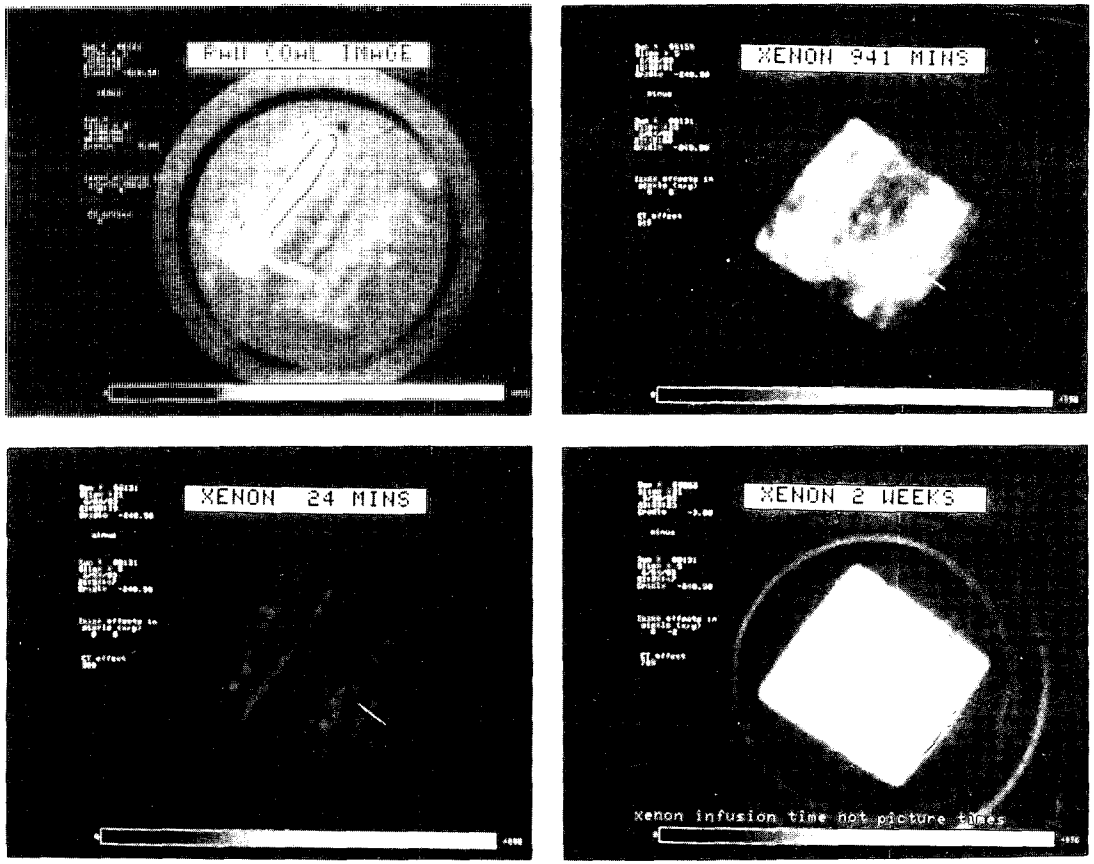

Figure 6. Xenon Penetration into Illinois #6

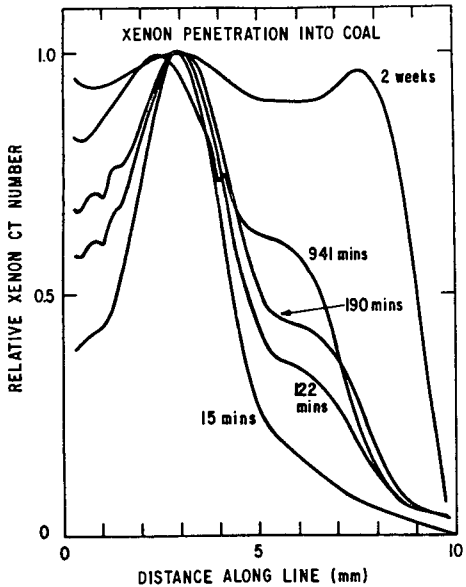

FIGURE 7. XENON PENETRATION INTO COAL ALONG THE LINE DRAWN IN FIGURE 6

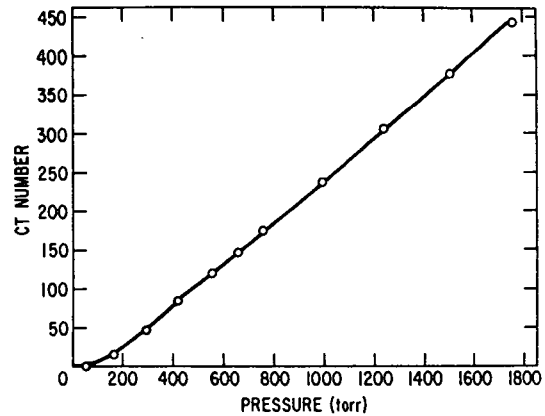

FIGURE 8. CT NUMBER AS A FUNCTION OF XENON GAS PRESSURE

EFFECTS OF COAL PREOXIDATION AND HEAT TREATMENT CONDITIONS ON RESULTING CHAR STRUCTURE OF CAKING COAL

D. J. Maloney* and R. G. Jenkins

Department of Materials Science and Engineering
The Pennsylvania State University, University Park, Pennsylvania, 16802

Introduction

When most bituminous coals are heated in the absence of air, they soften (i.e., become fluid), agglomerate, and, as gases and vapors are evolved, swell to form a coke. These properties can limit the utilization potential of certain coals because agglomerates can impede gas flow leading to poor mixing in reactors and, in the extreme case, eventual plugging. In addition, coals which pass through a plastic stage produce relatively unreactive chars (1,2). These factors can add substantially to the cost of a gasification process.

Coal agglomerating tendencies can be eliminated by mild oxidation of the raw coal prior to heat treatment. This method is very effective in removing the swelling and softening characteristics of caking coals (3). Also, under certain carbonization conditions, preoxidation can significantly enhance the subsequent reactivity of the resulting chars (2).

Recent studies at the Pennsylvania State University have been directed at understanding the effects of preoxidation on coal utilization potential under conditions of interest for entrained-flow gasification and pulverized coal combustion (rapid heating rate, short residence time). Studies were conducted on an eastern bituminous coal in an effort to evaluate the effects of preoxidation on devolatilization behavior (yield and kinetics), coal swelling and agglomerating tendencies, and resulting char structure and reactivity (4). This paper describes the changes in char structural features resulting from coal preoxidation and examines the relationship between char structure and subsequent gasification potential.

Experimental

The chars examined in this study were prepared from freshly mined and preoxidized samples of a strongly caking bituminous coal under widely varying pyrolysis conditions (heating rate and time). The parent sample was PSOC-1099, a HVA bituminous coal from the Pittsburgh No. 8 seam. All work described here was conducted on 200 x 270 mesh size fractions with mean particle diameters of 62 μm. Preoxidized coal samples were prepared by air oxidation of sized coal in a fluidized-bed furnace. Oxidation temperature, time, and weight gain were determined based upon complementary thermogravimetric studies of the air oxidation of each coal. Oxidation levels reported here are given as percent weight gain on oxidation (dry coal basis). The proximate analyses of the fresh and preoxidized coals used in this work are presented in Table 1.

Chars were prepared under rapid heating conditions (~ 10^4 K/s) in an entrained-flow furnace at temperatures between 1073 and 1273K with residence times up to 0.27s. Slow pyrolysis (12 K/min) chars were prepared in a horizontal tube furnace at a temperature of 1273K with a soak time at final temperature of 1 h. Extensive analyses of the surface properties of the chars were performed. Char morphology was examined

---

* Present Address: U.S. DOE, Morgantown Energy Technology Center, P.O. Box 880, Collins Ferry Road, Morgantown, West Virginia, 26505.

TABLE 1

Proximate Analyses of Samples* Examined

Sample	Moisture Percent	Ash Percent	Volatile Matter Percent	Fixed Carbon Percent
PSOC-1099 (HVA bituminous coal)	1.3	10.6	34.0	54.1
PSOC-1099 (1 percent O_2 added)	0.8	10.6	32.5	56.1
PSOC-1099 (2 percent O_2 added)	1.0	10.5	31.6	56.9

* Proximate analyses were conducted on 200 x 270 mesh fractions of 62 μm mean particle diameter.

using SEM. Total surface area was determined by CO_2 physisorption at 298K. Macro and transitional pore surface areas were determined by N_2 adsorption at 77K. Additional char structural information was obtained by ultimate analysis using a Perkin-Elmer Model 240 elemental analyzer. Char reactivities were determined in air at 668K using a thermogravimetric method described by Mahajan and co-workers (2,5). Complete details of all experimental procedures employed in this study are supplied in Reference 4.

Results

Figures 1 and 2 are scanning electron micrographs of chars prepared from fresh and preoxidized samples (2.5 percent oxygen added) of PSOC-1099 after heat treatment of 0.23 s at 1273K. Chars prepared from the fresh HVA coal, Figure 1, were thin-walled transparent structures commonly referred to as cenospheres (6-8), the mean diameters of which were more than twice that of the starting coal. This represents a ~10-fold increase in volume. During pyrolysis the sample shown lost 51 percent of its starting material (daf). Under the conditions employed in this work, cenospheres were fully developed during the first 0.1 s of heating time after which no observable changes in macroscopic properties were evident. When carbonized under slow heating conditions, this coal formed a fused swollen coke.

As illustrated in Figure 2, the preoxidized coal did not form the cenosphere structures observed in Figure 1. Preoxidized coal char particle sizes were similar with those observed for the parent sample prior to carbonization. Char particle shapes, however, were altered considerably. Particle surfaces were rounded with little evidence of the sharp, well-defined fracture surface characteristic of the starting coal. This indicates that the preoxidized coal passed through a fluid state during rapid heating. All preoxidized samples examined in the present study formed chars of similar size and shape during rapid pyrolysis. In contrast to this behavior, the preoxidized coal exhibited no signs of thermoplastic behavior when carbonized under slow heating conditions.

Figure 3 illustrates the development of char surface area (CO_2 area) as a function of heat treatment time at temperatures of 1073 and 1173K for chars produced from the fresh HVA coal. Char surface areas remained constant during the first 0.05 s of heat treatment after which surface areas increased with time. The CO_2 surface area for the parent coal was 170 m^2/g. At each heat treatment temperature, a more than two-fold increase in surface area occurred during the pyrolysis process. At 1073K, the maximum char surface area obtained was 360 m^2/g (daf char); while at 1173K, the maximum char surface area was 465 m^2/g. The sigmoid-shaped curves shown in Figure 3 suggest that char surface areas were approaching maximum values. This observation is supported by the results of Radovic (9) and others (10-14).

The N_2 surface area determined for the fresh coal was 2.7 m^2/g. N_2 surface areas determined for the corresponding char samples were less than 2 m^2/g for all the chars examined. These areas approximate the theoretical limits calculated for cenospheres of the size and weight produced in this study.

Generally, N_2 surface areas determined for coals or char samples are considerably lower than the corresponding CO_2 surface areas. N_2 adsorption kinetics (at 77K) on microporous materials are limited by activated diffusion and, therefore, N_2 adsorption gives an estimate of macro and meso porosity (15). CO_2 (at 298K), however, is accessible to surfaces present in macro, meso, and micro pores.

Figure 4 illustrates the development of char surface area as a function of weight loss during pyrolysis. Surface areas exhibited little change during the early stages of pyrolysis. After 25 percent weight loss, however, char areas increased rapidly up to a weight loss of approximately 45 percent. Subsequent weight loss, up to 50 percent, had little effect on resulting surface areas. It is of interest to note that the weight loss level at which surface areas began to increase coincided roughly with the initiation of cenosphere growth (4).

CO_2 surface areas determined for the untreated and preoxidized coal samples and selected chars generated from these samples are presented in Table 2.

TABLE 2

Comparison of CO_2 Surface Areas
Determined for Fresh and Preoxidized
Coals and Their Corresponding Chars

		Surface Areas m^2/g (daf basis)			
Carbonization Temperature (K)	Raw	1073	1173	1273	1273
Carbonization Time (s)	Coal	0.27	0.25	0.23	3600*
Sample					
PSOC-1099 (untreated)	170	360	465	465	88
1.2 percent oxygen added	160	290	480	475	
2.5 percent oxygen added	150	320	500	522	188

* Slow heating conditions (12 K/min) followed by 1 h soak time at 1273K.

Preoxidation had little effect on the surface area of the coal sample prior to carbonization. During pyrolysis, preoxidation had a mild effect on resulting char surface area, however, no specific pattern was evident. After heat treatment at 1073K, surface areas of chars prepared from preoxidized coals were less than that observed for the corresponding unoxidized coal char. At carbonization temperatures of 1173 and 1273K, preoxidized coal formed chars with slightly higher surface areas than the corresponding chars prepared from the unoxidized coal. When slow heating conditions and extended heat treatment times were employed, preoxidation led to a significant increase in resulting char surface area. Following extended hold times at elevated temperatures, char surfaces areas were greatly reduced when compared with char surfaces areas observed for the rapidly heated (short time) samples.

The carbon and hydrogen percentages obtained from ultimate analysis provide some useful information concerning changes in char composition as a function of carbonization

conditions. The C/H ratios presented in Figures 5 and 6 show that as carbonization temperatures and times were increased, hydrogen was preferentially removed from the char samples. As the temperature of carbonization was increased, the rate of hydrogen evolution relative to carbon evolution increased significantly. The preoxidized coal behavior was similar to that of the fresh coal. Under comparable carbonization conditions, no significant differences were observed in the C/H ratios determined for chars derived from the fresh and preoxidized coal samples.

Preoxidation effects on char composition are illustrated more clearly in Figure 7. Over 80 percent of the hydrogen present in the fresh HVA coal sample was removed during 0.23 s of heat treatment at 1273K. Less than 50 percent of the original carbon was removed in the same time interval. Preoxidation reduced the quantities of both hydrogen and carbon liberated during comparable heat treatments.

The relative gasification potential of the chars produced in this study were evaluated by examining the reactivities of selected samples during gasification in one atmosphere of air (20 kPa O_2). The reactivity parameter reported here is $\tau 0.5$, which, at a given reaction temperature, is the time corresponding to a fractional burn-off of one-half. Mahajan, Yarzab, and Walker (5) demonstrated the utility of this parameter for correlating char reactivity data for gasification in air, steam, and CO_2.

Table 3 shows the reactivity parameters, $\tau 0.5$, determined for chars generated from PSOC-1099 as a function of carbonization temperature and preoxidation level. The carbonization times employed were the maximum residence times attainable at each furnace operating temperature. These were 0.27 s at 1073K, 0.25 s at 1173K, and 0.23 s at 1273K. The reactivity parameters reported are the mean values determined from three replicate reactivity tests. Typically the standard deviation from the mean was less than ± 10 percent.

TABLE 3

Comparison of Air Reactivities at 668K for Chars Prepared from PSOC-1099 as a Function of Carbonization Temperature and Preoxidation Level

Furnace Temperature (K)	Reactivity Parameter $\tau 0.5$ min		
	No Oxygen Added	1.2% Oxygen Added	2.5% Oxygen Added
1073	33	32	36
1173	46	46	46
1273	69	64	66

As carbonization temperature was increased from 1073K to 1273K, the subsequent char reactivity decreased by a factor of two. This was true for chars prepared from both the unoxidized and preoxidized parent samples. Preoxidation had no apparent effect on subsequent char reactivity. Values of $\tau 0.5$ determined for chars prepared from unoxidized and preoxidized coals were equivalent within the limits of reproducibility of the reactivity measurement.

Discussion

Nsakala and co-workers (16,17) and Radovic (9, 18) examined lignite coal chars generated under rapid heating, short residence time conditions. Each of these investigators reported increases in char surface areas, determined by CO_2 adsorption, of 200 to 300 m^2/g. The results presented here concur with these findings. Nsakala, et al. (16, 17), also reported significant increases in N_2 surface area during pyrolysis of a lignite. Similar increases in N_2 area were not observed for the bituminous coal examined in the present study.

Mahajan, et al. (2), reported that surface areas of chars produced from preoxidized coals were several times larger than those prepared from fresh coal samples. These investigators examined coals of similar rank and employed preoxidation conditions comparable with those used in the present study. They employed slow heating conditions (10 K/min) and extended soak times (1 h) at final temperature (1273K) during the carbonization process. When slow heating conditions (12 K/min to 1273K, followed by 1 h soak time at 1273K) were employed in the present study, chars produced from the unoxidized coal had CO_2 surface areas significantly lower than the chars produced from the preoxidized coal (Table 2). However, under rapid heating conditions, preoxidation had only a slight effect on resulting char surface area. It is apparent from the results shown here that preoxidation effects on resulting char area were greatly diminished when employing rapid heating conditions and short carbonization times.

Decreases in char reactivity with increasing heat treatment temperature were reported previously for coal chars (1,9,18) and other disordered carbonaceous solids (19). Jenkins and co-workers (1) examined chars prepared under slow heating conditions (10 K/min heating rate, 2 h soak time at final temperature). They reported that char reactivities during air gasification decreased by as much as 10 times when carbonization temperature was increased from 873K to 1273K. Radovic (9,18) examined reactivities of chars prepared from a lignite under rapid heating, short contact time carbonization conditions similar to those employed in the present study. He observed a decrease by a factor of 10 when carbonization temperature was increased from 975K to 1275K.

Jenkins, et al. (1), suggested that the effect of temperature on subsequent char reactivity could be explained on the basis of the concentration and accessibility of active sites. Firstly, they observed that the lower temperature chars had a significantly higher level of macro and transitional porosity (estimated from N_2 adsorption) and, thus, a more open or accessible pore structure than did the higher temperature chars. Secondly, they noted that the chemical nature of the char surface changed with changing carbonization temperature. Lower temperature chars had a higher hydrogen content than did the higher temperature chars. They suggested that hydrogen was preferentially removed during air gasification leaving behind nascent carbon active sites which are more reactive to oxygen. The chars generated in this study were essentially void of surface area associates with macro and transitional pores. Char reactivities exhibited no correlation with the micropore areas determined for these chars. Considering these results, it is probable that char reactivities were more strongly influenced by the amount of hydrogen remaining in the char. This suggestion is supported by the elemental composition data presented in Figures 5 through 7.

Mahajan and co-workers (2) observed that under slow heating conditions (10 K/min, 1 h soak at 1273K) preoxidation markedly enhanced subsequent char reactivity (by a factor of up to 40). The results of this study suggest that preoxidation effects on resulting char surface area and reactivity are greatly diminished when rapid heating conditions and short carbonization times are employed. In support of this observation, selected coal and char samples were carbonized under conditions comparable with those used by Mahajan and co-workers (2). Chars were prepared from the fresh HVA coal and

preoxidized (2.5 percent oxygen added) coal. In addition, the 1273K chars (0.23 s carbonization time) prepared by rapid heating of these samples were recarbonized under slow heating conditions. The reactivity parameters determined for these chars are presented in Table 4. Increasing hold times at the final carbonization temperature (1273K) from 0.23 s to 3600 s led to a seven-fold decrease in reactivity for the chars prepared from the unoxidized coal. When comparable hold times were employed, heating rate had little effect on subsequent char reactivity. Chars prepared from preoxidized coals were about a factor of two more reactive than the corresponding chars prepared from the unoxidized coal. The important factor in determining the subsequent char reactivity was the hold time at final temperature and not the heating rate.

TABLE 4

Effect of Carbonization Conditions on Subsequent Reactivity of Chars Prepared from Raw and Preoxidized Samples of PSOC-1099

Char Preparation Method	Heating rate	Reactivity Parameter $\tau_{0.5}$ min		
		30,000 K/s	0.2 K/s	30,000 K/s*
	Hold Time at 1273K	0.23 s	3600 s	3600 s
Parent Sample				
Raw (unoxidized)		69	450	490
2.5 percent oxygen added		66	300	260

* Chars were prepared in the entrained-flow furnace under rapid heating conditions and were recarbonized by heating at 0.2 K/s and holding for 3600 s at 1273K.

Mahajan and co-workers (2) attributed the enhancement of char reactivity as a result of preoxidation to the large increases in micropore surface areas they observed for these chars. Under rapid heating, short contact time, carbonization conditions similar increases in surface area and char reactivity were not observed. However, when carbonization times were extended, preoxidation effects became evident. These results provide some insight concerning the role which oxygen plays in the carbonization process. From the work of Jenkins, et al. (1), and others (10-14), it is known that increasing the severity (time, temperature) of carbonization conditions results in a sealing up or closing of char porosity. This annealing process reduces the accessibility and quantity of active gasification sites present in the char. The results of this study and the work of Mahajan, et al. (2), suggest that preoxidation inhibits the annealing process and, thereby, leads to the production of more reactive coal chars. This inhibition does not become manifest in the initial stages of the carbonization process.

Acknowledgments

Funding for this work was provided by the Cooperative Program in Coal Research at the Pennsylvania State University and by the U.S. Department of Energy under Contract No. DE-AC01-79ET14882. Additional support was supplied by a Mining and Mineral and Mineral Fuels Conservation Fellowship. Elemental analyses were generously supplied by the United Technologies Research Center under the direction of Dr. James D. Friehaut.

References

1. Jenkins, R. G., S. P. Nandi, and P. L. Walker, Jr., Fuel, 52, 288, 1973.
2. Mahajan, O. P., M. Komatsu, and P. L. Walker, Jr., Fuel, 59, 3, 1980.
3. Maloney, D. J., R. G. Jenkins, and P. L. Walker, Jr., Fuel, 61, 175, 1982.
4. Maloney, D. J., Ph.D. Thesis, The Pennsylvania State University, 1983.
5. Mahajan, O. P., R. Yarzab, and P. L. Walker, Jr., Fuel, 57, 643, 1978.
6. Newall, H. E., and F. S. Sinnatt, Fuel, 3, 424, 1924.
7. Newall, H. E., and F. S. Sinnatt, Fuel, 5, 335, 1926.
8. Newall, H. E., and F. S. Sinnatt, Fuel, 6, 118, 1927.
9. Radovic, L. R., Ph.D. Thesis, The Pennsylvania State University, 1982.
10. Chiche, P., S. Durif, and S. Pregermain, Fuel, 44, 5, 1965.
11. Miura, S., and P. L. Silveston, Carbon, 18, 93, 1980.
12. Razouk, R. I., F. Z. Saleeb, and A. M. Youssef, Carbon, 6, 325, 1968.
13. Toda, Y., Fuel, 52, 94, 1973.
14. Toda, Y., Fuel, 52, 99, 1973.
15. Walker, P. L., Jr., Phil. Trans. R. Soc. Lond., A300, 65,1981.
16. Nsakala, N., R. H. Essenhigh, and P. L. Walker Jr., Fuel, 57, 605, 1978.
17. Nsakala, N., Ph.D. Thesis, The Pennsylvania State University, 1977.
18. Radovic, L. R., P. L. Walker, Jr., and R. G. Jenkins, Fuel, 62, 849, 1983.
19. Blake, J. H., G. R. Bopp, J. F. Jones, M. G. Miller, and W. Tambo, Fuel, 46, 115, 1967.

2:10-4-83:pp:5a

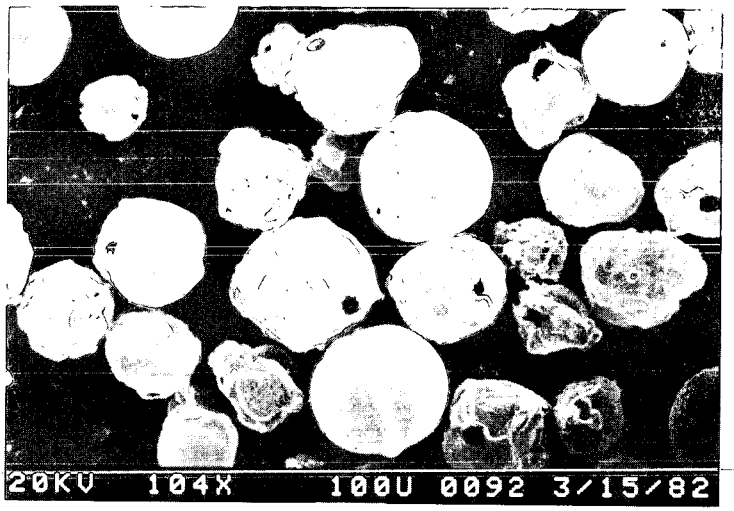

FIGURE 1. SCANNING ELECTRON MICROGRAPH OF THE CHAR PRODUCED FROM PSOC-1099 FOLLOWING HEAT TREATMENT AT 1273 K FOR 0.23 S

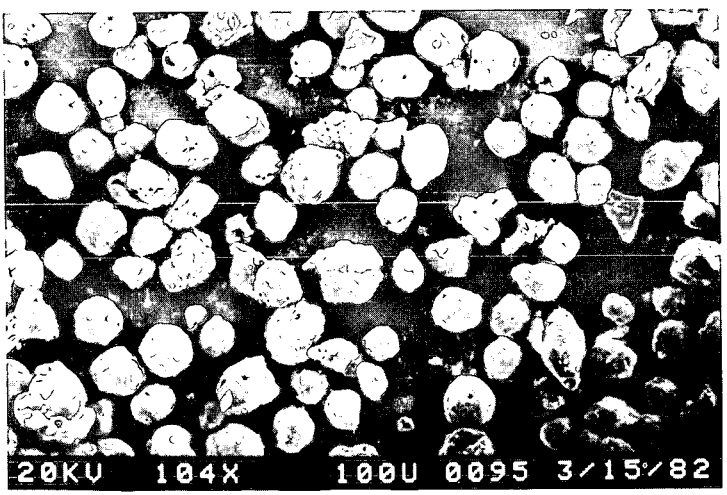

FIGURE 2. SCANNING ELECTRON MICROGRAPH OF THE CHAR PRODUCED FROM PREOXIDIZED PSOC-1099 (2.5% OXYGEN ADDED) FOLLOWING HEAT TREATMENT AT 1273 K FOR 0.23 S

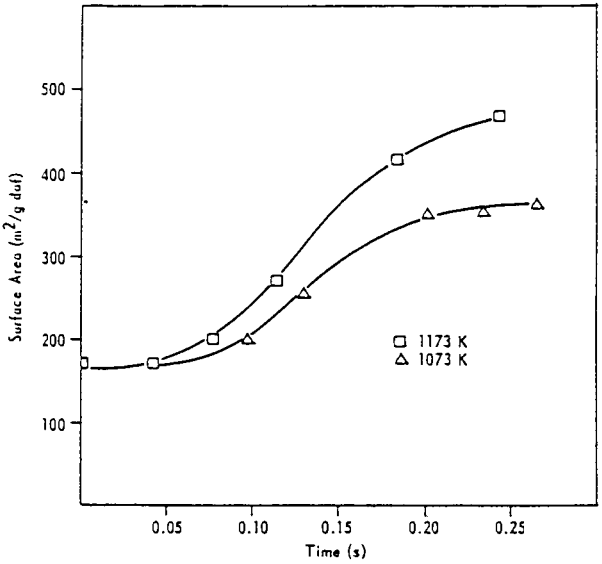

Figure 3. EFFECTS OF CARBONIZATION TIME AND TEMPERATURE ON RESULTING CO_2 SURFACE AREA FOR CHARS PREPARED FROM PSOC-1099

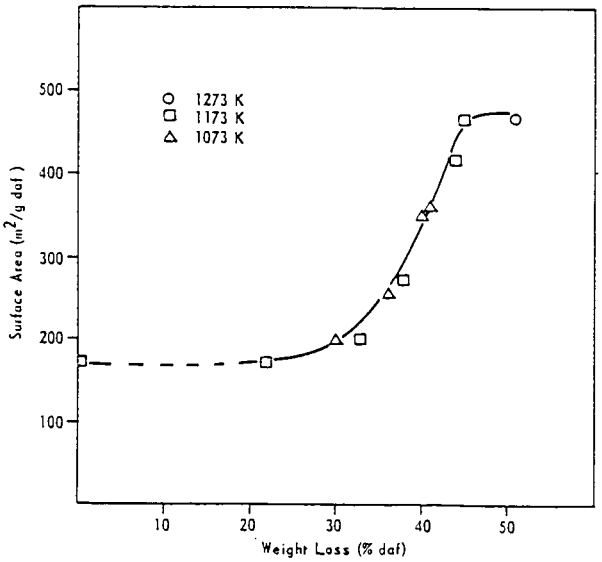

Figure 4. EFFECT OF PYROLYSIS YIELD ON RESULTING CO_2 SURFACE AREA FOR CHARS PREPARED FROM PSOC-1099

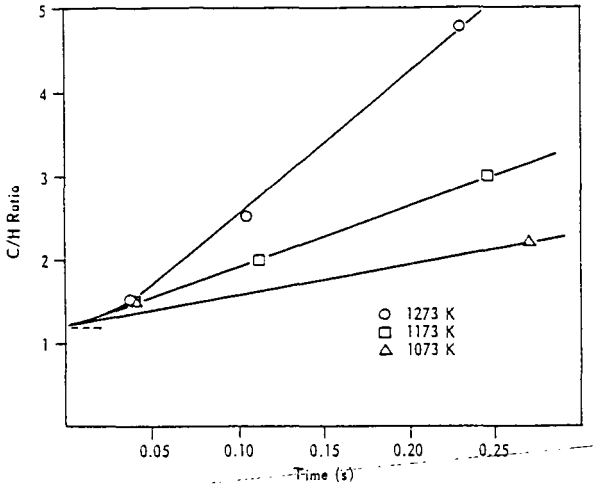

Figure 5. EFFECTS OF CARBONIZATION TIME AND TEMPERATURE ON RESULTING ATOMIC C/H RATIOS FOR CHARS PREPARED FROM PSOC–1099

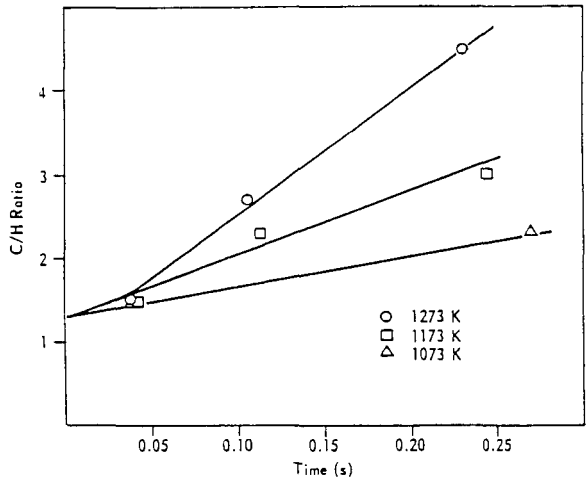

Figure 6. EFFECTS OF CARBONIZATION TIME AND TEMPERATURE ON RESULTING ATOMIC C/H RATIOS FOR CHARS PREPARED FROM PREOXIDIZED PSOC–1099 (2.5% Oxygen Added)

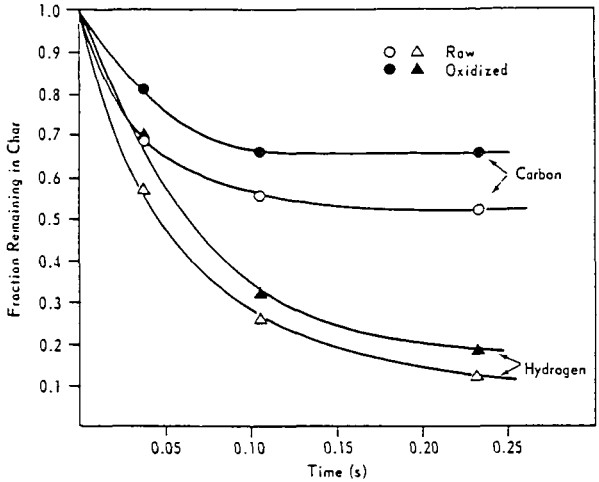

Figure 7. WEIGHT FRACTIONS OF CARBON AND HYDROGEN REMAINING IN CHARS AS A FUNCTION OF TIME AT 1273 K FOR RAW AND PREOXIDIZED (2.5% Oxygen Added) SAMPLES OF PSOC–1099

High Temperature Transformations of Minerals in Coal and the Relationship to the Organic Structure

P.A. Montano and A.S. Bommannavar

Department of Physics, West Virginia University
Morgantown, WV 26506

I. Introduction

The major use of coal is in direct combustion for the generation of electricity. Because of the environmental hazards involved in its use, considerable research has become necessary to fully understand the behavior of the different compounds appearing in coal and the ways in which they transform throughout the course of processing.

Of all the minerals present in coal, iron disulfides (pyrite and marcasite) are the most deleterious. They are one of the major sources of SO_2 pollution. Clay minerals represent a large percentage of the inorganic matter in coal. These minerals are transformed at high-temperature to ferrous and ferric glass phases. Mössbauer spectroscopy can be very helpful in understanding the transformation of iron-bearing minerals during combustion. Such a technique was used to study the oxidation of pyrite[1] at moderate temperatures (maximum 400°C). The oxidation of pyrite in an IL#6 coal occurs in three steps: a) to iron sulfates between 25° to 310°C, b) to γ-Fe_2O_3 between 310° and 325°C, and c) to α-Fe_2O_3 above 325°C.[1,2] It was also observed that the rate of oxidation is strongly particle size dependent. Wendeborn[3] enumerates no less than sixteen concurrent reactions for the oxidation of pyrite. Schwab and Philinis[4] observed that in the range of 400-500°C, the oxidation of pyrite proceeds mainly through the formation of oxides. Sulfate formation amounted to only 12% of the oxide formation at the lower temperature and decreased with increasing temperature. From thermodynamics and kinetics of the reaction of sulfur in coal, Attar[2] suggested that the final products of the reaction depend on temperature, pyrite particle size and oxygen partial pressure.

The Mössbauer effect has also been used by Huffman and Huggins[5] to study the residual ashes in coal. They observed the transformation of pyrite to hematite, siderite to hematite, and of ankerite and Fe^{2+} in clays to ferric ions in glassy materials. The composition of the ashes was strongly dependent on the original minerals and the cooling conditions.

In this work we report a series of *in situ* Mössbauer measurements in four well-characterized bituminous coals. We intend to study the sequence of chemical reactions taking place during the transformation of the iron-bearing minerals. Special emphasis is placed upon the valence state of the iron and the identification of the intermediate states.

II. Experimental Description

The coals used in this study were: Blacksville #2, Powhatan #5, Ky 9/14 and IL #6 obtained from St. Clair County, Illinois. Table I gives the ultimate analysis of these four coals. The oxidation process was carried out in a specially built reactor. The reactor chamber consists of a quartz cylinder with an outer diameter of 2.5 cm. The sample was mounted in the center of the cylinder allowing the flow of air through it. The quartz tube was placed inside a horizontal furnace capable of reaching 1200°C. A chromel-alumel thermocouple was inserted into the middle of the reactor near the sample to detect the temperature. The reactor was held

horizontally. The sample, a coal pellet, was mounted between two graphite holders in the center of the reactor. For the process of oxidation, air was allowed to flow through the sample at a constant rate. A computerized Mössbauer spectrometer was used in this study to accumulate, record and fit the data. The fitting is based on a non-linear least-square procedure assuming Lorentzian-like shapes. The source used was a ~100 mCi ^{57}Co in a rhodium matrix. A krypton (3% CH_4) proportional counter was used as a detector (care was taken to cool the windows of the detector during the measurements). In situ ^{57}Fe Mössbauer spectra of all the samples were recorded during oxidation at various temperatures between 22°C and 710°C. All the isomer shifts are given in reference to α-Fe (the zero velocity standard). The reduction measurements were performed under hydrogen flow as well as under a nitrogen atmosphere.

III. Experimental Results and Discussion

The Mössbauer spectra of all the coals at room temperature show the presence of FeS_2 (pyrite) in various amounts. The spectrum of pyrite is known to give a characteristic quadrupole split doublet, isomer shift (IS) = 0.31 mm/sec and quadrupole splitting (QS) = 0.61 mm/sec. In all the coals depending on the degree of weathering (room temperature oxidation), the presence of $FeSO_4 \cdot H_2O$ (szomolnokite) was observed, IS = 1.18 mm/sec and QS = 2.69 mm/sec. In some samples minor amounts of jarosite and coquimbite (ferric sulfates) were also observed. The major iron-bearing clay minerals detected in the present experiments were illite and mixed clays (as detected by x-ray diffraction). The amount of iron in such minerals is very small and detection becomes easier after analyzing the high temperature ashes. On heating the coal in air, FeS_2 will be oxidized to a mixture of sulfates and oxides, and we would expect the Mössbauer spectrum to consist of a superposition of a magnetically split six-line pattern due to the iron oxides and doublets resulting from unreacted FeS_2 and iron sulfates. The above reactions could be summarized as:

$$FeS_2 + 3O_2 \rightarrow FeSO_4 + SO_2 \qquad 1)$$

$$3FeS_2 + 10\ O_2 \rightarrow FeSO_4 + Fe_2(SO_4)_3 + 2SO_2 \qquad 2)$$

$$Fe_2(SO_4)_3 \rightarrow Fe_2O_3 + 3SO_3$$

In Figures 1 and 2 the in situ Mössbauer spectra for the Blacksville #2 and IL#6 coal are shown. On heating the coals through the various temperatures it was observed 1) for FeS_2, the QS remains almost unchanged but its isomer shift decreases rapidly. The decrease in the IS is attributed mainly to the second order Doppler shift. 2) For $FeSO_4 \cdot H_2O$, the QS is observed to decrease at high temperatures. This decrease is mainly due to the temperature dependence of the electric field gradient (through population of excited electronic states). The area fraction of iron sulfates increased with temperature; this is due to the formation of sulfates through reactions (1) and (2). On increasing the temperature above 300°C and for short periods of time, the formation of ferrimagnetic γ-Fe_2O_3 is observed (see reference 1). The formation of γ-Fe_2O_3 has also been reported by other authors.[6] On further heating the coal to 350°C, the conversion of γ-Fe_2O_3 to α-Fe_2O_3 is observed (easily detected by the difference in magnetic hyperfine fields). The conversion of γ-Fe_2O_3 to α-Fe_2O_3 is complete at 400°C, and a characteristic six-line pattern due to α-Fe_2O_3 is observed. The presence of γ-Fe_2O_3 as an intermediate state depends on the coal as well as oxidation time. The longer the time, the more γ-Fe_2O_3 to α-Fe_2O_3 conversion is observed. Of course at higher temperatures only α-Fe_2O_3 is stable. How the coal composition affects the amount of γ-Fe_2O_3 formed is not well understood, although one is inclined to believe that particle size and impurities in the pyrite (or marcasite) would be important factors in this process. The above was also observed in all the coals studied. Two typical room temperature spectra for the Blacksville #2 and IL#6 coals are shown in Figures 3 and 4. The six-line spectrum characteristic of α-Fe_2O_3 is easily observed as the dominant feature in the figures. Noted is the presence of

two extra doublets containing Fe^{3+}, attributed to decomposition of the clays and formation of amorphous materials with Fe^{3+} as an impurity. The doublets are not identical in both spectra indicating that the environment of Fe^{3+} is different. This is indicative of a variation in clay composition between the two coals. Because of the small amounts of iron in such phases, their clear identification is rather difficult and still remains a challenging problem for the spectroscopist. Similar spectra were also observed for the other two coals.

The Mössbauer spectral area of each species was used to determine the relative amounts of FeS_2, Fe^{2+}, Fe^{3+} (not as oxide) and Fe_2O_3. In this analysis we will neglect any variation in Debye-Waller (D-W) factors between the different species. Consequently the relative amounts will indicate the qualitative variation in sample composition at the different temperatures. The absolute amounts vary depending on their respective D-W factors. Since such a correction is very difficult, we limit ourselves to the assumption that all the species show a similar temperature dependence for the D-W factors. Figure 5 shows the decomposition of FeS_2 as a function of temperature for all the coals under study. Figure 6 shows the amount of Fe^{2+} as a function of temperature for all the coals; the divalent ion contribution is mainly from the ferrous sulfates. In Figure 7 the variation in Fe^{3+} and iron oxides (both γ and α) are shown as a function of temperature. It is evident that for the most weathered coals, there is more ferric sulfate present (e.g. IL#6). For the fresher coal (BL#2), the amount of ferric sulfate is smaller and the transformation from iron sulfides to sulfates to oxides is rapid. At 710°C the ferric ion is present mainly as α-Fe_2O_3. At this temperature we are above the antiferromagnetic to paramagnetic transition temperature of α-Fe_2O_3 and no magnetic splitting is observed. The α-Fe_2O_3 particle sizes seems to be very similar in all the coals studied. This is evident from Figure 8 where the normalized magnetic hyperfine field at the ^{57}Fe nucleus is plotted versus temperature. The temperature dependence is very similar for all the samples (only α-Fe_2O_3 plotted) indicating similar particle sizes. Most likely sintering has occurred during combustion. Weathering of the coal seems to be one of the major factors hindering the rapid conversion of FeS_2 to oxides at low temperatures. Eventually at higher temperatures the ferric sulfate particles are converted to oxides. It appears that the presence of particles of ferrous and ferric sulfates slows down the rapid oxidation of FeS_2. There is also a physical factor present. It is highly probable that the smaller sulfide particles were oxidized at room temperature in a weathered coal and the remaining particles are larger and more difficult to oxidize.[1,2] It is evident that the fresher coal oxidized faster than the others (see Figure 7).

Under reduction conditions and below 450°C, all the iron sulfides are transformed into pyrrhotites. The degree of transformation depends on time as well as the type of coal.[7] The major factor affecting the Fe/S ratio in the pyrrhotites is the total amount of sulfur available as H_2S. Partial H_2S pressure is the crucial quantity controlling the stoichiometry of the pyrrhotites. A high percentage of H_2S in the reactor at high temperatures assures the formation of pyrrhotites with a high number of metal vacancies. The pyrrhotite surface interacts with CO and CO_2 in the presence of hydrogen. The products are removed from the surface and the pyrrhotites retain a metal character. At temperatures higher than 450°C the pyrrhotites start to transform into troilite and eventually into iron metal. The formation of troilite (FeS) is also possible at lower temperatures if H_2S is continually removed from the reactor by flowing hydrogen. The clay minerals are also transformed during reduction with the iron ion preferring to retain a divalent state. The degree of transformation is strongly coal dependent.

The authors acknowledge the support of the Energy Research Center of West Virginia University.

REFERENCES

1. Shyu, H.J., Vaishnava, P.P., and Montano, P.A., Fuel 60, 1023 (1981).

2. Attar, A., Fuel 57, 201 (1978).

3. Wendeborn, H., "Der Chemie-Ingenieur," Vol.III, 5, edited by A. Eucker and M. Jacob, 334.

4. Schwab, G.M. and Philinis, J., J. Amer. Chem. Soc. 69, 2588 (1947).

5. Huffman, G.P. and Huggins, F.E. in "Recent Chemical Applications of Mossbauer Spectroscopy," eds. J. Stevens and G.K. Shenoy, ACS, Advances in Chemistry, 194 (1980).

6. Marusak, L.A., Walker, Jr., P.L. and Mulay, L.N., IEEE Trans. Mag. MAG-12(6), 889 (1976).

7. Bommannavar, A.S. and Montano, P.A., Fuel 61, 523 (1982).

TABLE I Ultimate Analysis (WT%, dry basis)

Coal	H	C	N	S	O	HTA
IL#6	4.7	67.6	1.2	4.0	8.0	13.96
Powhatan #5	4.9	71.1	1.1	3.5	7.5	11.8
Ky 9/14	4.9	71.3	1.5	3.4	9.7	9.3
Blacksville #2	5.2	75.83	1.4	3.4	3.5	10.1

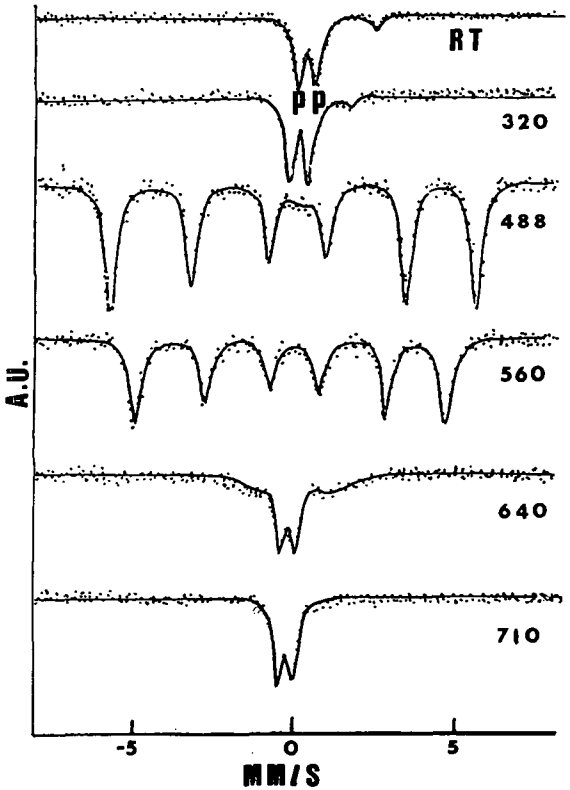

FIGURE 1 Mossbauer spectra of the Blacksville #2 coal as a function of temperature: pp indicates the position of pyrite.

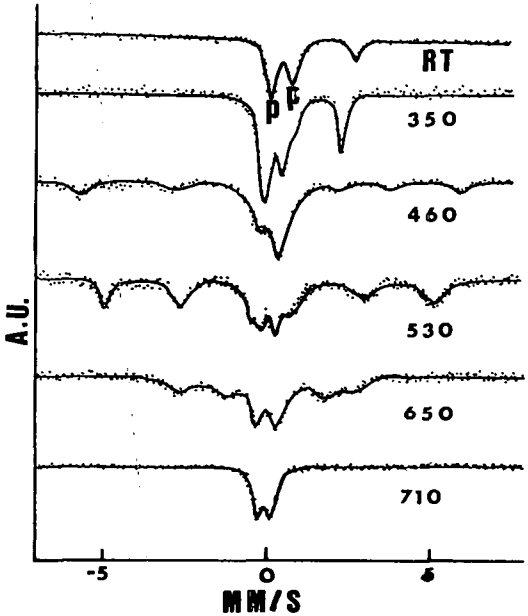

FIGURE 2 Mossbauer spectra of the IL #6 coal as a function of temperature.

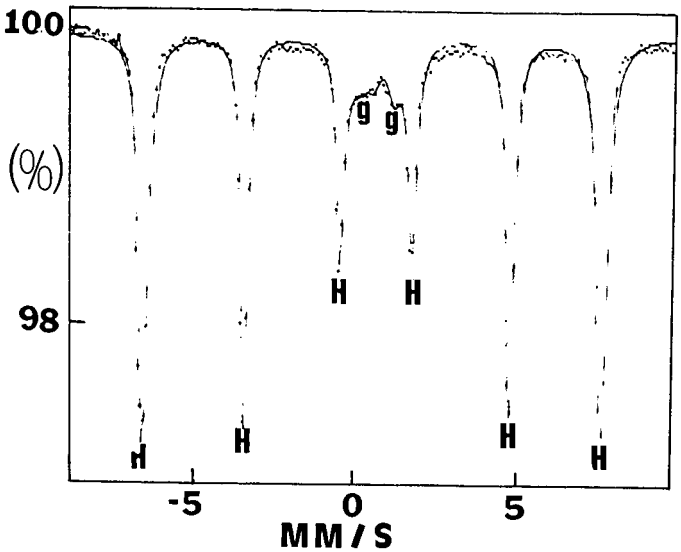

FIGURE 3 Mössbauer spectrum at room temperature after oxidation at 710°C of the Blacksville #2 coal. H: α-Fe_2O_3
g: Fe^{3+} in amorphous clay (two doublet)

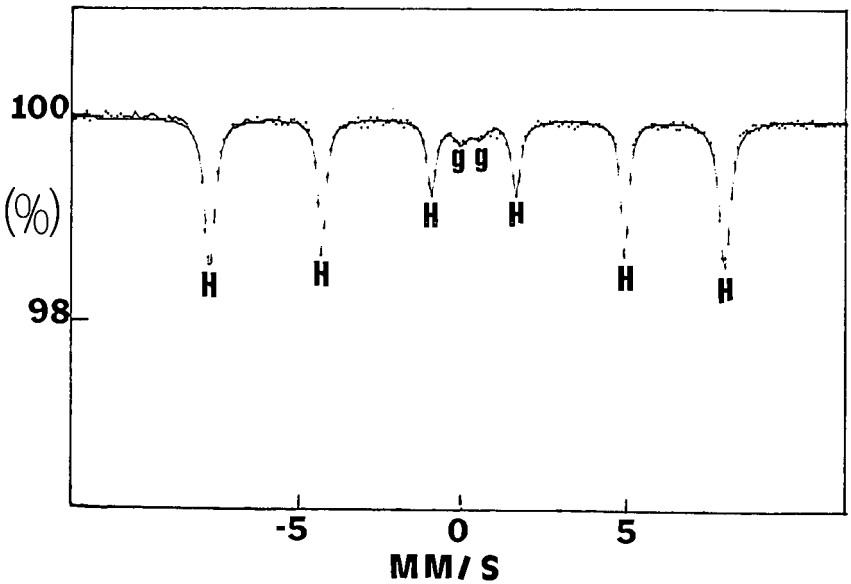

FIGURE 4. The same as above but IL #6 instead of Blacksville #2.

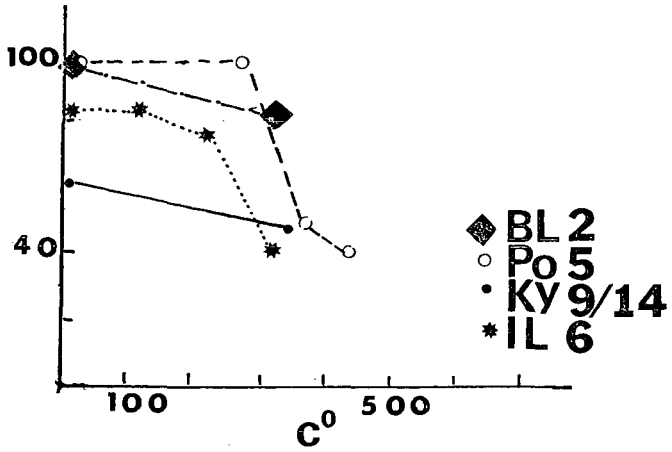

FIGURE 5 Decomposition of FeS_2 in percent as a function of temperature. BL2: Blacksville #2; Po5: Powhatan #5; Ky 9/14; and IL6: IL #6.

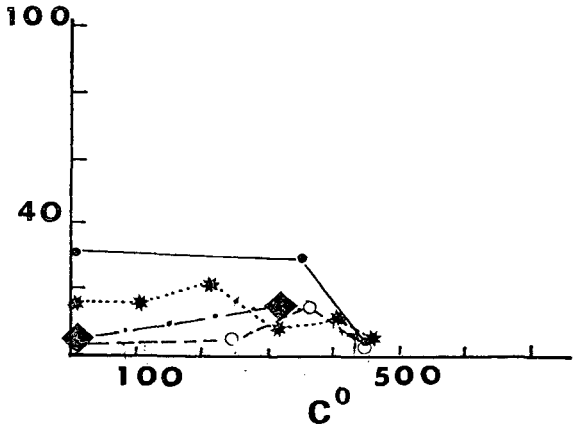

FIGURE 6 Transformation of Fe^{2+} in percentage vs. temperature. Key to the figure is found in Figure 5.

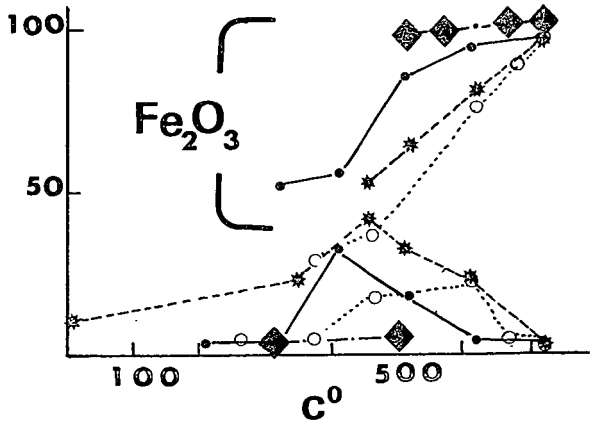

FIGURE 7 Conversion to Fe_2O_3 and Fe^{3+} (not oxides) as a function of temperature. See Figure 5 for the key to the symbols.

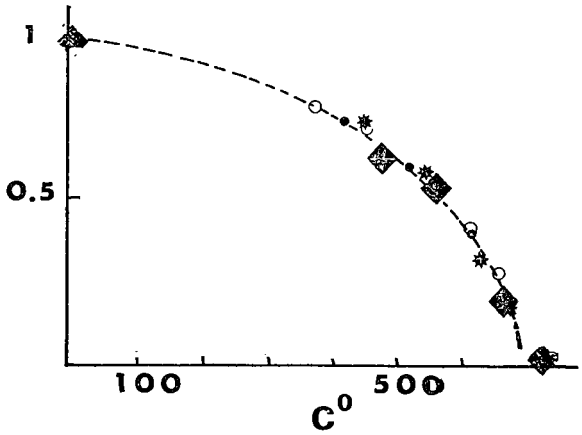

FIGURE 8 Magnetic hyperfine field normalized to room temperature for all the samples vs. temperature.

Enumeration of Graphite Carbon-Bond-Network Defects Having Ring Sizes Ranging from 2 to 9.

Jerry Ray Dias

Department of Chemistry
University of Missouri
Kansas City, Missouri 64110

Graphite-like Structures

A covering of the plane by congruent regular n-gons (all vertex angles and edge lengths are equal) is called a *regular* tessellation of the plane (1). The graphite σ-bond structure is a regular tessellation of the plane by hexagons. The only regular tessellations of the plane by n-gons are for n = 3,4, and 6; no other regular tessellations of the plane exist. If m denotes the number of regular n-gons at every vertex, then $m(1-2/n)\pi = 2\pi$ which simplifies to $1/n + 1/m = \frac{1}{2}$. *Homogeneous* tessellations (all edge lengths are equal) occur when different polygons are used with the same set of polygons at each vertex. Since the number of n-gons at every vertex is three for the graphite σ-bond structure, the various isomeric graphite tessellations in a plane must be given by $(1-2/n_1) + (1-2/n_2) + (1-2/n_3) = 2$ which simplifies to $1/n_1 + 1/n_2 + 1/n_3 = \frac{1}{2}$. The only acceptable solutions to the latter equation for n_1, n_2, n_3 are 6,6,6 or 3,12,12 or 4,6,12 or 4,8,8. These translate to the tessellated structures shown in Figure 1. Note that these tessellated graphite related structures are listed in decreasing order of their aromatic or pπ-bond energy stability associated with polycyclic conjugated hydrocarbons where the hexagonal web (n_1 = 6, n_2 = 6, n_3 = 6) is totally aromatic, the middle structures are either less aromatic (n_1 = 3, n_2 = 12, n_3 = 12) or have aromatic and antiaromatic components (n_1 = 4, n_2 = 6, n_3 = 12), and the latter structure is almost totally antiaromatic (n_1 = 4, n_2 = 8, n_3 = 8). The homogeneous tessellated structures (Figure 1) have only angle distortions from the ideal angle of 120° for the graphite structure. If bond (edge) distortions are permitted then other planar lattice structures become possible (2). They include plane nets composed of an equal number of pentagonal and heptagonal rings or trigonal and nonagonal rings and twice the number of pentagonal rings to octagonal rings or twice the number of heptagonal rings to tetragonal rings in compliance with the equation $3r_3+2r_4+r_5-r_7-2r_8-3r_9-4r_{10}-5r_{11}-6r_{12}-\cdots = 0$ (*vide infra*) where r_n is the number of rings of size n.

These other graphite lattices are unknown but can possibly exist as island defects in graphite or amorphous carbon (carbon-bond-network defects). Twinning of graphite crystals result in the formation of 4- and 8-membered rings along the twinning line. Similarly, a partial lateral dislocation leads to a similar 4-8 boundary. A single carbon-atom-lattice-vacancy forms a hole shaped like peri-naphthenyl radical and a two-carbon-atom-lattice-vacancy forms a hole shaped like pyrene (3). A partial line dislocation can produce a sp^3-hybridization-buckled-network defect (4). Other types of graphite defect structures involve layer stacking and foreign atom incorporation. The 419 other isomers of pyrene enumerated in a previous paper also represent other possible carbon-bond-network defect structural units that may possibly exist as localized islands in graphite and amorphous carbon (5).

Diamond-like Structures

There are two basic three-dimensional 4-connected nets or lattices that can be constructed with equal links and regular tetrahedral bond angles (6). The most stable is the (cubic) diamond-like lattice which is made up of the totally staggered arrangement of links where each and every two-tetrahedral-atom unit resembles the staggered conformation of ethane and every six-tetrahedral-atom ring system resembles the chair conformation of cyclohexane. The less stable wurtzite-like (hexagonal diamond) lattice is composed of 1/4 eclipsing links and 3/4 staggered links and has (normal) layers of made up of fused polycyclic hexagonal rings in chair conformational-like arrangements which are mutually joined in such a way that boat conformational-like hexagonal rings are formed between these layers. A lattice which alternates in a regular or periodic manner between the cubic and hexagonal diamond structures could lead to the SiC polytypes. Two other lattices possible for 4-connected tetrahedral atoms are worthy of note (6). One is based on the cyclopentagon which has an internal angle of 108° that is close to the regular tetrahedral angle value of 109.5°. A net which radiates out from a central pentagonal dodecahedron can be constructed. The other is based on the planar (and angle strained) cyclohexagon. An infinite net which radiates from a column of planar cyclohexagons leads to a structure that can be described as a 6-fold rotation twin of cubic diamond.

Isomer Enumeration of Polycyclic Conjugated Hydrocarbons

Consider the σ-bond graphs of three of the 420 possible polycyclic conjugated hydrocarbon isomers of pyrene shown in Figure 2 (5). Pyrene (*1*) has $N_{Pc}=4$ peripheral third degree carbon vertices (numbered 1 to 4), isomer *2* has $N_{Pc}=5$, and isomer *3* has $N_{Pc}=6$; all pyrene polycyclic conjugated isomers have $N_H=10$ second degree vertices on the periphery of their σ-bond graphs. Note that the previously derived equation of $N_{Pc}-N_H+6=3r_3+2r_4+r_5-r_7-2r_8-3r_9-\cdots$ correctly enumerates the relative number of ring sizes different from the hexagonal ring in these three pyrene isomers (*1* to *3*).

Carbon-Bond-Network Defects in Graphite

The principle assumption in this treatment of carbon-bond-network defects is that this kind of defect is formed in an initially ideal graphite lattice in such a manner that the initial number of carbon atoms are conserved (i.e., Frenkel-like defects). Also, the graphite crystal is regarded basically as a super-large polycyclic aromatic hydrocarbon and that these carbon-bond-network defects occur remote to the crystal edge; under these conditions $N_{Pc}-N_H+6=q_p-2N_H+6=3r_3+2r_4+r_5-r_7-2r_8-3r_9=0$ since $N_{Pc}-N_H+6=0$ for benzenoid PAHs. A two-dimensional projection on the $(1\bar{1}0)$ plane of the diamond lattice gives a 6-gon tessellated structure with hexagonal rings possessing two shortened parallel edges. Dislocations in the diamond lattice of silicon parallel to this $(1\bar{1}0)$ plane result in ring size combinations which obey the above general equation as a consequence of avoiding energetically unfavorable dangling bonds (7). A $(1\bar{1}0)$ projection of the diamond-cubic lattice of germanium containing an intrinsic Z-shaped faulted dipole was shown to exhibit a combination of pentagonal and heptagonal rings ($r_5-r_7=0$) which complies with the above equation (8). A study of <011> tilt boundaries in the diamond-cubic lattice gave a two-dimensional projection showing ring size combinations consistent with this equation (9).

Naphthalene has only four polycyclic conjugated hydrocarbon isomers as enumerated in Figure 3. If one takes an ideal graphite lattice, excises out a naphthalene substructure, and replaces it with a substructure corresponding to the other three naphthalene isomers, one obtains the three carbon-bond-network defects enumerated in Figure 4; the graphite partial structure shown in Figure 4 will be

referred to as the ovalene graphite cell. Similarly, if one excises out a pyrene substructure from an ideal graphite lattice and replaces it with another substructure corresponding to one of the other 419 isomers of pyrene, one obtains other carbon-bond-network defects. Note that for all the defect graphite cell structures shown in Figure 4, the combination of ring sizes is predicted by $3r_3+2r_4+r_5-r_7-2r_8-3r_9=0$. If one distinguishes between rings of the naphthalene the outer rings formed upon their insertion into the ovalene graphite cells, then the equation $3r_3+4r_4+5r_5+6r_6+7r_7+8r_8+9r_9= q_p+2q_I$ can be partitioned into the two following equations where the superscript "i" designates "inner" and the superscript "o" designates "outer" ring system:

$$3r_3+4r_4+5r_5^i+6r_6^i+7r_7^i+8r_8^i+9r_9=q_p^i+2q_I^i$$

$$5r_5^o+6r_6^o+7r_7^o+8r_8^o=q_p^o+2q_I^o$$

These equations with specific values for q_I^i, q_p^i, q_I^o, q_p^o, and N_{Ic}^i are given in Figure 4. If one excises the pyrene structural unit from the circumpyrene ideal graphite cell, rotates the pyrene structural unit, and reinserts it, then one obtains another carbon-bond-network defect. Thus there are probably more than 419 different elementary carbon-bond-network defects since each of the different 420 structural isomeric units of pyrene can be inserted with different orientations into the empty circumpyrene graphite cell. The simplest carbon-bond-network defect is that graphite cell corresponding to azupyrene since the surrounding graphite hexagonal units would be nearly normal. Carbon-bond-network defects having ring sizes 3 to 9 are shown to be most probable within the constraints of this model.

A recent example of thermal (500°C) isomerization of azupyrene to pyrene has been published (10). This example (Figure 5) is probably mechanistically the simplest type of isomerization possible for pyrene isomers since a pairwise detachment and reattachment exchange of *syn* internal bonds to the internal third degree carbon atom vertices would convert azupyrene to pyrene. Annealing graphite with analogous defects can cause their migration to the surface or annihilate them as shown in Figure 5.

Although large vacancy defects no doubt exist in graphite, one or two carbon-atom-lattice-vacancies most likely do not exist. Point defects have excess energy due to strain and dangling bonds. Each dangling bond amount to ∿2.5eV, and thus there will be a tendency to form point defects which minimize the number of dangling bonds. Consider a two carbon-atom-lattice-vacancy which forms a hole which is shaped like pyrene (3); the four dangling bonds in this defect could form two bridging bonds if some lattice distortion and associated strain energy is permitted. Since it is likely that this strain energy is less than 10 eV, the equilibrium in Figure 6 probably lies to the right side of the equation; note that the equation $3r_3+2r_4+r_5-r_7-2r_8-3r_9=0$ is again obeyed (i.e., $r_5-2r_8=2-2x1=0$).

These examples demonstrate the broad applicability of the general equation $3r_3+2r_4+r_5-r_7-2r_8-3r_9-\cdots=0$ for predicting the relative number of nonhexagonal ring sizes in planar graphs of molecular carbon systems where minimization of dangling bonds is a dominant energetic factor. Amorphous carbon can be regarded as a mix of graphite and diamond lattice types and carbon-bond-network defects (11). These structural concepts should be useful in study of the mechanism of carbonization by which pitch is thermally converted to coke and coke to graphite (12).

References

1. Berman, G., Fryer, K. "Introduction to Combinatories;" Academic Press New York, NY, 1972.
2. Balaban, A. T., Rentia, C. C., Ciupitu, E. *Rev. Roum. Chim.* 1968, *13*, 231.
3. Kelly, B. T. "Physics of Graphite;" Applied Sci. Pub.: NJ, 1981.
4. Ubbelohde, A. R., Lewis, F. A. "Graphite and its Crystal Compounds;" Oxford Univ. Press: London, England, 1960.
5. Dias, J. R. *Match* (*Math. Chem.*) 1983, *14*, 83.
6. Wells, A. F. "Three-Dimensional Nets and Polyhedra;" John Wiley & Sons, Inc.: NY, 1977, Chapter 9.
7. Tan, T. Y. *Phil. Mag. A* 1981, *44* (1), 101-140.
8. Chiang, S.-W., Carter, C. B., Kohlstedt, D. L. *Phil. Mag. A* 1980, *42* (1) 103-121.
9. Moller, H.-J. *Phil. Mag. A* 1981, *43* (4), 1045-1055
10. Anderson, A. G., Kao, L. G. *J. Org. Chem.* 1982, *47*, 3589.
11. Dias, J. R. *Carbon*, in press.
12. Lewis, I. C. *Carbon* 1982, *20*, 519.

APPENDIX: Glossary of Terms

N_c - total number of carbon atoms in a PAH

N_H - total number of hydrogen atoms in a PAH

N_{Ic} - number of internal carbon atoms in a PAH having a degree of 3

N_{Pc} - number of peripheral carbon atoms in a PAH having a degree of 3

PAH6 - polycyclic aromatic hydrocarbon containing exclusively fused hexagonal rings

$|P|=p=Nc$ - total number of graph points

p_3 - number of graph points (vertices) having a degree of 3

$|Q|=q$ - number of graph edges (lines or C-C bonds)

q_I - number of internal graph edges

q_p - number of peripheral graph edges

q_b - number of graph edges connecting to phenyl-like ring substituents

r - number of rings

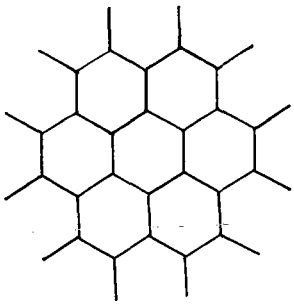

$n_1 = 6,\ n_2 = 6,\ n_3 = 6$

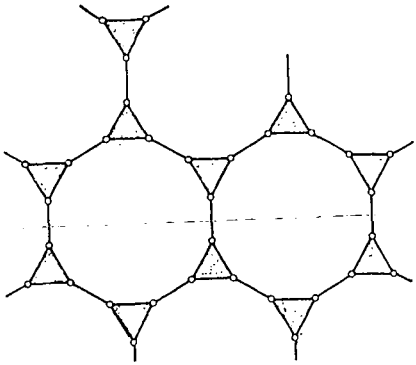

$n_1 = 3,\ n_2 = 12,\ n_3 = 12$

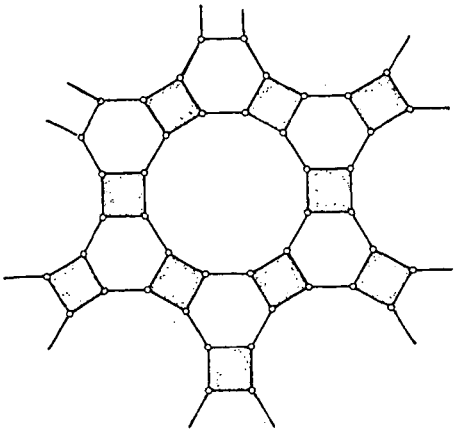

$n_1 = 4,\ n_2 = 6,\ n_3 = 12$

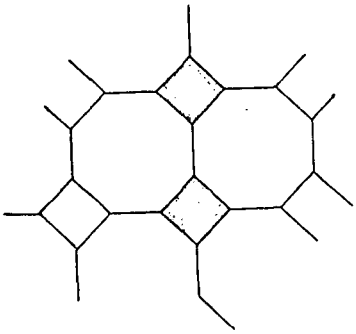

$n_1 = 4,\ n_2 = 8,\ n_3 = 8$

Figure 1 . Graphite related tessellated structures.

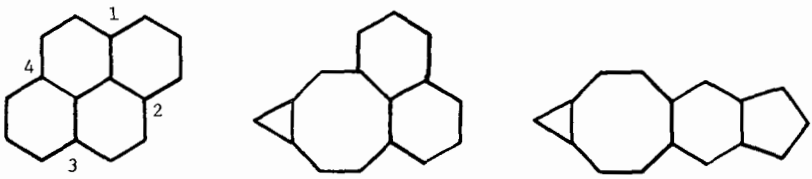

Pyrene

1 *2* *3*

Figure 2. Three of the 420 possible polycyclic conjugated hydrocarbon isomers of pyrene.

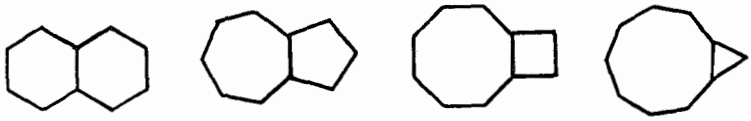

Naphthalene Azulene

Figure 3. Polycyclic conjugated isomers of naphthalene.

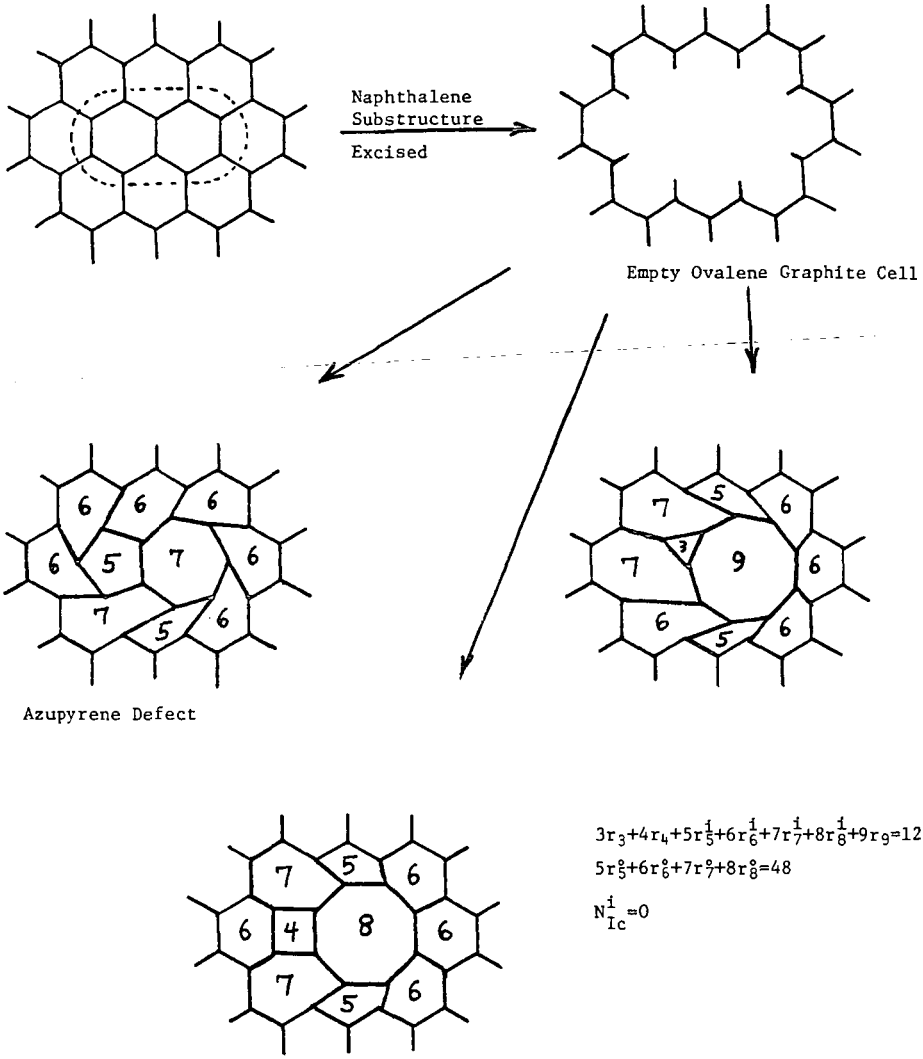

$$3r_3+4r_4+5r_5^i+6r_6^i+7r_7^i+8r_8^i+9r_9=12$$

$$5r_5^o+6r_6^o+7r_7^o+8r_8^o=48$$

$$N_{Ic}^i=0$$

Figure 4. Carbon-bond-network defects in ovalene graphite cells.

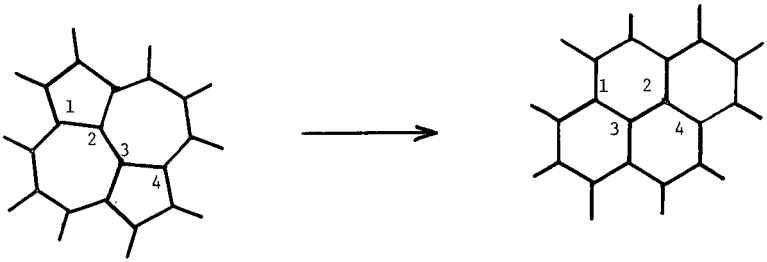

Azupyrene defect

Figure 5. Thermal isomerization of azupyrene to pyrene.

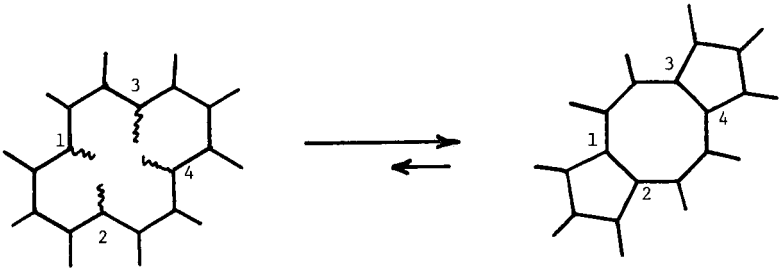

Figure 6. Example of minimization of dangling bonds.

INFLUENCE OF PARTICLE STRUCTURE ON THE RATE OF GAS-SOLID GASIFICATION REACTIONS

K. A. Debelak, J. T. Malito and R. M. Patrick

Department of Chemical Engineering
Vanderbilt University
Nashville, TN 37235

Introduction

Changes in structural parameters, such as surface area available for reaction, porosity, and pore size distribution, will markedly affect the rate of gas-solid reactions. Accompanying these changes in structural parameters are changes in the resistance to diffusion of gaseous products and reactants through the pores of the solid. Understanding the nature of this diffusion, therefore is important in predicting simultaneous diffusion and reaction rates. A quantitative measure of pore diffusion for first-order reactions is given by the effectiveness factor which is a unique function of the effective diffusivity. For microporous solids such as coal, there have been few measurements of effective diffusivity. Furthermore, the effective diffusivity changes as a function of coal conversion as pore walls are gasified. The objective of this work is to determine the changes in the particle structure of coal as it undergoes the reaction, $C + CO_2 \rightarrow 2CO$ and to include the effect of these changes in surface area and effective diffusivity on the overall reaction rate.

A number of workers (1-6) have made measurements of changes in surface area as a function of conversion. Most report that surface area increases during reaction. Only Turkdogan et al (1) and Patel el al (7) have made any measurements of effective diffusivity as a function of conversion. The changes in effective diffusivity, D_e, and total surface area, S, may be expressed as functions of conversion. Once these functions are established, they can be included in an overall rate expression. Recently Bhatia and Perlmutter (8) and Gavalas (9) have developed random pore models for gas-solid reactions at chemically controlled rates. These models can be shown to be essentially identical (10). In both cases expressions have been derived which relate surface area to conversion. Bhatia and Perlmutter (11) have extended their model to include diffusion and transport effects where they assume that effective diffusivity will vary with the structural parameters of the solid in the form $D_e = D\varepsilon/\gamma(\varepsilon)$ where $\gamma(\varepsilon)$ is the tortuosity which varies as reaction proceeds. The random pore models provide a way to interpret rate data in terms of the measurable parameters of surface area and effective diffusivity.

Experimental

The experimental equipment to determine surface and effective diffusivity is the same as used previously (12). The surface area device is a flow-type adsorption apparatus. Surface area measurements were made by adsorbing CO_2 at 0°C for 1 hour. The adsorbed CO_2 was then desorbed by heating the sample at 120°C. This process was repeated at several relative CO_2 pressures to obtain an adsorption isotherm. The surface area was calculated using the Dubinin-Polanyi theory (13) with modifications by Medek (14). Effective diffusivity determinations were made by pulsed chromatography employing the method of moments. The theoretical model used to describe the mass transfer in the chromatographic bed was the same as used previously (12). Axial dispersion and external mass transfer coefficients

were determined from correlations in Shah and Ruthven (15) and Bird (16), respectively. From the two moment equations the adsorption constant K_a and the diffusion parameter D_e/r_c^2 where D_e is effective diffusively and r_c is diffusion length were calculated. These diffusion studies were made on CO_2, CO, CH_4, and N_2 over a temperature range of 50°C to 250°C. To produce char, a sample of raw coal was heated at 25°C/min to the reaction temperature in a helium gas stream and held at reaction temperature for 1 hour. The sample was cooled and surface area and effective diffusivity measurements were made again. The chars produced were reheated to reaction temperature and reacted with CO_2. A known volume of CO_2 was injected and the outlet gas was collected and analyzed to determine the extent of the reaction. The sample was then cooled and surface area and effective diffusivity measurements were made. The sample was then reheated and reacted again. This procedure was repeated until there was no further appreciable carbon conversion. Measurements of reaction rates for the char/CO_2 reaction were made using a thermal gravimetric balance. Devolatilization temperatures and reaction temperatures ranged from 1073K to 1373K.

Results and Discussion

There are significant changes in the surface area and diffusion parameter as a result of devolatilization. Table 1 gives these changes at different devolatization temperatures. The char surface areas are from 1.5 to 2.0 times as great as the raw coal. The ratio of char/coal surface area increases as devolatilization temperatures increases and reaches a maximum at 1273K and then decreases. The increase in surface area represents the opening of pores inaccessible before devolatilization. Walls closing off pores are devotalized and small pores inaccessible to initial CO_2 adsorption are exposed. As the devolatilization temperature increases to 1373K the amount of new pores structure begins to decrease as more material is devolatilized. The ratios of the char/coal diffusion parameters for N_2 are less than one indicating that the new pore structure has a greater resistance to diffusion. The ratio of char/coal diffusion parameter increases as devolatilization temperature increases but is still less than one. The devolatilization process produces an increase in surface area and a decrease in diffusion parameter.

The CO_2/char gasification reaction causes continuous changes in the pore structure of the char. Specific surface area initially increases, passes through a maximum and then decreases as a function of conversion. The specific surface area was correlated with conversion using Bhatia and Perlmutter's expression for surface area as a function of conversion. Figures 1-4 are plots of surface areas versus conversion using the Bhatia and Perlmutter model at each reaction temperature. From the slope and intercept of the least squared line an initial surface area S_o, and a structural parameter, ψ were calculated. These values along with the measured initial surface areas are given on Figures 1-4. The calculated and measured initial surface areas disagree by as low as 2.5% and as high as 33%. Bhatia and Perlmutter's model indicates that when the structural parameter ψ is greater than 2 that there is a maximum in surface area as a function of conversion. All the values of ψ determined are greater than 2 and the values of ψ increase as a function of reaction temperature up to 1273K and then decrease at a reaction temperature of 1373K. Bhatia and Perlmutter's model has not been widely tested, and the range of conversion over which it applies has not been established. The data of Hashimoto et. al (6) correlated to a conversion of 0.75 for one char and to a conversion of 0.3 for another char. These data correlate from conversion of 0.40 at 1373K to 0.75 at 1173K.

The calculated diffusion parameter, D_e/r_c^2, and the adsorption equilibrium constant, K_a for the diffusion of carbon dioxide in helium as a function of conversion are displayed in Table 3. The diffusion parameters and equilibrium constants for carbon monoxide, nitrogen and methane as a function of conversion and at different reaction temperature also were calculated but are given elsewhere (17). There is an increase in diffusion parameter with conversion. There appears to be an inverse relationship between the adsorption constant and the diffusion parameter. Intuitively, as the pore structure becomes more open, or as the reactive core decreases in diameter, the resistance of mass transfer decreases.

Walker, et al studied the diffusion of methane in coals and determined that diffusion is activated (18,19). An Arrhenious relationship was proposed to explain the influence of temperature on the diffusion parameter. Activation energies, $\Delta H_0^{\ddagger}$, and pre-exponential factors, $(D_e/r_c^2)_0$ parameters were calculated from diffusion data obtained at 100°C or greater. The results are listed in Table 6 for char reacted at 1073K. For all gases the activation energy generally decreases with conversion, as expected, since higher energies are associated with smaller pores and pore entrances and with smaller reactive core radii. Patel, et al (7) also observed a decrease in the diffusion of methane through various activated anthracite coals. Activation energies and pre-exponential factors as a function of conversion at the other reaction temperatures are available elsewhere (17). Using calculated activation energies and pre-exponential factors, diffusion parameters were estimated at reaction temperatures. These parameters vary non-linearly with conversion and follow the order $N_2 > CO > CH_4 > CO_2$.

Reaction rate data for char/CO_2 reaction obtained using the TGA exhibited maxima at intermediate conversions. The Bhatia and Perlmutter model assuming a kinetically controlled reaction and rearranged in linear form was used to interpret the rate data. Values of ψ and S_0 determined from the surface area studies were used in the model. These data are plotted in Figures 5-8. Reaction rate constants were calculated from the slopes of these plots. An Arrhenious plot for the reaction rate constants is given in Figure 9. An activation energy of 150 KJ/mole was calculated from the slope of this plot. The assumption of a kinetically controlled reaction appears to be correct since the reaction rate data in Figures 5-8 are linear as the Bhatia/Perlmutter model suggests and the Arrhenious plot is linear. However, effectiveness factors still need to be calculated and this is currently being done using the Bhatia/Perlmutter model which includes transport effects.

Conclusions

Devolatilization results in an increase in surface area and a decrease in diffusion parameter. A maximum increase in surface area occurs at a devolatilization temperature of 1273K whereas the diffusion parameters increases as devolatilization temperature increases. Specific surface area exhibits a maximum at a conversion of approximately 0.35. The Bhatia/Perlmutter is able to correlate the data to a conversion of at least 0.4. The structural parameter ψ has a maximum at reaction temperature of 1273K. The diffusion parameters, D_e/r_c^2, are conveniently estimated using the model of Shah and Ruthven (15) and method of moments. The diffusion parameter varies non-linearly with conversion and follows the order $N_2 > CO > CH_4 > CO_2$. The reaction of CO_2 with Wyodak char at temperatures between 1073K and 1373K can be modeled by the Bhatia/Perlmutter model assuming kinetic control. The activation energy is 150 KJ/mole. To confirm this, however, effectiveness factors need to be determined from the simultaneous solution of the equations describing diffusion and reaction including the functions accounting for changes in diffusivity and surface area as a function of conversion.

Acknowledgements

This work was supported by the U.S. Department of Energy Contract # DE-AC-21-81MC16053.

References

1. Turkdogan, E.T., Olsson, R.G., and Vinters, J.V., Carbon, 8, 545, (1970).

2. Kawahta, M., Walker, P.L., "Proceedings of the Fifth Carbon Conference, Vol. 2, 251, Pergamon Press, London, (1962).

3. Kalbach, W.M., Brown, L.F., West, R.E., Carbon, 9, 117, (1970).

4. Marsh, H., Rand, B., Carbon, 47, 79, (1971).

5. Berger, J., Siemieniewski, J., Tomkov, Fuel, 55, 9, (1976).

6. Hashimoto, K., et al., Ind. Eng. Chem. Process Des. Dev., 18, 72, (1979).

7. Patel, R.L., Nandi, S.P., and Walker, P.L., Jr., Fuel, 51, 47, (1972).

8. Bhatia. S.K., and Perlmutter, D.D., AIChE J., 26, 379, (1980).

9. Gavalas, G.R., AIChE J., 26, 577, (1980).

10. Scott, P.E., M.S. Thesis, Vanderbilt University, (1983).

11. Bhatia, S.K., and Perlmutter, D.D., AIChE. J., 27, 247, (1981).

12. Debelak, K.A., Clark, M.A., and Malito, J.T., ASC Div. of Fuel Preprints, No. 1, 31, (1982).

13. Gregg, S.J., and Sing, K.S.W., Adsorption Surface Area and Porosity, New York, Academic Press, 223, (1967).

14. Medek, J., Fuel, 56, 131, (1977).

15. Shah, D.B., and Ruthven, D.M., AIChE. J., 23, 804, (1977).

16. Bird, R.B., Stewart, W.E., Lightfoot, E.N., Transport Phenomena, New York, John Wiley and Sons, Inc., (1960).

17. Patrick, R.M., M.S. Thesis, Vanderbilt University, (1983).

18. Walker, P.L., Jr., and Kini, D.A., Fuel, 44, 453, (1965).

19. Nandi, S.P., and Walker, P.L., Jr., Fuel, 49, 309, (1970).

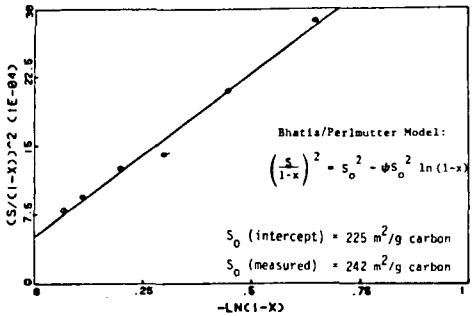

Figure 1. Plot of Bhatia/Perlmutter Model for Surface Area for Wyodak Char Reacted at 800°C ψ = 7.

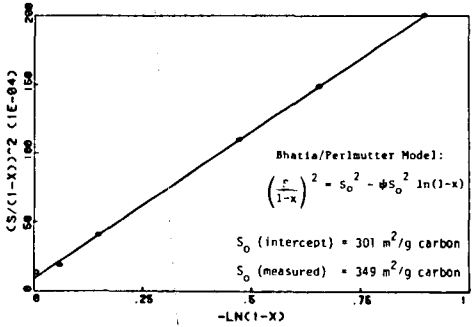

Figure 3. Plot of Bhatia/Perlmutter Model for Surface Area for Wyodak Char Reacted at 1000°C ψ = 23.6.

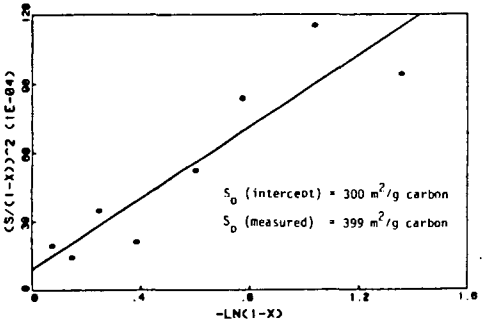

Figure 2. Plot of Bhatia/Perlmutter Model for Surface Area for Wyodak Char Reacted at 900°C ψ = 8.7.

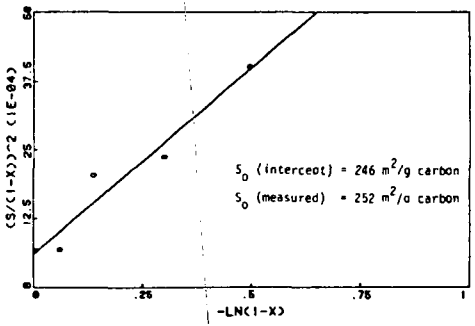

Figure 4. Plot of Bhatia/Perlmutter Model for Surface Area for Wyodak Char Reacted at 1100°C ψ = 11.2.

Bhatia/Perlmutter Model

$$\frac{(dx/dt)(1-\epsilon_o)}{C_{CO_2}[1-\psi \ln(1-x)]^2} = KS_o(1-x)$$

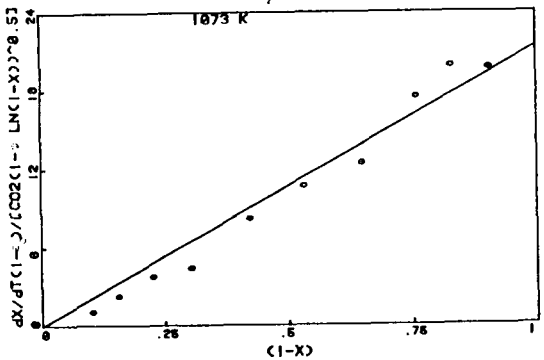

Figure 5. Reaction of Coal Char with Carbon Dioxide at 1073°K. Data fitted to B/P model.

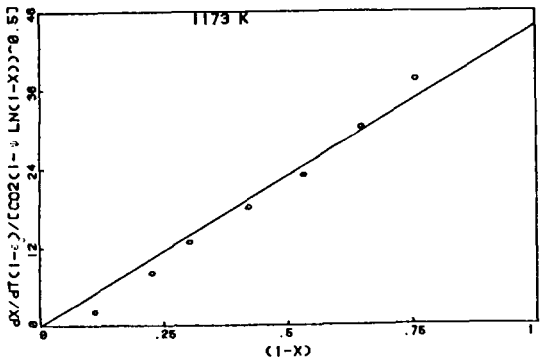

Figure 6. Reaction of Coal Char with Carbon Dioxide at 1173°K. Data fitted to B/P model.

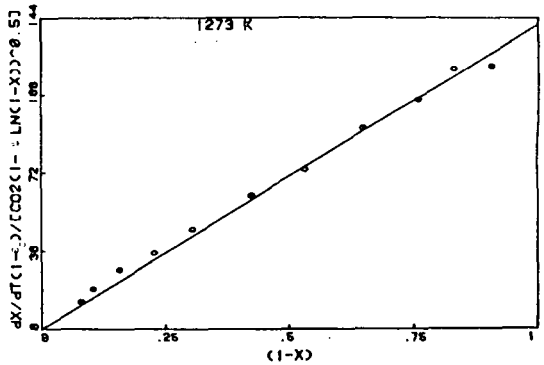

Figure 7. Reaction of Coal Char with Carbon Dioxide at 1273°K. Data fitted to B/P model.

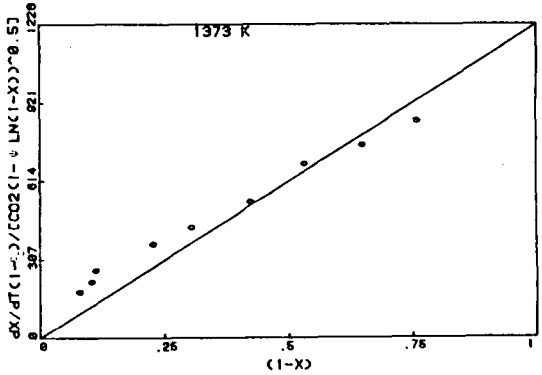

Figure 8. Reaction of Coal Char with Carbon Dioxide at 1373°K. Data fitted to B/P model.

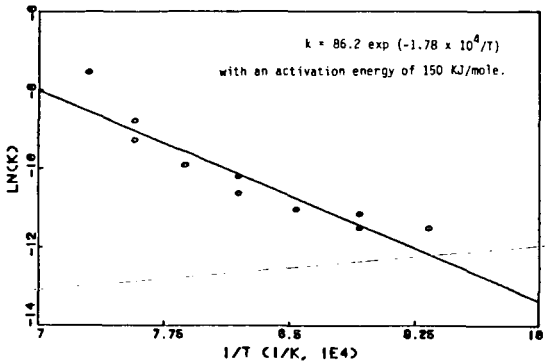

Figure 9. Arrhenius Plot for the Rates Constants.

TABLE 1

EFFECTS OF PYROLYSIS ON WYOMING SUBBITUMINOUS COAL

Pyrolysis Temperature (°K)	Weight (Char/Coal)	Ratio of Specific Area (Char/Coal)	Ratio of N_2 Diffusion Measured at 323°K (Char/Coal)
1073	.5605	1.81	.234
1173	.5855	1.90	.422
1273	.5749	2.03	.658
1373	.5527	1.47	.708

TABLE 2

WYODAK COAL CHAR REACTED AT 1073°K DIFFUSION PARAMETERS
AND ADSORPTION EQUILIBRIUM CONSTANTS FOR
CARBON DIOXIDE IN HELIUM

Conversion	Adsorption Constant, K_a					Diffusion Parameter, $10^3 D_e/r_c^2$ (s^{-1})				
	323°K	373°K	423°K	473°K	523°K	323°K	373°K	423°K	473°K	523°K
0	244	36.7	17.3	11.8	9.79	1.21	5.16	8.36	11.1	12.8
0.061	190	-	19.5	13.1	10.1	1.65	-	5.53	7.79	10.1
0.100	102	-	34.5	11.7	9.74	2.44	-	4.37	7.82	8.57
0.176	94.1	29.3	16.7	10.7	9.11	2.30	5.05	6.02	9.57	10.3
0.247	71.8	23.7	14.4	9.87	8.82	2.73	6.83	6.51	10.6	9.51
0.357	56.7	20.5	11.9	8.88	7.99	3.48	6.08	11.8	13.0	12.4
0.473	41.9	17.8	11.4	8.08	7.36	4.12	6.55	8.53	14.9	15.1
0.583	31.4	15.2	11.0	8.95	7.77	7.64	11.3	12.6	17.3	21.4
0.701	26.1	13.6	-	8.60	-	9.01	13.7	-	21.5	-
0.778	24.1	12.8	8.22	8.71	7.94	11.5	32.0	55.9	48.4	48.1
0.849	34.4	24.3	19.9	11.6	10.4	13.9	54.7	56.5	71.2	64.3
0.865	27.2	25.7	16.2	12.5	11.2	20.4	79.4	74.2	70.3	78.2
0.902	30.3	31.4	17.9	16.0	14.8	25.3	103	80.6	79.0	99.3
0.926	46.9	27.6	19.2	17.1	15.2	52.6	99.3	92.4	105	129

TABLE 3

WYODAK COAL CHAR REACTED AT 1073°K ARRHENIUS PARAMETERS
FOR DIFFUSION OF CARBON DIOXIDE, CARBON
MONOXIDE, NITROGEN, AND METHANE

Conversion	CO_2		CO		N_2		CH_4	
	$\Delta H_a^{\ddagger}$ (KJ/mol)	$(D_e/r_c^2)_o$ (s^{-1})	$\Delta H_a^{\ddagger}$ (KJ/mol)	$(D_e/r_c^2)_o$ (s^{-1})	$\Delta H_a^{\ddagger}$ (KJ/mol)	$(D_e/r_c^2)_o$ (s^{-1})	$\Delta H_a^{\ddagger}$ (KJ/mol)	$(D_e/r_c^2)_o$ (s^{-1})
0.0	9.94	0.13	11.0	1.46	9.68	1.09	19.6	8.26
0.061	12.9	0.20	6.18	0.42	5.36	0.35	10.7	1.00
0.100	9.16	0.070	11.2	1.79	6.89	0.57	13.8	2.46
0.176	10.5	0.13	9.84	1.27	6.08	0.48	11.1	1.35
0.247	8.64	0.082	7.29	0.59	5.40	0.36	11.8	1.64
0.357	9.78	0.14	7.15	0.60	5.03	0.34	8.54	0.72
0.473	9.70	0.15	9.88	0.40	4.87	0.32	6.95	0.48
0.583	6.97	0.10	3.34	0.22	4.25	0.28	5.29	0.33
0.701	7.33	0.13	4.69	0.33	4.13	0.29	5.13	0.33
0.778	3.93	0.13	3.32	0.20	2.66	0.18	3.97	0.23
0.849	2.40	0.12	2.84	0.22	3.82	0.28	3.85	0.27
0.865	-	-	3.58	0.26	-	-	6.00	0.45
0.902	3.83	0.24	4.15	0.33	-	-	4.93	0.36
0.926	6.14	0.52	5.15	0.47	5.19	0.48	5.03	0.42

THE REACTION OF CO_2 WITH COKE ON SPENT CATALYSTS

W. P. Hettinger, Jr., J. F. Hoffman and S. M. Kovach

Ashland Petroleum Company
Research and Development Department
Ashland, Kentucky 41114

Introduction

The processing of residuum from the bottom of the crude oil barrel into transportation fuels has become both economically attractive and necessary as crude oil has become heavier and more expensive. In processing these heavier feedstocks, as with Ashland Oil's RCC^{sm} heavy oil conversion process, more coke is produced than in conventional FCC operations. Tremendous amounts of heat are produced during the regeneration of coked catalysts. Conventional methods to moderate the temperature in the regenerator of a circulating fluidized bed include controlling operational parameter (eg. cat/oil, feed preheat, and reactor temperature), direct addition of steam and/or water to the riser or regenerator (U.S. Patent 4,405,444), the use of multi-bed regenerators (CAN Patent 1,137,455), the use of steam coils in the regenerator, and the incomplete combustion of coke (U.S. Patent 4,354,923). Because of economic constraints on varying the operational parameters and metallurgical limitations, and temperature stability of catalysts, especially when loaded with Ni and V,[1] a practical limit to the regenerator temperature exists. In a further effort to lower the amount of heat produced in the regenerator, other solutions to the problem were sought.

Program

One new approach not mentioned above was to employ the Boudouard Reaction, one of the principle reactions studied for many years in the steel industry as related to iron production. This paper reports the results of a study of the partial regeneration of spent (coked) cracking catalysts with CO_2 (Boudouard Reaction). It also reports a second and equally interesting reaction which was uncovered in the course of this work. The second reaction is called the H-reaction, which is the reaction of the hydrogen associated with the carbon in the "catalytic coke" with CO_2 to produce CO and water. Catalytic coke on spent catalyst is a species which is 92-97%C and 3-8%H and contains minor amounts of sulfur and nitrogen.

The reaction of carbon with CO_2 to produce carbon monoxide (Boudouard Reaction)[2,3,4] is endothermic as is well known. The H-reaction also appears to be slightly endothermic. The H-reaction would lower the amount of heat produced in the regenerator if it could be achieved at the exit temperature of the reactor (1000°F) or at a slightly higher temperature in the spent catalyst stripper section by removing hydrogen before it can undergo combustion. Carbon dioxide in the flue gas from an FCC or RCC unit is available for these reactions.

The pertinent thermodynamics parameters for the coke-O_2 and coke-CO_2 reactions are presented in Table 1.[5] The equilibrium constant of the Boudouard Reaction does not favor the formation of CO at temperatures below 1300°F. In order to obtain significant amounts of CO, temperatures above 1800°F are required.[6] By use of a promoter, substantial

amounts of CO can be produced at 1350-1400°F. The most active promoters of the Boudouard Reaction are salts of the alkali metals and the metals of Group VIII in the periodic table[6]. The H-reaction was found to proceed at a much lower temperature than the Boudouard Reaction, hence, it is of greater interest because of the lower temperature at which it can be initiated.

In past investigations of the Boudouard Reaction, the fate of the hydrogen present in very small quantities in coke has not apparently been of interest. In this investigation, an attempt has been made to confirm the production of the H_2O formed by the reaction of the hydrogen-associated coke with CO_2, and to determine the lower temperature limit where this reaction can be utilized.

The objectives of this work were to determine:

1) The metals which would promote the Boudouard Reaction, but do not adversely affect the activity and selectivity of the cracking catalyst.

3) The effect of nickel and vanadium, which are deposited on the catalyst during the cracking reaction, as promoters of the Boudouard Reaction.

3) The fate of hydrogen during the reaction of coke with CO_2.

4) The temperature at which the H-reaction initiates.

Experimental

Catalyst samples which had been coked in a commercial circulating fluidized bed unit were impregnated with aqueous solutions of a metal salt (chloride or nitrate) by the incipient wetness technique. The solutions were prepared with the appropriate metal salt to give 1.0 wt% as the element on the catalyst after impregnation. The impregnated catalysts were then dried at 300°F for at least three hours before testing. The activity of the impregnated catalyst to promote the Boudouard Reaction was determined by measuring the amount of carbon which had reacted during a 30 minute test. The reaction was performed at 1400°F in a 1" ID Vycor reactor with a thermocouple well in the dense phase of the fluidized bed. Twenty grams of the coked metal impregnated catalyst was heated to the reaction temperature and equilibrated in a stream of helium. Carbon dioxide was then introduced at a constant rate of 1.7 scfh. The CO concentration in the product gases was monitored at regular intervals by gas chromatography. After each test, the catalyst was cooled in helium and the %C left on the catalyst was determined.

In order to study the H-reaction, the catalyst was heated to 600°F for one hour in helium to remove physically adsorbed water. After cooling to 100°F in helium, the catalyst was heated in CO_2 to the desired temperature, 900-1400°F, over a 30 minute period, and then held at this temperature for an additional 30 minutes. The moisture content of the gas stream was measured over the entire 60 minute test with a Shaw hygrometer (Model SH), which was equipped with a gold spot sensor. This sensor was capable of measuring dew points between -58°F and +68°F. The amount of H_2O produced during the H-reaction was calculated by integrating the plot of dew point vs. time.

Results and Discussion

A. Metal Promoters for the Boudouard Reaction

A wide variety of metal salts have been tested as possible promoters for the Boudouard Reaction. The results of the screening tests showed that the most active promoters were the alkali metals and the metals of Group VIII, which agreed with earlier literature reports[6]. The screening tests consisted of impregnating each metal onto the coked catalyst and then determining its activity by measuring the %C on the catalyst after contact with CO_2 for 30 minutes. Each promoter was tested on the same spent catalyst (Ni+V = 5900 ppm). The metals were divided into three classes (Table 2) based on their activity to promote the Boudouard Reaction.

An important requirement of this investigation was that the cracking activity and selectivity of the catalyst should not be affected by the promoter. The cracking activity and selectivity were measured by a standard micro-activity test (MAT)[7]. The catalyst was calcined at 1100°F for 2 hours to remove all of the coke before running the MAT. The highest activity promoters in Table 2 were evaluated by the MAT. The results of the MAT evaluation are given in Table 3. Catalyst cracking activity is related to the MAT conversion, and selectivity is related to the coke producing factor (CPF) and hydrogen producing factor (HPF). The CPF or HPF is defined as the ratio of the amount of coke or hydrogen produced during the test to the amount produced with a standard catalyst at the same conversion.

A comparison of Table 2 and 3 showed that while the lithium promoted catalyst exhibited the highest activity for the Boudouard Reaction, the cracking activity, as expected, had been drastically reduced by the addition of lithium. Of the other promoters in the highest activity group of Table 2, copper and strontium were selected for further study based on the MAT results. Barium was also selected for further study even though on the standard catalyst the activity was in the lowest class. At Ni+V concentrations greater than 8000 ppm, barium did exhibit substantial activity for the Boudouard Reaction.

Lithium because of its deleterious effect on cracking activity, and rhodium, because of its cost, were not considered possible promoters at the 1.0 wt% and 0.5 wt% levels, respectively. In an attempt to use these high activity promoters, the effect of promoter concentration on activity was examined (Table 4). At feasible concentrations of the promoters (0.1% Li and 5 ppm Rh), their activity had decreased to a level comparable to the unpromoted reaction.

The effect of the contaminant metals (Ni and V), which were deposited on the catalyst during the cracking reaction, on the activity of the various promoters was investigated. Each promoter was impregnated on various spent equilibrium catalyst samples. The results of these tests were plotted as %C on catalyst after the 30 minute test (normalized to 1.0 wt% C initially on the catalyst) versus Ni+V (Figures 1-3 for copper, strontium and barium promoted catalysts, respectively). Each metal promoted the Boudouard Reaction to a greater extent as the concentration of Ni+V increased. The promoter and the contaminant metals exhibited a synergistic effect on increasing the rate of the Boudouard Reaction. The circled data points in Figures 1-3 supported the idea of synergism. These data points were the results of experiments in which the Ni/V ratio on the catalyst was equal to one. The

remaining data points, those that fall on the curves, were the results of experiments in which the promoters were impregnated on catalysts with Ni/V ratios equal to 1/3. The circled data points showed, at comparable metals levels, that less coke had undergone reaction with CO_2 in the catalysts with lower vanadium concentrations. Vanadium, when impregnated on spent catalyst, exhibited moderate activity (35% carbon removal on a catalyst containing 5900 ppm Ni+V). Nickel and vanadium, deposited on the catalyst during the cracking reaction, promoted the Boudouard Reaction only when the total concentration of these metals was greater than 8000 ppm. At Ni+V concentrations, above 15,000 ppm, these metals promote the Boudouard Reaction to the same extent as the highest activity metals (see Figure 4).

In the previous experiments, the catalyst samples were impregnated with the promoter after the catalyst was deactivated with coke. However, in a commerical process, the promoter could be deposited on the catalyst during manufacture or during the process. A series of experiments were performed to compare the activity of barium impregnated on the catalyst before coking and after coking. The conclusion was that barium exhibited a higher activity when the metal was impregnated before the catalyst was deactivated (see Table 5).

A series of experiments were performed to test the ability of a barium promoted catalyst (Ni+V = 12,600 ppm) to maintain activity over ten coking-regeneration cycles. Each cycle consisted of, first, coking the regenerated catalyst with a vacuum gas oil at 900°F, then allowing the spent catalyst to react with CO_2 for 30 minutes at 1400°F, and finally, regenerating the catalyst with air at 1200°F. In Figure 5, the peak height of CO in the GC analysis of the product gas stream plotted against the number of coking-regeneration cycles. The amount of CO in the gas stream was determined 5 times (at 2, 9, 16, 23 and 30 minutes) during coke-CO_2 reaction. The activity of the promoter decreased slightly over the ten cycles.

B. H-Reaction Studies

Coke has a composition in the range of 92-97% C and 3-8% H[8] with trace amounts of nitrogen and sulfur. In previous reports[9,10] on promoting the Boudouard Reaction, the hydrogen in coke has either been assumed not to react with CO_2 or not mentioned. Hydrogen in the coke on spent catalyst was calculated to be responsible for 15-25% of the heat generated during the regeneration of catalyst spent. In this investigation, the hydrogen in coke was found to react with CO_2 to produce water according to the reaction sequence:

$$C_yH_x + CO_2 \longrightarrow C_yH_{x-2} + CO + H_2O \text{ (H-reaction)}$$

While the enthalpy change for this reaction has not been determined, it is believed to be considerably more endothermic than for the combustion reaction. By allowing the H-reaction to occur, the amount of hydrogen which must undergo combustion in the regenerator section of a fluidized reactor system would be decreased, thus, less heat would then be produced in the regenerator.

With a hygrometer inserted into the product gas stream line, the amount of water in the product gas stream, as measured by the dew point (in

°C), was determined. The concentration of water in the gas stream was determined by the equation:

$$\log (H_2O \text{ in ppm}) = 13.33 - 261.3/\text{Dew Point } (°K)$$

A comparison of the amount of H_2O produced during the reaction of CO_2 with a coked and a regenerated catalyst is given in Figure 6. The difference in the two plots is a measure of the amount of water produced by the H-reaction. The water observed in the dew point plot of the regenerated catalyst is attributed to catalyst dehydroxylation at 1400°F. With this technique, the amount of hydrogen in coke on a catalyst is found to be between 3-10%. The range in this value is the result of uncertainty in the amount of hydrogen in the coke which did not react during the 30 minute test.

C. Initiation Temperature of the H-Reaction

One of the potentially useful aspects of the H-reaction is that it could be made to occur in the reactor (spent catalyst) stripper of the RCC^{sm} process unit. The temperature of the catalyst in the stripper is usually between 900-1050°F. The thermodynamics of the H-reaction as compared to the water gas shift reaction indicates that hydrogen in coke will react at temperatures within this range. Carbon dioxide could easily be used either in place of or in conjunction with steam as a stripper gas. The advantage of reacting hydrogen in the stripper in the RCC^{sm} process unit is apparent from the data in Figure 7. This figure shows the relationship for a particular set of unit operating conditions between Conradson carbon in the feed, the water addition to the riser, and the hydrogen content in the coke in order to maintain the RCC^{sm} process unit in heat balance at a CO_2/CO ratio in the flue gas equal to one. By lowering the hydrogen content in coke, feedstocks with higher Conradson carbon values can be processed with the heat balance being maintained in the RCC unit.

The temperature at which a measurable amount of water is produced by the H-reaction has been determined. The initiation temperature was determined by a series of temperatures in which the catalyst was heated to a predetermined temperature (eg., 900°, 1000°, 1400°F) in CO_2 and the amount of water produced during the CO_2 reaction was measured. Before each test, the catalyst was heated to 600°F in an attempt to remove physically adsorbed water. The results of these experiments are shown in Figure 8. The set of dew point plots show that substantially more water is produced at 1000°F and 1400°F than at 900°F. Temperatures between 800°-900°F give identical dew point plots to the one at 900°F. These data indicate that the rate of the H-reaction becomes measurable between 900° and 1400°F. The source of the water in the dew point plots obtained at reaction temperature below 900°F is believed to be adsorbed water.

A series of experiments in a product distribution unit (PDU) were performed to quantify the amount of water produced by the H-reaction. The PDU is a homogeneous fluid bed reactor which uses a liter of catalyst. The larger volume of catalyst allows for a more accurate determination of the water produced by the hydrogen reaction. The catalyst was heated in the reactor at 1250°F in dry O_2 free N_2 overnight to remove all adsorbed and chemical water. The catalyst was then coked with a reduced crude oil and the entrained hydrocarbons were stripped from the catalyst with N_2. At this point, CO_2 was introduced into the reactor, at either 1000° or 1100°F. The product gases from the H-reaction were

monitored for their water content continuously. After two hours, the CO_2 was stopped and air was introduced into the reactor to burn the remaining hydrogen off the catalyst. The amount of hydrogen which had reacted with CO_2 was calculated by comparing the water produced by the H-reaction to the water produced by the combustion reaction. From these calculations, it was found that 4% of the hydrogen in the coke on the catalyst reacts at 1000°F, while at 1100°F, 10% of the hydrogen in the coke on the catalyst has reacted.

Conclusions

This report describes an investigation into a novel method to lower the amount of heat produced in the regenerator of an RCC^{sm} process unit. Three metal promoters (Cu, Sr and Ba) were found for the Boudouard Reaction which allowed the reaction to occur at 1400°F without severely affecting the cracking activity of the catalyst. Another promising result of this investigation was that a fraction of the hydrogen in coke reacts with CO_2 at 1000°F. At this temperature, a portion of hydrogen could be removed from the catalyst in the reactor stripper, thereby lowering the amount of hydrogen in coke which must be burned off the catalyst. This would allow for the processing of heavier feedstocks in an RCC^{sm} process unit, while maintaining moderate temperatures in the regenerator.

References

1. Zandona, O. J., Busch, L. E., and Hettinger, Jr., W. P., NPRA 80th Annual Meeting, Paper AM-82-61, March 21-23, 1982

2. Boudouard, Ann Chim. Phys., 24 5 (1901).

3. Holstein, W. L., Bodart, M., J. Catal. 75 337 (1982)

4. Jalan, B. P., Rao, Y. K., Carbon 16 175 (1978)

5. Stull, D. R., Westrum, Jr., E. F., and Sinke, G. C., "The Chemical Thermodynamics of Organic Compounds", John Wiley and Sons, Inc., New York, 1969

6. McKee, D. W., General Electric Technical Information Series, Report No. 78CRD076, Schenectady, NY, April, 1978

7. Hettinger, Jr. W. P., Beck, H. W., Cornelius, E. B., Doolin, P. K., Kmecak, R. A. and Kovach, S. M., Div. Petrol. Chem. Preprints, ACS 28 (4) 920 (1983)

8. Sotirchos, S. V., Mon, E., and Amundson, N. R., Chem. Eng. Sci. 38 55 (1983)

9. Marsh, H. and Rand, B., Carbon 9 63 (1971)

10. Hippo, E., and Walker, Jr., P. L. Fuel 54 245 (1975)

Table 1

Thermodynamic Parameters

Reaction	H (kcal/mole) at 298°K	H (kcal/mole) at 1000°K	G (kcal/mole) at 1000°K
$C + 1/2\ O_2 \rightleftharpoons CO$	-26.42	-26.77	-47.95
$C + O_2 \rightleftharpoons CO_2$	-94.05	-94.32	-94.61
$H_2 + 1/2\ O_2 \rightleftharpoons H_2O$	-57.80	-59.24	-46.04
$C + CO_2 \rightleftharpoons 2CO$	+41.21	+40.78	- 1.29
$H_2 + CO_2 \rightleftharpoons H_2O+CO$	+ 9.83	+ 8.31	+ 0.62

Table 2

Classes of Boudouard Reaction Promoters

High Activity	% Coke Reacted	Low Activity	% Coke Reacted
Li	69	Mo	29
Co	55	Sn	28
$CuCl_2$	55	Ca	27
Ni	53	Ti	25
Rh (0.5 wt%)	53	Cr	25
Fe	52	La	25
Na	52	Y	25
Ru (0.5 wt%)	52	Zn	24
Sr	46	Zr	24
$Cu(NO_3)_2$	42	U	23
		B	22
Moderate Activity		Ba	22
		Cs	22
V	35	K	20
Ag	31	In	20
Bi	30	Mn	20
		Cd	16
		None	15
		W	15
		Sb	9

Catalyst - Super DX w/1.10% C
Temperature - 760°C
Reaction Time - 30 minutes
Promoter Concentration - 1.0 wt% except where noted

Table 3

MAT Results of Promoted Catalysts

Promoter	Concentration (wt%)	Conversion (vol)(%)	CPF	HPF
None	0	61	1.2	13
Li	1.0	10	3.9	10
$CuCl_2$	1.0	65	1.5	17
$Cu(NO_3)_2$	1.0	62	1.6	18
Sr	1.0	50	1.2	10
Ba	1.0	56	1.1	9
Fe	1.0	52	2.3	22
Ni	1.0	53	3.2	33
Li	0.5	16	3.7	11

Table 4

The Effect of Promoter Concentration on the Boudouard Reaction

Li Conc. (wt%)	% Coke Reacted
1.0	69
0.5	44
0.33	35
0.1	25
Rh Conc. (ppm)	
5000	53
500	44
50	26
5	17

Table 5

Sequence of Promoter Addition

Catalyst	%C Reacted	Sequence
1.0 wt% Ba on Catalyst X	.64	Coke over Ba
1.0 wt% Ba on Catalyst X	.71	Ba over Coke
1.0 wt% Ba on Catalyst G	.74	Coke over Ba
1.0 wt% Ba on Catalyst G	.84	Ba over Coke

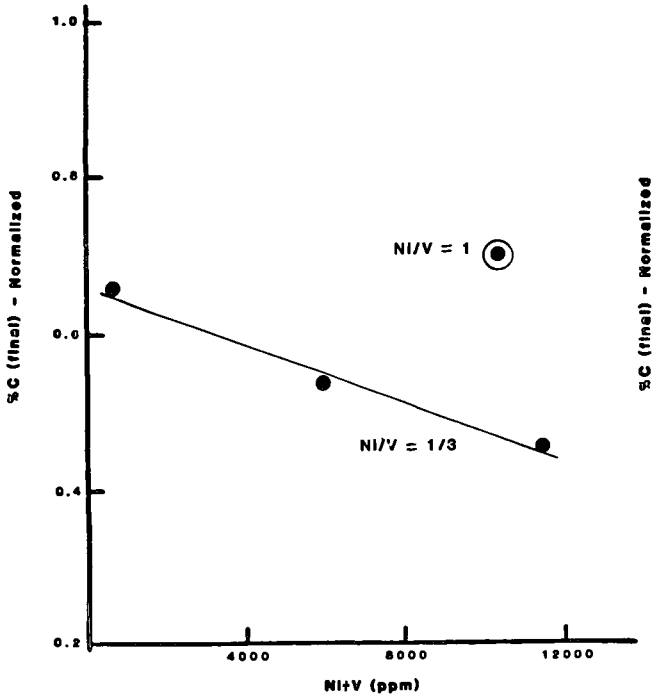

Figure 1. The Effect of Metals on Promoter Activity - Copper

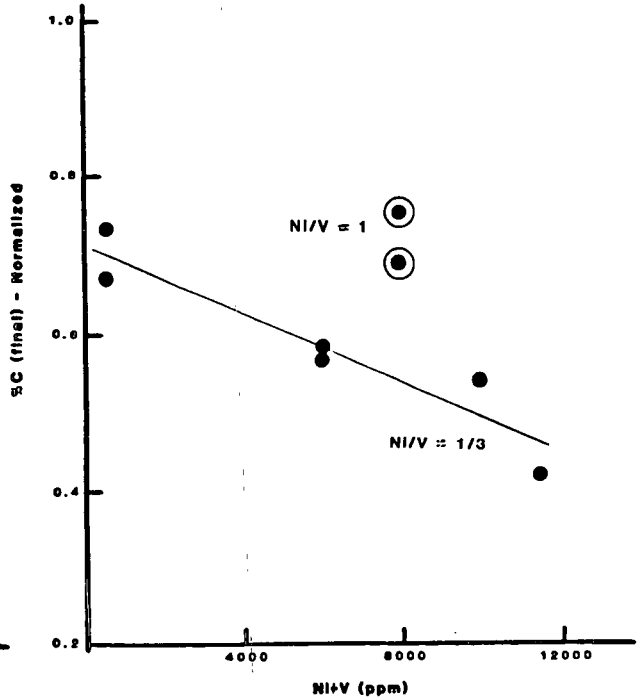

Figure 2. The Effect of Metals on Promoter Activity - Strontium

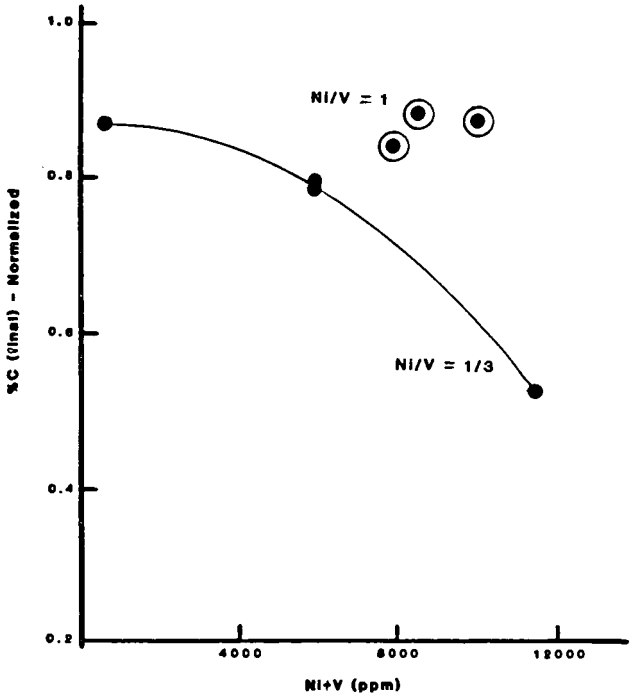

Figure 3. The Effect of Metals on Promoter Activity - Barium

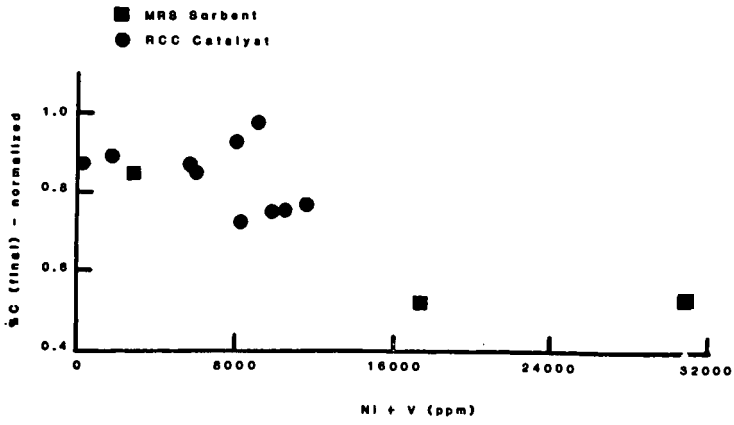

Figure 4. The Effect of Metals on the Rate of the Unpromoted Boudouard Reaction

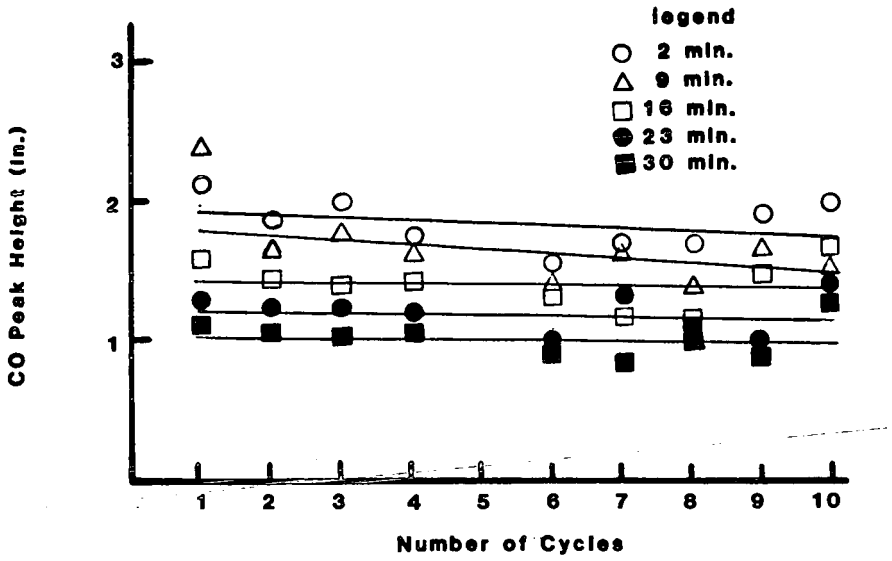

Figure 5. The Effect of Repeated Coking-Regeneration Cycles on the Activity of the Boudouard Reaction Promoter

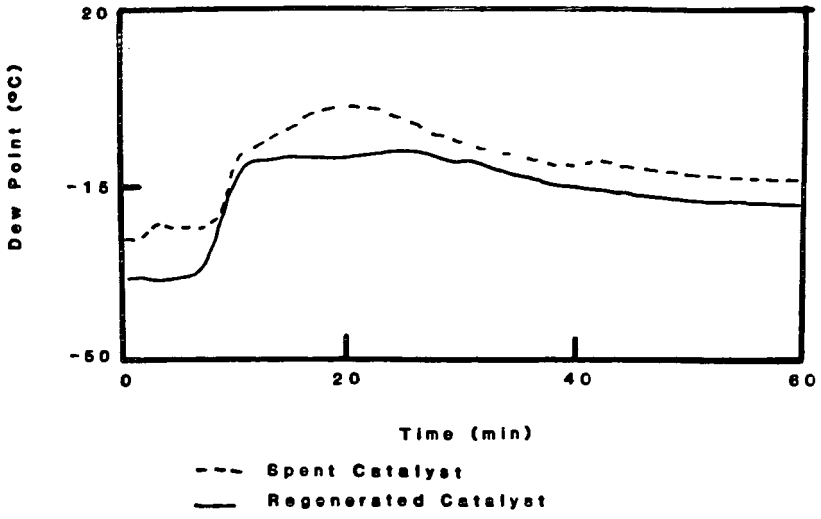

Figure 6. H-Reaction Comparison of Spent and Regenerated Catalysts

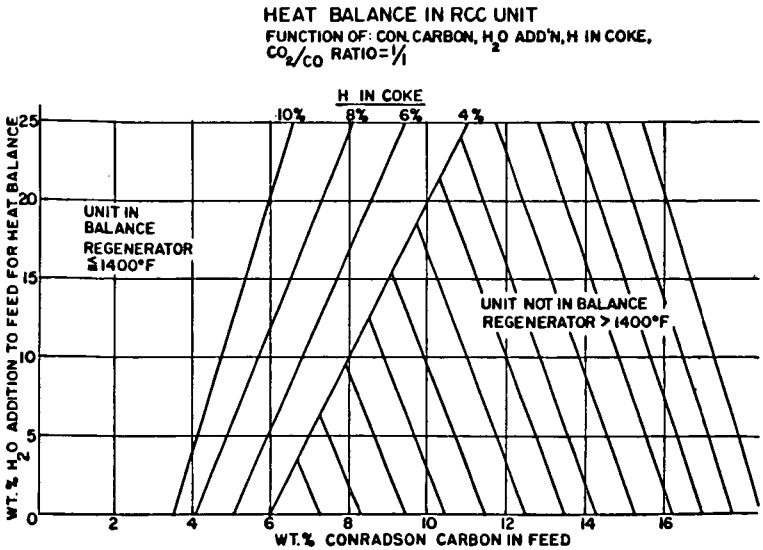

Figure 7. Heat Balance in RCC Unit

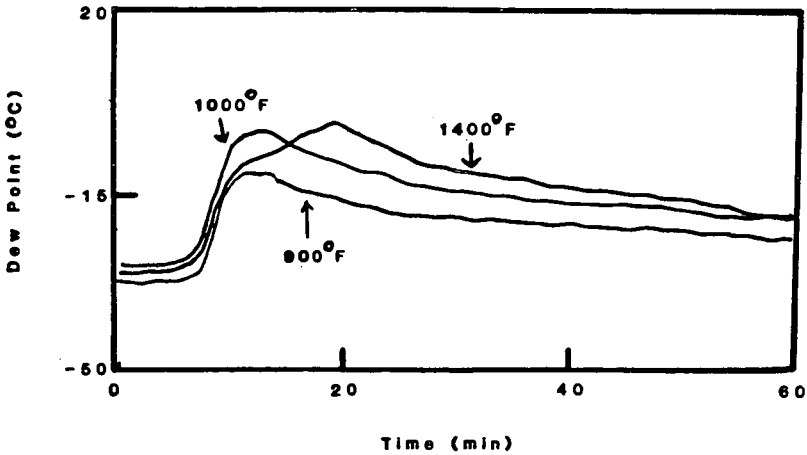

Figure 8. Initiation Temperature of the H-Reaction